# Image acquisition and reconstruction in multi-pinhole emission tomography

Proefschrift

ter verkrijging van de graad van doctor
aan de Technische Universiteit Delft,
op gezag van de Rector Magnificus prof. ir. K.C.A.M. Luyben,
voorzitter van het College voor Promoties,
in het openbaar te verdedigen op 11 september 2014 om 15.00 uur
door Pieter Eric Bart VAISSIER
Master of Science in Biomedical Engineering
geboren te Nijmegen

Dit proefschrift is goedgekeurd door de promotor:
Prof. Dr. F.J. Beekman

Copromotor    Dr. ir. M.C. Goorden

Samenstelling promotiecommissie:

Rector Magnificus,            voorzitter
Prof. Dr. F.J. Beekman,       Technische Universiteit Delft, promotor
Dr. ir. M.C. Goorden,         Technische Universiteit Delft, copromotor
Prof. Dr. ir. L.J. van Vliet, Technische Universiteit Delft
Prof. Dr. R. Boellaard,       VU University Medical Center
Prof. Dr. M. Defrise,         Vrije Universiteit Brussel
Prof. Dr. O.C. Boerman,       Radboud University Medical Center
Prof. Dr. H. Zaidi,           Geneva University Hospital
Prof. Dr. P. Dorenbos,        Technische Universiteit Delft, reservelid

# Contents

# 1. Introduction and thesis outline

## *1.1 Radio-molecular imaging*

Nowadays, tomographic imaging techniques are  inseparable from modern medical practice as they allow non-invasive 3-dimensional visualization of the interior of a patient in order to e.g. establish a medical diagnosis, or to monitor disease progression and the effects of disease treatment. Next to clinical use, tomographic imaging techniques are also applied in research with small animals, like mice and rats, in studies of disease or in the development of pharmaceuticals.

The various imaging techniques (imaging modalities) that are available each have their own qualities with respect to visualizing different aspects of the body's structure and/or function. Therefore, one needs to select the most suitable technique for the imaging task at hand. Generally, modalities can be classified into structural/anatomical modalities and functional/molecular modalities. Figure 1 displays example images obtained with different imaging modalities: X-ray Computed Tomography (CT) and Magnetic Resonance Imaging (MRI) mainly provide anatomical information, whereas Single Photon Emission Computed Tomography (SPECT) and Positron Emission Tomography (PET) are functional imaging techniques *pur sang*, as they provide accurate information about physiological and pathological  properties of specific tissues of the body down to the cellular level. Images obtained with different imaging modalities are often combined since these different modalities can provide highly complementary or enhanced information. To this end, even hybrid imaging systems have been developed which combine two or more modalities on a single platform.

SPECT and PET visualize the distribution of radioactive tracer molecules ('tracers') that are injected into a patient. These tracer molecules are biochemically designed in such a way that they accumulate at target locations in the body. The radiation emitted by the tracer molecules can be detected and a 3-dimensional image of the tracer distribution can be reconstructed from the projection measurements. The type of tracer molecule that is injected determines the physiological processes or biochemical pathways that are visualized: e.g. some tracers accumulate in/around tumor cells, while others are designed to be a measure for metabolic rate, perfusion or receptor density of specific tissues. SPECT and PET have applications in the fields of e.g. cardiology, oncology, neurology and psychiatry. A major difference between SPECT and PET lies in the nature of the radioactive decay of their tracers: a SPECT tracer decays by emitting single gamma photons, while decay of a PET tracer results in the emission of pairs of annihilation photons. As a result, different detection principles have been developed for SPECT and PET tracers, which has led to separate SPECT and PET scanners. However, recently it was shown by our group that high-resolution simultaneous imaging of SPECT and PET tracers in mice is possible with a single device, namely a modified small-animal multi-pinhole SPECT system. The work in this thesis mainly focuses

on new image acquisition and image reconstruction techniques for high-resolution multi-pinhole imaging of SPECT and PET tracers.
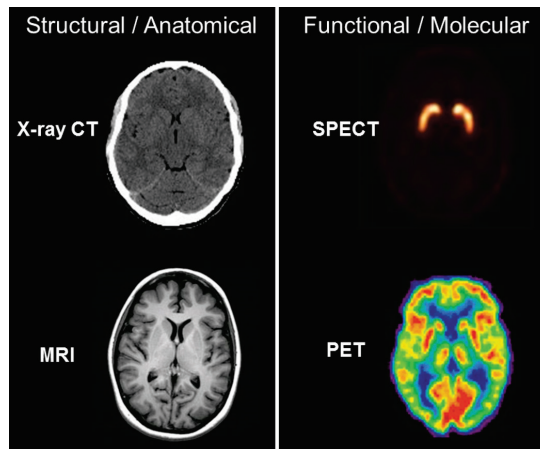


**Figure 1**. *Examples images of the brain obtained with different tomographic imaging techniques. Tomographic techniques used in medicine can roughly be classified into structural/anatomical modalities, like X-ray CT and MRI, and functional/molecular modalities, like SPECT and PET.*

## 1.2 Gamma-cameras and collimators

SPECT images tracers by detecting the gamma photons that are emitted when the radioactive isotopes in the tracer molecules decay. These photons are detected by dedicated gamma-cameras, which provide the estimated position of each detected photon on the detector, but leaves the direction from which a photon originated unknown. However, directional information of photons is required to enable reconstruction of the tracer distribution. To this end, a gamma camera is equipped with a collimator that is positioned between the source and the camera. The collimator only allows gamma photons from certain directions to reach the detector. Collimators are made of dense materials, like lead or tungsten, because these materials have a high stopping-power for the gamma photons that are emitted by SPECT tracers. A widely-used SPECT collimator is the parallel-hole collimator which consists of a slab of material with parallel holes in the direction normal to the detector. Such a collimator only permits gamma photons from directions normal to the detector surface to reach the detector. A parallel-hole collimator produces a 2-dimensional parallel projection of the source distribution onto the gamma-camera (Fig. 2a). Other types of collimators may have diverging holes, converging holes (like the cone- or fan-beam collimator) or pinholes. The type of collimator that is used for a SPECT scan depends on the imaging task since each collimator type has advantages and disadvantages with respect to e.g. resolution, sensitivity,

field-of-view, object sampling, required image reconstruction technique and required orbit of the gamma camera(s).

## 1.3 Pinhole SPECT

Since collimators block a considerable fraction of the gamma photons to obtain directional information of the photons that are detected, there is a trade-off between the number of gamma photons that is detected (sensitivity) and the accuracy with which their direction is known, which has an effect on the sharpness (i.e. spatial resolution) of the projections which in turn affects the spatial resolution of the reconstructed image. An increase in either sensitivity or spatial resolution often goes at the expense of the other: e.g. smaller holes in a collimator result in improved directional information of the detected photons, and therefore improved spatial resolution, however less photons will be detected since a larger fraction will be stopped by the collimator. The spatial resolution is not only determined by the design of the collimator, but also by the intrinsic resolution of the camera (i.e. the accuracy with which the position of a detected gamma photon on the detector is estimated). The total combined spatial resolution $R_t$ of a SPECT system can be approximated by a combination of the geometric resolution of the system as a result of collimation $R_g$ and the intrinsic resolution of the gamma camera $R_i$:

$$R_t = \sqrt{R_g^2 + R_i^2} \tag{1}$$

The spatial resolution of clinical SPECT is of the order of 10 mm, which is adequate to locate tracer uptake at sub-organic level in humans. However, for small animals like mice this resolution is inadequate since mice are a few thousand times smaller than humans; acceptable resolutions for these animals are in the sub-millimeter range. It can be deduced from (1) that for a high-resolution collimator (i.e. $R_g << R_i$ ), the total system resolution $R_t$ is approximately equal to the intrinsic detector resolution $R_i$, which is typically a few millimeters for a conventional SPECT camera. Thus, sub-mm resolution SPECT is out of reach with parallel hole collimation and conventional SPECT cameras. In order to improve SPECT resolution, pinhole collimation was introduced. A pinhole that is adequately placed between the source and detector produces a magnified inverted projection of the source distribution on the detector (Fig. 2a). Pinhole magnification strongly reduces the influence of the intrinsic detector resolution on $R_t$ according to:

$$R_t = \sqrt{R_g^2 + \left(\frac{R_i}{F}\right)^2} \tag{2}$$

In (2), the pinhole magnification factor $F$ is the ratio of the detector-to-pinhole distance to the source-to-pinhole distance. The development of dedicated small-animal SPECT systems with high pinhole magnification factors has enabled to reach sub-millimeter SPECT resolutions in mice and rats [1].

Collimators with multiple pinholes are often being used as they can provide much better sensitivities than a single pinhole. If all pinholes focus on the same area in a subject, a high sensitivity can be obtained within the focal region of the pinholes (Fig. 2b). Conventional SPECT systems must rotate their camera(s) and collimator(s) around the subject to acquire enough projection views to enable a 3-dimensional image to be reconstructed. However, systems that apply a focusing multi-pinhole collimator and detectors that surround the subject can readily acquire enough projection views and a high sensitivity in the focal region of the pinholes without any detector movement [1-3]. Larger areas of the body can still be scanned by stepping the animal through the focal region [4]. Based on these principles and using a clinical SPECT system with three gamma cameras, a small-animal SPECT system was developed at University Medical Center Utrecht, called the U-SPECT-I [5]. A focusing multi-pinhole collimator can be inserted into this system to enable sub-half mm resolution SPECT of mice. From U-SPECT-I, U-SPECT-II was developed [1]. Compared to U-SPECT-I, improvements included larger detectors and exchangeable collimators optimized for different imaging tasks and differently sized rodents.
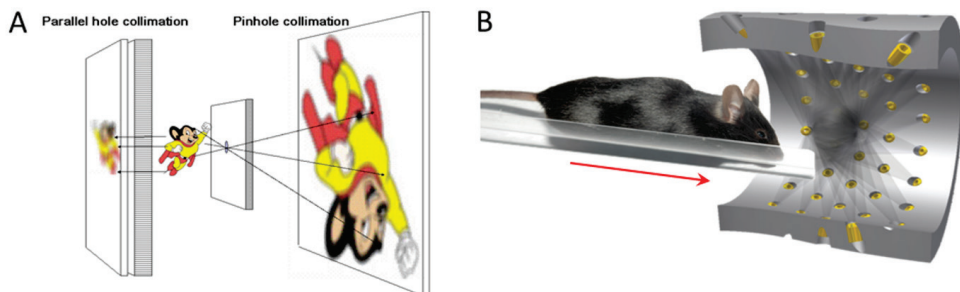


**Figure 2**. *(a) Parallel-hole collimation vs. pinhole collimation. (b) Mouse inside cylindrical focusing multi-pinhole collimator.*

## 1.4 Simultaneous SPECT-PET imaging with pinholes

SPECT allows imaging of multiple tracers in a single scan, as long as it is possible to distinguish between the energies of the gamma-photons that originate from different tracers. Traditionally, PET tracers are imaged by a technique called 'coincidence imaging' in which the two (approximately) antiparallel gamma photons that result from PET tracer decay are imaged in coincidence by a ring of detectors surrounding the object. Based on the high resolutions of pinhole SPECT and the advantages of multi-tracer SPECT imaging, a Versatile Emission Computed Tomography (VECTor) system has recently been developed within our

group. VECTor employs a novel collimation technique which allows pinhole-collimated gamma-ray imaging of PET tracers, even simultaneously with SPECT tracers [6]. This way, the concept of multi-tracer imaging has been extended to include a whole new and important class of PET tracers. Because the annihilation photons resulting from PET tracer decay (511 keV) have much higher energies than those of common SPECT isotopes (typically 30-250 keV), the detection of annihilation photons requires a dedicated high-energy collimator in order to reduce the penetration of these photons through the pinhole edges [7]. The work performed in this thesis largely revolves around U-SPECT-II and VECTor systems.

## *1.5 Image reconstruction*

A SPECT measurement consists of 2-dimensional projections of the radioactive source distribution which are obtained with collimator(s) and gamma-detector(s). It is the goal of an image reconstruction algorithm to accurately reconstruct the (unknown) 3-dimensional distribution of the radioactive source that gave rise to the measured projection data. To this end, different reconstruction methods have been developed which can be classified into analytic and iterative methods.

### 1.5.1 Analytic methods

Analytic image reconstruction methods, like filtered back-projection (FBP), are generally fast since they calculate the activity distribution in a single step. These methods are based on a line-integral model which assumes that the number of counts that are measured at a point on the detector is proportional to the total amount of tracer along a straight line through that point in the direction of collimation. However, the theoretical basis for analytic reconstruction requires simplifying assumptions about the imaging process, like the absence of distance-dependent collimator resolution and sensitivity, an unlimited number of projection views and noiseless projection data. Naturally, these assumptions are violated in practice; e.g. SPECT projections are usually noisy and collimator resolution and sensitivity strongly vary with the source-to-pinhole distance for pinhole imaging, which make these analytic methods inadequate for pinhole SPECT.

### 1.5.2 Iterative methods

In contrast to analytic reconstruction methods, iterative methods have been shown to be more robust to statistical noise and allow better modelling of the physical detection process, which can be used to correct for several image-degrading effects. Moreover, these methods are applicable to complex detector- and collimator geometries like those found in multi-pinhole SPECT. A review on iterative reconstruction techniques can be found in [8]. With

iterative methods the projection- and image space are often discretized: The detector projections $P$ are divided into 2-dimensional elements called *pixels* and the image $A$ into 3-dimensional elements called *voxels*. The matrix equation that describes the imaging process (if noise and photon scatter are neglected) is given by:

$$P = MA \tag{3}$$

Equation (3) states that the measured number of photons in one of the projection pixels of $P$ is equal to the number of photons emitted from each voxel (contained in $A$) times the corresponding detection probabilities (contained in the system matrix $M$). The purpose of iterative image reconstruction is –with $P$ and $M$ known– to solve (3) for $A$ by iteratively finding new estimates of $A$ ($\hat{A}$) for which the estimated projections –which can be obtained using (3)– increasingly better match the measured projections.

The Maximum Likelihood Expectation Maximization algorithm (MLEM; [9, 10]) has become an important standard in iterative reconstruction. The MLEM algorithm is based on the assumption that the noise in the data obeys Poisson statistics since the decay of radioactive tracer molecules can be modeled as a Poisson process. Using the Poisson model, MLEM maximizes the likelihood that the estimated activity distribution gave rise to the measured projections by iteratively finding new activity estimates. As a result, images reconstructed by MLEM are less noisy compared to images reconstructed by, for instance, FBP.

A diagram of the calculation steps taken during an iteration of the MLEM algorithm is given in Fig. 3: Reconstruction usually starts with $\hat{A}$ being a uniform activity distribution. Given this $\hat{A}$, corresponding estimated projections $EP$ are calculated in the forward-projection step. These estimated projections are then compared to the measured projections $P$. This results in error projections $P/EP$ which are used in the back-projection step to calculate correction terms to find a new $\hat{A}$. After the update of $\hat{A}$, a new iteration can commence starting with the calculation of new estimated projections.
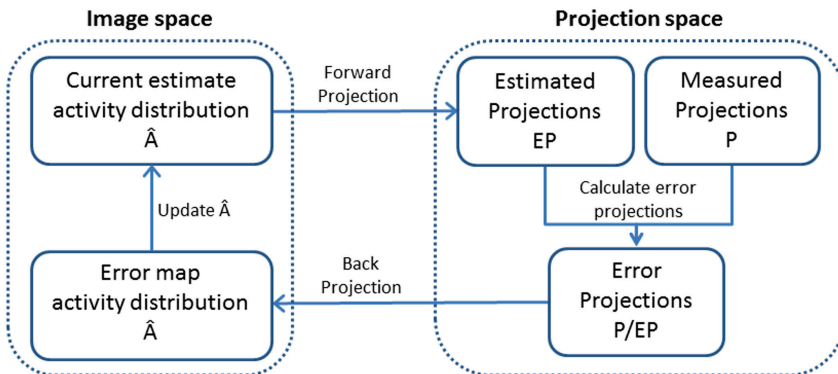


**Figure 3**. *Diagram of steps in the MLEM algorithm.*

Although MLEM is proven to converge to a maximum likelihood estimate of *A*, the estimates of late iterations are usually too noisy for practical use. Therefore, it is common practice to stop the reconstruction process after a number of iterations at which the small details in the image have been largely resolved and where the noise level in the image is still acceptable.

Despite of being consistent and predictable with respect to its convergence behavior, the applicability of MLEM in medical imaging is hampered by the fact that it is computationally costly. Block-iterative methods were introduced in order to strongly reduce the computational costs. Block-iterative methods have led to wide-spread use of iterative algorithms in medical imaging. The rationale that led to the development of block-iterative methods is that a favorable new activity estimate can already be obtained by only using a subset of the projection data, which is computationally much more efficient compared to using all projection data as is the case with MLEM.

With block-iterative methods, an iteration of the algorithm is subdivided into many subsequent sub-iterations, each using a different subset of the projection data. A widely-used block-iterative version of MLEM is the Ordered Subsets Expectation Maximization algorithm (OSEM; [11]). The calculation steps in a sub-iteration of OSEM are the same as for MLEM. The computation time of a full OSEM iteration is about equal to the time needed to perform a single MLEM iteration, while the reconstruction speed-up of a full iteration OSEM over a single iteration MLEM is approximately equal to the number of sub-iterations (i.e. number of subsets).

## 1.6 Thesis outline

The work in this thesis mainly focuses on new image acquisition and image reconstruction techniques for high-resolution multi-pinhole imaging of SPECT and PET tracers in small animals with U-SPECT-II and VECTor systems. However, SPECT is often combined with other imaging modalities and chapter 2 gives an overview of current preclinical research applications and trends of SPECT/CT and SPECT-MRI, mainly in tumor imaging and neuroscience imaging, and discusses advantages and disadvantages of different hybrid imaging approaches.

In chapter 3 it is demonstrated that a SPECT system with stationary gamma-cameras and a focusing multi-pinhole collimator is well-suited for fast dynamic imaging up to total-body scans since there are no moving collimator(s) and detector(s) and the animal can be stepped quickly through the field-of-view. To improve temporal resolutions for (total-body) scans, a new bed-positioning method was developed. The performance of this method was validated and demonstrated by SPECT scans of phantoms and by fast dynamic SPECT scans of mice.

Chapter 4 is an extension of the work of Goorden *et al*. [6], in which it was shown that it is possible to perform simultaneous high-resolution SPECT-PET imaging of mice with the VECTor system. In chapter 4 it is demonstrated that simultaneous SPECT-PET imaging with

VECTor is also possible with rats. To this end, we designed and build a novel high-energy collimator that can accommodate rat-sized animals. The performance of the new collimator was evaluated by sensitivity measurements, SPECT and PET scans of a resolution phantom and by simultaneously acquired SPECT-PET images of rats.

Chapter 5 is a study on the influence of respiratory gating on high-resolution ECG-gated murine cardiac SPECT: Respiratory motion affects the position and orientation of the heart, which -if accounted for- may improve cardiac image quality by reducing image blur in cardiac images. The influence of other factors on cardiac image quality, namely image filtering and animal positioning, is also investigated.

Chapter 6 deals with an issue that can arise if the OSEM algorithm is used for the reconstruction of low-count SPECT data: OSEM can lead to undesirable noise levels and quantitative inaccuracies in the reconstructed images. Since there is no general rule on how to select a safe number of subsets for different data sets, an alternative count-regulated OSEM algorithm (CR-OSEM) is proposed, which automatically adapts the number of subsets depending on the count levels of the projection data. The performance of CR-OSEM is compared to MLEM and OSEM by reconstructions of simulated- and *in vivo* multi-pinhole SPECT data.

In chapter 7 we extend the validation of CR-OSEM to the reconstruction of pinhole-collimated imaging of both SPECT and PET tracers. We show that reconstruction speed of CR-OSEM in image regions with low-activity can sometimes still be rather slow. Moreover, after a many iterations of CR-OSEM, contrast does not always reach the same level as is reached with MLEM after many iterations. To overcome these problems, we propose and validate a novel algorithm, dubbed Similarity-Regulated OSEM (SR-OSEM). Like CR-OSEM, SR-OSEM also automatically and locally adapts the number of subsets. SR-OSEM does this based on a similarity criterion regarding the voxel update factors that are acquired in different subsets. It is shown that SR-OSEM does not suffer from the aforementioned issues that were observed with CR-OSEM and that SR-OSEM significantly outperforms CR-OSEM with respect to reconstruction speed.

## *Bibliography*

[1]    F. Van der Have, B. Vastenhouw, R. M. Ramakers, W. Branderhorst, J. O. Krah, C. Ji, S. G. Staelens, and F. J. Beekman, "U-SPECT-II: An Ultra-High-Resolution Device for Molecular Small-Animal Imaging," *J. Nucl. Med.,* vol. 50, no. 4, pp. 599-605, 2009.

[2]    L. R. Furenlid, D. W. Wilson, Y. C. Chen, H. Kim, P. J. Pietraski, M. J. Crawford, and H. H. Barrett, "FastSPECT II: A Second-Generation High-Resolution Dynamic SPECT Imager," *IEEE Trans. Nucl. Sci.,* vol. 51, no. 3, pp. 631-635, 2004.

[3]    G. K. Kastis, H. B. Barber, H. H. Barrett, H. C. Gifford, I. W. Pang, D. D. Patton, J. D. Sain, G. Stevenson, and D. W. Wilson, "High resolution SPECT imager for three-dimensional imaging of small animals," *J. Nucl. Med.,* vol. 39, no. 5, pp. 9P-9P, 1998.

[4]    B. Vastenhouw, and F. Beekman, "Submillimeter total-body murine imaging with U-SPECT-I," *J. Nucl. Med.,* vol. 48, no. 3, pp. 487-93, 2007.

[5]     F. J. Beekman, F. van der Have, B. Vastenhouw, A. J. van der Linden, P. P. van Rijk, J. P. Burbach, and M. P. Smidt, "U-SPECT-I: a novel system for submillimeter-resolution tomography with radiolabeled molecules in mice," *J. Nucl. Med.,* vol. 46, no. 7, pp. 1194-200, 2005.

[6]     M. C. Goorden, F. van der Have, R. Kreuger, R. M. Ramakers, B. Vastenhouw, J. P. Burbach, J. Booij, C. F. Molthoff, and F. J. Beekman, "VECTor: a preclinical imaging system for simultaneous submillimeter SPECT and PET," *J. Nucl. Med.,* vol. 54, no. 2, pp. 306-12, 2013.

[7]     M. C. Goorden, and F. J. Beekman, "High-resolution tomography of positron emitters with clustered pinhole SPECT," *Phys. Med. Biol.,* vol. 55, no. 5, pp. 1265-77, 2010.

[8]     J. Qi, and R. M. Leahy, "Iterative reconstruction techniques in emission computed tomography," *Phys. Med. Biol.,* vol. 51, no. 15, pp. R541-78, 2006.

[9]     K. Lange, and R. Carson, "EM reconstruction algorithms for emission and transmission tomography," *J. Comput. Assist. Tomogr.,* vol. 8, pp. 306-316, 1984.

[10]    L. A. Shepp, and Y. Vardi, "Maximum likelihood reconstruction for emission tomography," *IEEE Trans. Med. Imag.,* vol. 1, no. 2, pp. 113-22, 1982.

[11]    H. M. Hudson, and R. S. Larkin, "Accelerated image-reconstruction using ordered subsets of projection data," *IEEE Trans. Med. Imag.,* vol. 13, no. 4, pp. 601-609, 1994.

# 2. The role of preclinical SPECT in oncological and neurological research in combination with either CT or MRI

## *Abstract*

Preclinical imaging with SPECT combined with CT or MRI is used more and more frequently and has proven to be very useful in translational research. In this article, an overview of current preclinical research applications and trends of SPECT combined with CT or MRI, mainly in tumor imaging and neuroscience imaging, is given and the advantages and disadvantages of the different approaches are described. Today SPECT and CT systems are often integrated into a single device (commonly called a SPECT/CT system), whereas at present combined SPECT and MRI is almost always carried out with separate systems and fiducial markers to combine the separately acquired images. While preclinical SPECT/CT is most widely applied in oncology research, SPECT combined with MRI (SPECT/MRI when integrated in one system) offers the potential for both neuroscience applications and oncological applications. Today CT and MRI are still mainly used to localize radiotracer binding and to improve SPECT quantification, although both CT and MRI have additional potential. Future technology developments may include fast sequential or simultaneous acquisition of (dynamic) multimodality data, spectroscopy, fMRI along with high-resolution anatomic MRI, advanced CT procedures, and combinations of more than two modalities such as combinations of SPECT, PET, MRI and CT all together. This will all strongly depend on new technologies. With further advances in biology and chemistry for imaging molecular targets and (patho)physiological processes *in vivo*, the introduction of new imaging procedures and promising new radiopharmaceuticals in clinical practice may be accelerated.

## 2.1 Introduction

Over the past decade the use of PET, SPECT, CT and MRI in preclinical research has greatly increased due to technological advances that have resulted in significant improvements in spatial and temporal resolution as well as sensitivity [1-5]. These noninvasive imaging methods enable imaging of (patho)physiological and molecular processes over time *in vivo*, obviating the need for killing animals for each time-point being studied [6-8]. Each of these imaging modalities has unique qualities, in terms of their spatial and temporal resolution and their ability to measure morphology and/or function; the appropriate technique should be selected according to the research question. PET and SPECT allow detection of radiopharmaceuticals at nano- to picomolar concentrations *in vivo*, and have proven to be excellent tools in the translational evaluation of radiotracers. CT and MRI provide a high degree of spatial resolution that is well suited to anatomical imaging and tissue phenotyping, including volumetry, and can provide information regarding tissue physiology [9].

Due to their sensitive detection capabilities, PET and SPECT both have preeminent ability to monitor and quantify dynamic processes at a molecular level *in vivo*. Unique SPECT capabilities include: the ability to image ligands such as peptides and antibodies relatively easy with $^{99m}$Tc, $^{111}$In or iodine isotopes ($^{123}$I, $^{125}$I), the ability to measure slow kinetic processes due to the long half-life (compared to most PET tracers) of some of the commonly used radionuclides, and the ability to probe multiple molecular pathway simultaneously by detecting radionuclides with different gamma energies (multi isotope imaging). Multi isotope imaging has been demonstrated both clinically [10-13] and preclinically [14, 15]. Another advantage of SPECT over PET is that no cyclotron and associated infrastructure and complex logistics are required on site and that many tracers are readily available in the form of kits.

While in clinical imaging higher spatial resolutions can be obtained with PET than with SPECT, the opposite is clearly true in preclinical imaging in small animals. Small imaging volumes enable the use of high magnification apertures in SPECT imaging (Fig. 1), increasing sensitivity and resolution relative to their clinical counterparts [16-18]. Recently developed SPECT systems can be extended to high-resolution imaging of high-energy photons emitted by PET tracers, even simultaneously with (multiple) SPECT tracers [14]. Since some SPECT systems also enable imaging of $^{125}$I-labelled tracers (<35 keV), the gap between *in vitro* and *in vivo* studies is closed. Finally, in SPECT imaging spatial resolution and sensitivity can be adjusted by changing the size of the collimator apertures.

On the other hand, the drawbacks of SPECT include its lower sensitivity compared to PET, especially when high-resolution SPECT is desired. Moreover, SPECT tracer molecules may differ with regard to their biological properties from their nonradioactive counterparts after introduction of a radionuclide-chelator complex, which is not the case for several PET tracers in which endogenous atoms (such as hydrogen, carbon and oxygen) can be replaced by their radioactive isotopes. In addition, the dynamic capabilities of SPECT, although recently greatly improved, are often limited compared to those of PET.

In current clinical practice combining images from different tomographic modalities is common. Also in preclinical research multimodality imaging strategies are useful, as different modalities can provide highly complementary information. Spatially registered images enable localization, enhanced visualization and accurate quantification of spread and uptake of radiolabelled molecules within the anatomical context provided by CT or MRI. In addition, functional information derived from advanced CT and MRI techniques such as perfusion imaging can be related to expression and function of specific molecules as measured by PET or SPECT.

In this review we discuss recent applications and technological advances of preclinical SPECT in combination with CT or MRI in the fields of oncology and neuroscience. Overviews by others and Golestani *et al*. addressing preclinical SPECT combined with MRI and CT in other research fields, such as cardiovascular research, regenerative medicine and inflammation, have recently been published [19-22]. The space constraints of this article prevented coverage of every aspect of this exciting field, but we aimed to provide a good appreciation of the possibilities, and also the limitations and remaining challenges.
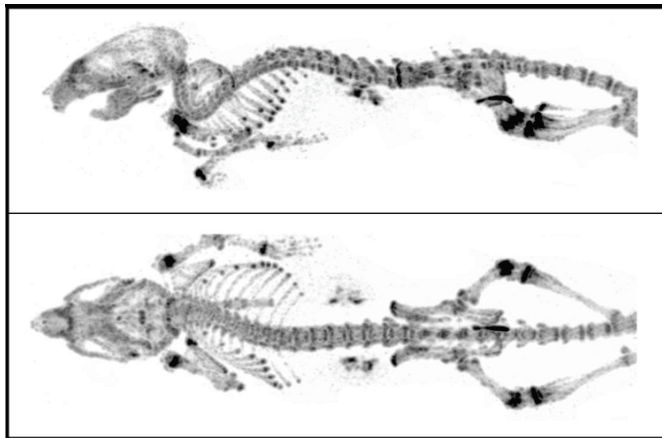


**Figure 1.** *State-of-the-art whole-body SPECT bone images acquired for 60 min with 250 MBq $^{99m}$Tc-HDP and with 0.25-mm resolution collimators (image courtesy of Oleksandra Ivashchenko, TU-Delft/MILabs B.V.)*

## 2.2 Applications of SPECT combined with CT or MRI

### 2.2.1 Tumor imaging

Hanahan and Weinberg [23, 24] introduced the notion that the tumor microenvironment plays a crucial role in the development and behavior of tumors, including receptiveness and sensitivity to treatment. The resulting understanding that cancer is a complex disease with significant involvement of the tumor stroma has led to the interest in

imaging tumor cell characteristics as well as noncancer cell components *in vivo* [25, 26], especially with regard to molecular diagnostics and drug development. Since it would be impossible to cover every aspect of this rapidly developing field, we only address some key aspects in tumor imaging and the roles that SPECT, and SPECT combined with CT or MRI have been playing in this field.

### 2.2.1.1 Imaging targets and probes

Tumors and tumor cells exhibit different characteristics compared to normal tissue and cells; this is reflected in altered physiology, tissue composition and expression of intra- and extracellular molecules [23, 24, 26-28]. All these aspects can be used as imaging targets in relation to diagnostics, drug development and treatment response assessment. SPECT probes (or tracers) can be classified according to their biodistribution and targeting characteristics, i.e. the biodistribution of some radiopharmaceuticals is determined by their chemical/physical properties, whereas that of other tracers is determined by their specific interaction with a target. For details the reader is referred to a review by Müller and Schibli [29].

Tumors are known often to display an aberrant vascular network and microcirculation, which in turn underlies features such as interstitial hypertension, hypoxia and acidosis, characteristics that contribute to malignant phenotypes and resistance to various treatments [30]. Within this environment, tumor cells can also display altered energy metabolism, as reflected in, for example, increased glucose uptake and shifted balances in metabolic products. At the preclinical level, a variety of SPECT tracers are under evaluation for use as markers for (neo)angiogenesis [31-33], hypoxia [34-37], acidosis [38-40], metabolic activity [41] and proteolytic activity [42, 43]. Moreover, MRI and to a lesser extend CT offer options for interrogating tumor physiological characteristics, either through the use of specific probes or the use of sophisticated MRI techniques, as recently reviewed by Bernsen *et al*. [9]. Besides metabolic tracers, much effort has been put into the development and validation of SPECT probes specific for tumor target molecules such as antigens, receptors or other molecules also overexpressed in tumor tissue. The use of peptides interacting with receptors [44], antibodies and antibody fragments targeting their epitopes [45], vitamin-based radiopharmaceuticals [28] and nucleoside analogues [46], significantly increases the possibilities for tumor detection, localization and staging.

Specific points of interest in translational preclinical imaging studies include efforts directed at improved tumor specificity [47], tumor uptake/retention [48] and minimized pharmacological effects [49, 50] of imaging probes. In most preclinical studies involving the use of SPECT combined with CT or MRI to date, the CT or MRI components have been mostly used to provide anatomical reference and more recently also for attenuation correction [51]. However, CT and MRI offer more than anatomical information, and some examples of the use of more sophisticated CT and MRI techniques are discussed and provided in the technology sections below.

## 2.2.1.2 Biodistribution studies/dosimetry/response assessment

In drug development, biodistribution and pharmacokinetic properties of a candidate drug or therapeutic agent are crucial for their therapeutic potential and safety in patients. After binding of a suitable radionuclide to the molecule or particle of interest, preclinical SPECT imaging provides a valuable noninvasive tool to study candidate drugs. Especially in development of targeted treatment strategies with radiolabelled molecules such as peptides, antibodies and vitamin-based analogues, SPECT imaging combined with CT or MRI has been widely used [45, 52-56]. Next to *in vivo* evaluation of such molecules, SPECT combined with CT or MRI is also being applied in the preclinical evaluation of (nano)particles for treatment and/or diagnosis of cancer. Various studies have investigated the biodistribution and therapeutic potential of, for example, liposomes [57-61], radiolabelled superparamagnetic iron oxide nanoparticles and $^{166}$Ho microspheres ($^{166}$HoAcAcMS), using multimodality imaging approaches with SPECT/CT and SPECT/MRI [62, 63]. The combined imaging data allow accurate assessment of biodistribution and retention as well as dosimetry calculations.

Many of the imaging biomarkers addressed in the previous section are also being evaluated as markers to monitor response to treatment. Elimination of tumor cells might be accompanied by loss of tracer uptake directed at tumor-associated antigens or decreased metabolic activity, whereas changes in vascular properties and tissue hypoxia may be expected after antiangiogenic therapies, allowing these markers to be used for response assessment. While such an approach may appear fairly straightforward, some limitations and pitfalls need to be taken into account. Loss of tumor-associated antigen expression may also be a result of changed tumor physiology not related to tumor cell death [64]. Another process of interest as an imaging biomarker for response is apoptosis [65, 66]. Expectations were raised that visualization and quantification of apoptosis, as a more specific and relevant marker of cell death, may provide better specificity for assessing actual tumor cell elimination following treatment. Apoptosis imaging using a tracer specific for annexin could reveal early tumor cell death after chemotherapy [65], but its value as a robust marker for treatment response still needs to be established.

For the assessment of potential treatment efficacy, Bol *et al.* recently reported on the added value of dual modality imaging using SPECT and MRI [67]. In a rat model of neuroendocrine pancreatic tumor, radiolabelled peptide uptake was assessed in conjunction with measurement of tumor perfusion using DCE-MRI. A substantial correlation between tumor uptake of $^{111}$In-DTPA-octreotide and tumor perfusion parameters was observed (Fig. 2). It was shown that even in tumor areas with high receptor expression no peptide uptake occurred when perfusion was low, indicating that combined SPECT and MRI may be useful in treatment planning and/or response prediction in patients treated with PRRT.

Imaging of cell trafficking has also been an area of interest in which SPECT in combination with either CT or MRI has been employed, an approach that has already been part of clinical routine for several decades for identifying infection or inflammation sites by leucocyte scintigraphy [68]. Recently, the interest in *in vivo* cell tracking has received a tremendous boost from the realization that knowledge about the *in vivo* fate of infused cells is crucial to the development of safe and effective cell-based therapeutic strategies, including

stem cell therapy [69, 70]. SPECT has largely been used to investigate the short-term fate of transplanted cells labelled with radio- tracers such as ^{111}In-oxine, ^{99m}Tc-hexamethylpropylene amine oxine (HMPAO) and ^{111}In-tropolone as intracellular labels [71]. However, due to the lack of anatomical information and the limited life-time of the radionuclides, preventing longitudinal follow up, other imaging techniques such as MRI have been widely used as well [72]. Since MRI also has some specific limitations for *in vivo* cell tracking such as low sensitivity and specificity, and challenges in quantification of the MRI probe, alternative approaches have been sought, with specific interest in reporter gene technology [70]. For SPECT the sodium iodide symporter gene (NIS) and the herpes simplex virus type 1 thymidine kinase gene (HSV1-tk) are so far the most commonly used reporter genes in combination with radioactive substrates [73, 74]. Reporter gene technology with these and other reporter genes, e.g. norepinephrine transporter and the somatostatin receptor, is being used not only in *in vivo* cell tracking applications for cell-based therapy [75, 76], but also to monitor metastatic spread of tumor cells [77-79], as well as gene delivery and expression of genes in targeted gene therapy approaches [80, 81].

Finally, in medical research, the successful choice of a target molecule that is a key disease biomarker has the potential to lead to the development not only of a molecular imaging probe, but also of a therapeutic agent to inhibit the disease process. Examples include peptides [55, 82, 83], antibodies or fragments thereof [84-87], and nanoparticles [26, 88], similar compounds or particles that can be labelled with radionuclides for either imaging or therapy. Receptor targeting with small radiolabelled peptides for receptor-targeted tumor imaging (PET and SPECT) as well as for radionuclide therapy [89] provide good examples of such theranostic potential in nuclear oncology and have paved the way for further developments in this field.



AUC60      SPECT      Overlay
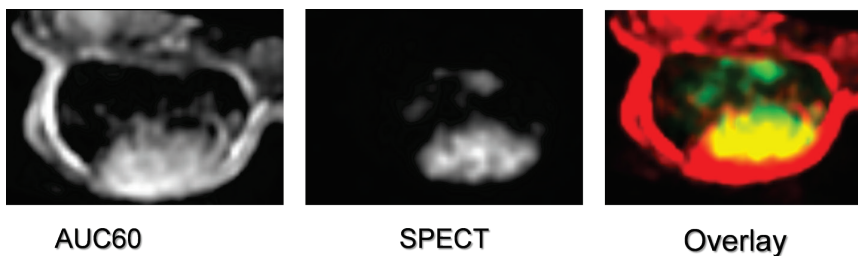
**Figure 2.** *Multimodality imaging of tumor uptake of targeted radiolabelled peptide and tumor perfusion. Rats bearing a syngeneic, somatostatin receptor overexpressing, neuroendocrine pancreatic tumor, were imaged by SPECT/CT and MRI to study tumor uptake of a ^{111}In-labelled somatostatin analogue ([^{111}In-DTPA]octreotide) and tumor perfusion by DCE-MRI respectively. Left Tumor perfusion depicted by the AUC value over the first 60 s as assessed by DCE-MRI; center tumor uptake of radiolabelled [^{111}In-DTPA] octreotide of the same tumor section as imaged by MRI; right color-coded overlay of the MR image and the SPECT image with MRI values depicted in red and SPECT values depicted in green. For correct image registration, MRI data were resampled to match the lower resolution of the SPECT/CT images (image courtesy of Joost Haeck and Karin Bol, Erasmus MC)*

## 2.2.2 Neuroscience

### 2.2.2.1 Preclinical SPECT studies in small laboratory animal models of neurodegenerative diseases

Parkinson's disease (PD) is a neurodegenerative disease characterized by loss of neurons producing dopamine (DA), and consequently loss of the DA transporter (DAT) [90-95]. Preclinical SPECT studies initially focused on the feasibility of detecting striatal DAT binding in small laboratory animals per se [96, 97]. In the past decade, pinhole SPECT studies have shown the possibility of detecting loss of striatal DAT binding in rodent models of PD using [123I]FP-CIT and [123I]β-CIT as radiotracers [98, 99]. Initially, single-pinhole SPECT systems were used to image DAT [90, 100], and the SPECT images were coaligned with MR images (or templates) acquired on clinical MRI scanners (using dedicated coils), with or without the use of external markers [99, 101, 102]. Another recent study, however, used a preclinical system with high-resolution parallel-hole collimators (X-SPECT system) to evaluate DAT loss (using [123I]altropane as a radiotracer) in a rat model of PD, and the SPECT images were registered with CT images [103]. Another DAT ([123I]FP-CIT) SPECT study in a mouse model of PD used a double-headed gamma camera equipped with a multi-pinhole aperture. The SPECT images were not coaligned with CT or MR images [104, 105]. Finally, MRI is an important tool in the field of neuroimaging. In this regard, it is of interest that Lee *et al*. proposed an image registration algorithm which can be used to register individual DAT SPECT ([99mTc]TRODAT was used as a radiotracer on a NanoSPECT/CT system) and brain MR images (acquired on a 3-T system) in rodent models of PD without using external markers [106].

Neurodegenerative diseases like multiple system atrophy, progressive supranuclear palsy and Huntington's disease, are characterized by loss of striatal DA $D_2$ receptors [91]. A study published in 2002 demonstrated the feasibility of pinhole SPECT for measuring striatal DA $D_{2/3}$ receptor binding in the mouse brain *in vivo* [107]. [123I]IBF was used to assess striatal $D_{2/3}$ receptor binding and SPECT images were not registered with CT or MR images. Not long afterwards, another study in rats confirmed the feasibility of assessing DA $D_{2/3}$ receptor binding *in vivo*, using [123I]IBZM as radiotracer and a dedicated small-animal SPECT system [108]. In that study, SPECT images were not registered with CT or MR images, but a region of interest template was constructed and used to evaluate receptor binding [108].

Scherfler *et al*. showed the ability of single-pinhole SPECT to detect loss of striatal DA $D_{2/3}$ receptors in a rat model of Huntington's disease [109]. In that study, the [123I]IBZM SPECT images were registered on a MRI template. Importantly, *in vivo* [123I]IBZM binding was highly correlated with the loss of medium-sized spiny neurons that express DA $D_2$ receptors demonstrated *ex vivo* [110].

Alzheimer's disease (AD) is the most common dementia in humans, and is characterized by the deposition of β-amyloid plaques and neurofibrillary tangles. PET tracers have been developed successfully to image this neuropathology [111]. The deposition of amyloid has also been evaluated in micro-PET studies in animal models of AD [112, 113].

SPECT tracers have also been developed for labelling of amyloid plaques [112]. Although [$^{123}$I]IMPY shows high affinity for amyloid *in vitro* and amyloid plaques in post-mortem brain tissue of AD patients and animal models of AD, the specific to nonspecific binding ratios are too low to be of value for studies in animal models of AD [114, 115].

### 2.2.2.2 Preclinical SPECT studies in small laboratory animals relevant to studies on psychosis or addiction

A consistent finding of imaging studies in drug addiction is loss of striatal DA D$_{2/3}$ receptors. An increase in D$_2$ receptor expression may therefore be beneficial in its treatment [116]. Interestingly, some drugs may induce an increase in D$_{2/3}$ receptors [117-119], which has been supported by SPECT imaging in rats [117]. In the latter study an ultra-high-resolution pinhole SPECT system was used (U-SPECT-II), but SPECT images were not registered with CT or MR images. Due to the high spatial as well as temporal resolution of this system, changes in DAT occupancy by cocaine over time can be studied in the mouse *in vivo* [120]. Alterations in the expression of DA D$_{2/3}$ receptors have been reported in schizophrenia. In a recent study, in which the SPECT images were registered with CT images (X-SPECT/CT system), decreases in DA D$_{2/3}$ receptor availability in the striatum and midbrain have been shown in a rat model of schizophrenia using [$^{123}$I]epidepride as radiotracer [121]. DA D$_{2/3}$ receptor imaging can be used to evaluate DA release [122]. Increased DA release has been reported in schizophrenia, whereas DA release may be reduced in cocaine dependency [123, 124]. Interestingly, recent pinhole SPECT studies in mice and rats have also shown the ability to measure DA release [125, 126]. In both studies, SPECT images were not registered with CT or MR images.

### 2.2.2.3 Preclinical SPECT studies focused on brain perfusion

Brain perfusion studies may be of relevance for the study of, for example, the aetiology of stroke. Using a multi-pinhole SPECT system (NanoSPECT), the kinetics of the perfusion tracers [$^{99m}$Tc]HMPAO and [$^{99m}$Tc]ECD were compared directly in control mice. SPECT images were registered on a MRI template [127]. It was shown that [$^{99m}$Tc]ECD washout was much faster than that of [$^{99m}$Tc]HMPAO. In another study, [$^{123}$I]iodoamphetamine was used to assess hypoperfusion in infarcted brain areas in mice [128]. A single-pinhole collimator system was used, and CT and MRI images acquired on other systems were used for the alignment of the SPECT images. Finally, Ceulemans *et al*. performed brain perfusion SPECT studies ([$^{99m}$Tc]HMPAO, 1-mm pinhole collimator positioned on a dual-head gamma camera, coregistered on individual CT images) to quantify the infarct size in rats [129].

Deep brain stimulation (DBS) is commonly used in the treatment of PD, but has recently also been used in the treatment of other neuropsychiatric disorders [130]. Interestingly, Wyckhuys *et al*. studied the effects of DBS on brain perfusion in rats [131]. In all rats, they acquired individual brain perfusion studies with SPECT (U-SPECT-II) after DBS

(stimulator on and off), micro-CT scans and, after the animals were killed and the electrodes removed, MRI scans on a clinical MRI scanner using a dedicated rat brain coil [131]. After registration of the images and analysis of each voxel, hypoperfusion induced by DBS could be located accurately in small brain areas (Fig. 3). This approach highlights the potential of multimodality imaging to evaluate and locate the effects of interventions/treatments in small brain areas of rodents.
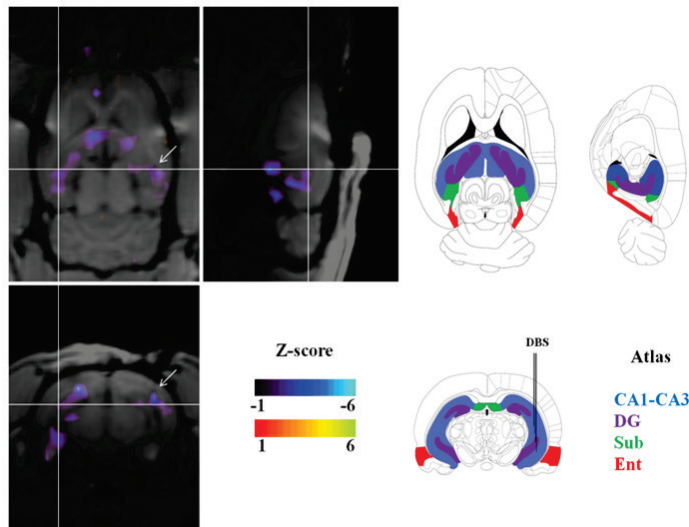


**Figure 3.** *Coronal, sagittal and transverse anatomical T1-weighted MRI scans coregistered with colored subtraction SPECT data illustrating the changes in regional cerebral blood flow induced by deep brain stimulation (DBS). The white arrows indicate a DBS electrode artefact in the hippocampus. The corresponding sections, modified from the rat brain atlas of Paxinos and Watson [132] are shown on the right (CA1-CA3; DG dentate gyrus, Sub subiculum, Ent entorhinal cortex). The different hippocampal structures are colored and the position of the DBS electrode is indicated (courtesy Tine Wyckhuys [131])*

### 2.2.2.4 Preclinical SPECT studies focused on neurooncology

Micro-SPECT studies have also been performed successfully in the field of neurooncology. For example, Yang *et al*. recently showed the feasibility of using [$^{99m}$Tc]DTPA to study the integrity of the blood–brain barrier and tumor activity in glioma-bearing rats [133]. A preclinical pinhole SPECT/CT system (FLEX Triumph) was used which offers the ability to coalign the SPECT and CT images [133]. Angiogenesis is essential for tumor growth. Furthermore, malignant cells can release vascular endothelial growth factors (VEGFs) which are important promoters and regulators of angiogenesis. SPECT studies showed the possibility of imaging VEGF receptors in rats. [$^{99m}$Tc]HYNIC-VEGF uptake was increased in glioma-bearing rats pretreated with a VEGR receptor tyrosine kinase inhibitor [64]. In that study, SPECT images were acquired on a dedicated multiple-pinhole SPECT

system (NanoSPECT), but the SPECT images were not registered with CT or MR images. In addition, Huang *et al*. evaluated a 188Re-labelled liposome as a diagnostic and therapeutic agent in glioma-bearing rats [60], using a preclinical multiple- pinhole SPECT/CT system (NanoSPECT/CT). Importantly, uptake in the brain tumor could be visualized, and specific binding was confirmed histopathologically [121]. Another study in glioma-bearing rats evaluated new treatment strategies for glioma, and imaged [99mTc]-labelled nanoparticles using a clinical SPECT system [134]. Finally, SPECT/CT (parallel hole SPECT system) studies were performed to examine successfully glioblastoma xenografts that were located subcutaneously in mice using, for example, [125I]-labelled monoclonal antibodies against chemokine receptor 4 [135].

## 2.3 Technology of SPECT combined with CT or MRI

### 2.3.1 Combined imaging approaches/systems, introduction

In order to fully benefit from multimodality imaging, accurate spatial registration of the images is crucial. Below we address ways to adequately combine SPECT with CT or MRI.

#### 2.3.1.1 Side-by-side systems

In contrast to clinical imaging of patients, small animals can be transported – including the bed – between imaging devices with gentle fixation with tape preventing movement of the animal on the bed. This requires beds that can be easily, rigidly and reproducibly mounted on different scanners (Fig. 4). Multimodal fiducial markers attached to the animal (or bed) or a premeasured transformation matrix can be used for spatial coregistration [136, 137]. Such side-by-side use of separate scanners offers flexibility in adding and/or replacing individual modalities while both systems can be used in parallel facilitating higher throughput. However, maintaining anesthesia may be a challenge during transport, especially when the machines are far apart.
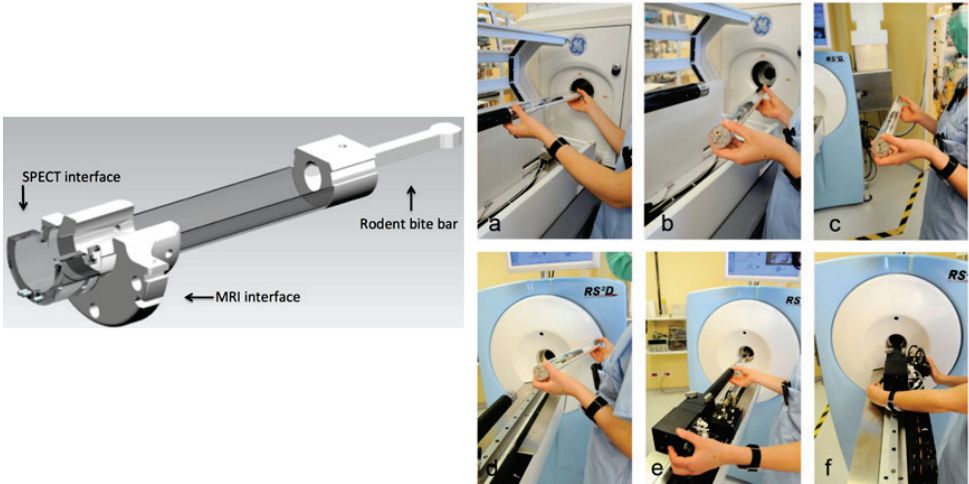
**Figure 4.** *Example of the principle of a transferable bed system. Left: Schematic drawing of an animal bed with tailored interfaces for mounting into compatible cradles in SPECT and MRI scanners. Right: Step-by-step photo representation of the transfer from a SPECT scanner to a MRI scanner: **(a)** at the end of SPECT/CT acquisition; **(b)** the animal bed is unplugged; **(c,d)** the animal and bed are moved towards the MRI scanner ; **(e,f)** the bed is docked and positioned inside the magnet followed by MRI acquisition (image courtesy of Philippe Choquet)*

### 2.3.1.2 In-line systems

A second approach to imaging with SPECT in combination with CT or MRI is to mount the separate modalities in-line (i.e. back-to-back) on a single gantry (Fig. 5). When the bed moves in the axial direction, images of the different modalities can be acquired shortly after each other. With this approach it is easier to continuously provide anesthesia and no animal handling between scans is required. However, simultaneous use of the separate modalities is not possible, limiting flexibility and through-put. Furthermore, close proximity of the SPECT and MRI systems limits the MRI field strengths that can be applied potentially resulting in impractically long MRI acquisition times. MRI-compliant SPECT hardware will most likely tack- le these problems in the future.
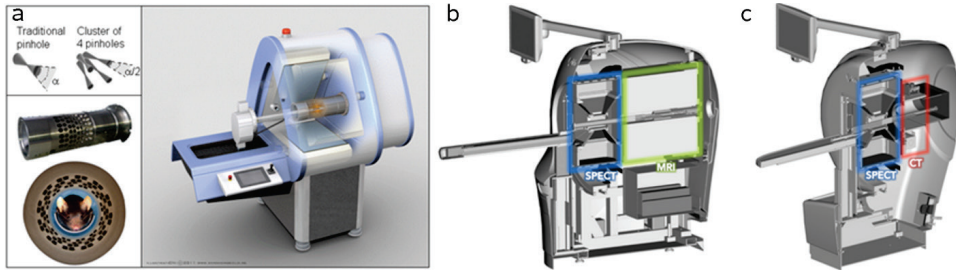
**Figure 5.** *Combined modality approaches. (a) Drawing of a SPECT/CT system in which the SPECT part can also image 511 keV photons to perform simultaneous SPECT/PET (from M.C. Goorden et al., JNM 2013). (b,c) Cross-sectional views of (b) a proposed SPECT/MRI system and (c) a SPECT/CT system. For (b) and (c) the SPECT system is placed in front while the MRI or CT system is placed at the back of the scanner ((b,c) courtesy of Mediso Medical Imaging Systems)*

### 2.3.1.3 Integrated systems

Figure 6 shows an example of a system where the SPECT and CT are mounted on the same gantry. An advantage is that fast sequential SPECT and CT acquisition can be performed with minimal or even without shifting of the bed. One of the drawbacks of this approach is space constraints, since the number and/or size of detectors that can be used for each modality is limited, preventing e.g. stationary and full angular SPECT approaches.
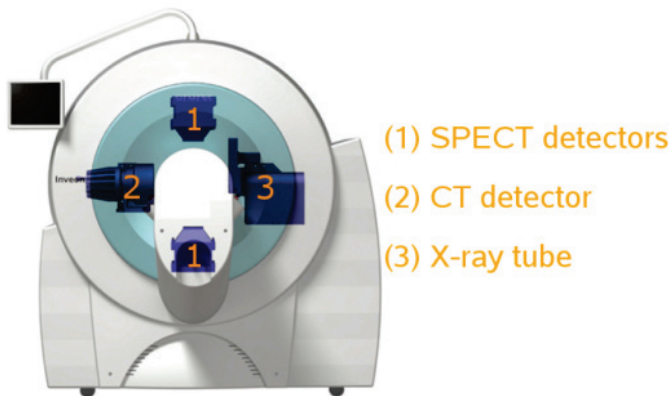


**Figure 6.** *Diagram of an integrated SPECT/CT system showing two SPECT detectors, a CT detector and an X-ray tube, all rotating on the same gantry (image courtesy of Siemens Healthcare)*

## 2.3.2 SPECT combined with CT

Implementation of multi-pinhole collimators with high pinhole magnification factors in dedicated small-animal SPECT systems has helped overcome the limitation of poor sensitivity and spatial resolution. Efforts have been made to keep the heavy SPECT detectors stationary [16, 138-140] in order to obviate the need for regular geometric parameter calibration and to enable fast dynamic imaging [5, 138], while sensitivity and resolution in organ and tumor imaging have been increased [140-142].

CT systems currently used in preclinical SPECT/CT usually contain a variable energy X-ray tube. Tube voltage and current are in the range of 20–80 kVp and 0.2–1 mA, respectively. Tube current typically decreases with decreasing focal spot size. Reconstructed resolutions of well below 100 μm are achieved using microfocus X-ray tubes with focal spot sizes down to a few micrometers.

## 2.3.3 SPECT combined with MRI

Exposure to ionizing radiation from CT imaging may influence study outcomes [143-147]. Furthermore, image contrast of CT is often suboptimal for soft tissues such as brain and tumors. These two limitations have been strong incentives for the current efforts to integrate SPECT and MRI. A combined SPECT/MRI platform was first proposed in 2007 by Breton *et al*. who used a single pinhole SPECT system adjacent to a 0.1-T magnet [148]. The low MRI field strength made this solution suboptimal for use in routine preclinical research. However, since then systems combining SPECT and MRI have been introduced with both higher SPECT sensitivity and resolution and higher MRI field strengths. One solution involves the use of a robotic rotation/translation stage that automatically transfers the animal between the separately spaced MRI system and other modalities (Fig. 7). Using such an approach the MRI unit is still positioned in-line with the other modalities, while avoiding the effects of fringe magnetic fields. Similar to hybrid SPECT/CT scanners, recent efforts also include an in-line hybrid SPECT/MRI system, in which the SPECT subsystem is placed in front of the MRI system (Fig. 5b). In attempts to perform simultaneous SPECT and MR imaging, SPECT inserts for MRI systems have been developed [149, 150]. They have a stationary detector set-up and MRI-compatible collimators and detectors, although today these systems are still in early stages of development.
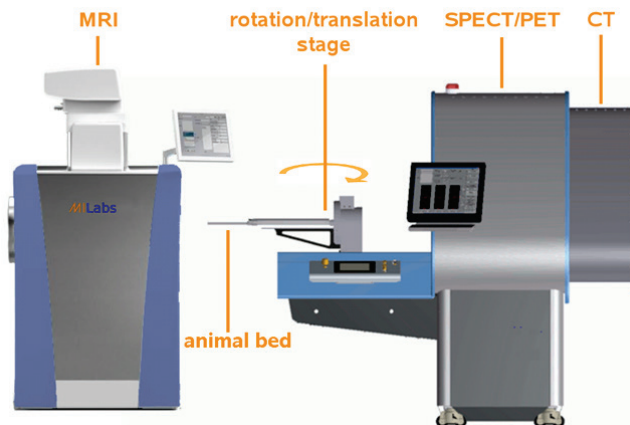
**Figure 7.** *One of the commercial side-by-side solutions for integrating 1.5-T or 3-T MRI with SPECT and other modalities. In this example a robotic rotation/translation stage automatically transfers the animal between the systems. In this set-up the MRI system is integrated in-line with the other modalities, while avoiding possible interference of the fringe magnetic field of the MRI system with the other modalities (image courtesy of MILabs B.V.)*

## 2.3.4 Quantification in animal SPECT combined with CT or MRI

Preclinical SPECT systems are mostly based on the use of pinholes that magnify projections of the radionuclide distribution on detectors. For proper quantification of radioactivity, image-degrading factors such as distance-dependent collimator response and sensitivity, as well as photon attenuation and scatter, need to be taken into account.

### 2.3.4.1 Distance-dependent collimator response and sensitivity

To maximize spatial resolution in SPECT, thereby minimizing partial volume effects, and to reduce quantification errors, distance-dependent collimator resolution and sensitivity need to be taken into account in image reconstruction (i.e. resolution recovery methods). In this context it is also important to accurately calibrate the system's geometrical parameters [151-155]. Methods that also account for more complex effects, such as detector and collimator imperfections include measurements of the system's response with a point source at many discrete locations in the field of view of the camera [156-158]. Such methods can also be combined with advanced interpolation schemes [159] and have enabled very high spatial resolution.

### 2.3.4.2 Attenuation and scatter

Since the likelihood of scatter events in small animals is much smaller than in humans, the effects of photon attenuation and scatter in tissue are smaller than in clinical SPECT [160]. Simulation studies in mouse-sized phantoms have shown that attenuation can degrade

quantitation accuracy by up to −18% (^{99m}Tc or ^{111}In) or −41% (^{125}I) [161]. Accounting for scatter and attenuation is especially important for imaging tracers that emit low gamma-ray energies such as [125]I [162, 163]. Several methods have been published for attenuation and scatter correction [163-167]. First order attenuation correction methods as proposed in 1978 by Chang [168] seem to be sufficient for small-animal SPECT [167]. Attenuation correction maps can be derived from CT images [163], optical images [167] and MR images [164].

Because of the low amount of scatter in small subjects, simple energy-window-based corrections [169-171] are often sufficient for ^{99m}Tc, ^{123}I and [111]In [163, 165, 167]. However, in the case of multipeak spectra and multiradionuclide imaging, it is important that many scatter windows are available, or that data are acquired in list mode (i.e. that for each detected photon its position, its energy and its detection time are stored). Scatter in pinhole apertures is low [172], although in multienergy and in multiradionuclide SPECT, scatter and photon penetration in the collimator can be a significant issue, e.g. with a combination of SPECT and PET tracers used on a SPECT camera, although in such a case excellent quantitative images have been recently obtained using a dedicated high-energy (clustered-)pinhole collimator and window-based scatter corrections [14].

## 2.4 Concluding remarks and future perspectives

Recent advances in small-animal SPECT/CT and SPECT/MRI devices, radiochemistry, probe development, target finding and suitable animal models have provided more advanced and increased applications of these combined imaging strategies.

In most preclinical SPECT imaging studies to date, CT or MRI merely fulfil a supportive role to provide anatomical reference and in some cases attenuation correction. In small laboratory animals, acquisition of detailed anatomical information, performance of dynamic scans or functional imaging with CT has specific challenges compared to imaging in humans. To reach diagnostic image quality high CT radiation doses and/or large volumes of contrast agent are necessary. These aspects are not compatible with longitudinal studies, since they may severely affect the wellbeing of animals. New developments in small-animal CT [173-178] and the use of new contrast agents for CT should provide better image quality at lower radiation doses and/or with lower volumes of contrast agent.

MRI offers detailed anatomical imaging of soft tissues compatible with longitudinal studies. Separately spaced SPECT and MRI systems can pose challenges with respect to image registration, imaging times and anesthesia times; the effects of these issues can potentially influence study results. On the other hand, physical integration of SPECT and MRI technologies is hampered by various incompatibilities; the components and working mechanisms of the separate modalities currently degrade the other's performance.

A major benefit of higher magnetic field strengths is that more signal is provided which can be used to shorten acquisition times, but higher magnetic field strengths do not always guarantee higher image quality per se. Currently, most high-field magnets are cooled with cryogenic liquids. One of the main drivers towards small MRI systems is the

development of cryogen-free magnets or systems using helium gas instead of liquid helium. This development could lead to significant reductions in the size, site requirements and cost of high-field MRI systems. Today, such helium gas-based commercial MRI systems are limited to 3-T.

While not covered in detail in this review, an extremely important aspect to consider during imaging is animal welfare. Animal handling and especially anesthesia is demanding to the animal and can severely affect the outcome of imaging studies [35, 179-181]. Also issues regarding radiation doses will have to be taken into account [143, 144, 182, 183].

Taking these issues into account, further advances in technology and chemistry, for example the development of new imaging procedures and promising new radiopharmaceuticals, for imaging molecular targets as well as (patho)physiological processes *in vivo*, the step from bench to bedside might become more successful and shorter; e.g. accelerating the introduction of new imaging procedures and promising new radiopharmaceuticals into clinical practice.

## *Bibliography*

[1]     S. Deleye, R. Van Holen, J. Verhaeghe, S. Vandenberghe, S. Stroobants, and S. Staelens, "Performance evaluation of small-animal multipinhole muSPECT scanners for mouse imaging," *Eur. J. Nucl. Med. Mol. Imaging,* vol. 40, no. 5, pp. 744-58, 2013.

[2]     A. Greco, G. Fiumara, S. Gargiulo, M. Gramanzini, A. Brunetti, and A. Cuocolo, "High-resolution positron emission tomography/computed tomography imaging of the mouse heart," *Exp. Physiol.,* vol. 98, no. 3, pp. 645-51, 2013.

[3]     A. W. Sauter, H. F. Wehrl, A. Kolb, M. S. Judenhofer, and B. J. Pichler, "Combined PET/MRI: one step further in multimodality imaging," *Trends Mol. Med.,* vol. 16, no. 11, pp. 508-15, 2010.

[4]     S. J. Schambach, S. Bag, L. Schilling, C. Groden, and M. A. Brockmann, "Application of micro-CT in small animal imaging," *Methods,* vol. 50, no. 1, pp. 2-13, 2010.

[5]     P. E. B. Vaissier, M. C. Goorden, B. Vastenhouw, F. van der Have, R. M. Ramakers, and F. J. Beekman, "Fast spiral SPECT with stationary gamma-cameras and focusing pinholes," *J. Nucl. Med.,* vol. 53, no. 8, pp. 1292-9, 2012.

[6]     T. F. Massoud, and S. S. Gambhir, "Molecular imaging in living subjects: seeing fundamental biological processes in a new light," *Genes Dev.,* vol. 17, no. 5, pp. 545-80, 2003.

[7]     B. J. Pichler, H. F. Wehrl, and M. S. Judenhofer, "Latest advances in molecular imaging instrumentation," *J. Nucl. Med.,* vol. 49 Suppl 2, pp. 5S-23S, 2008.

[8]     R. Weissleder, and U. Mahmood, "Molecular imaging," *Radiology,* vol. 219, no. 2, pp. 316-33, 2001.

[9]     M. R. Bernsen, A. Ruggiero, M. van Straten, G. Kotek, J. C. Haeck, P. A. Wielopolski, and G. P. Krestin, "Computed tomography and magnetic resonance imaging," *Recent Results Cancer Res.,* vol. 187, pp. 3-63, 2013.

[10]    K. H. Ma, W. S. Huang, C. H. Chen, S. Z. Lin, S. P. Wey, G. Ting, S. D. Wang, H. W. Liu, and J. C. Liu, "Dual SPECT of dopamine system using [99mTc]TRODAT-1 and [123I]IBZM in normal and 6-OHDA-lesioned formosan rock monkeys," *Nucl. Med. Biol.,* vol. 29, no. 5, pp. 561-7, 2002.

[11]    A. Nakazawa, K. Ikeda, Y. Ito, M. Iwase, K. Sato, R. Ueda, and Y. Dohi, "Usefulness of dual 67Ga and 99mTc-sestamibi single-photon-emission CT scanning in the diagnosis of cardiac sarcoidosis," *Chest,* vol. 126, no. 4, pp. 1372-6, 2004.

[12]   A. Sanchez-Crespo, J. Petersson, S. Nyren, M. Mure, R. W. Glenny, J. O. Thorell, H. Jacobsson, S. G. Lindahl, and S. A. Larsson, "A novel quantitative dual-isotope method for simultaneous ventilation and perfusion lung SPET," *Eur. J. Nucl. Med. Mol. Imaging,* vol. 29, no. 7, pp. 863-75, 2002.

[13]   P. Weinmann, M. Faraggi, J. L. Moretti, and P. Hannequin, "Clinical validation of simultaneous dual-isotope myocardial scintigraphy," *Eur. J. Nucl. Med. Mol. Imaging,* vol. 30, no. 1, pp. 25-31, 2003.

[14]   M. C. Goorden, F. van der Have, R. Kreuger, R. M. Ramakers, B. Vastenhouw, J. P. Burbach, J. Booij, C. F. Molthoff, and F. J. Beekman, "VECTor: a preclinical imaging system for simultaneous submillimeter SPECT and PET," *J. Nucl. Med.,* vol. 54, no. 2, pp. 306-12, 2013.

[15]   M. Melis, R. Valkema, E. P. Krenning, and M. de Jong, "Reduction of renal uptake of radiolabeled octreotate by amifostine coadministration," *J. Nucl. Med.,* vol. 53, no. 5, pp. 749-53, 2012.

[16]   F. J. Beekman, F. van der Have, B. Vastenhouw, A. J. van der Linden, P. P. van Rijk, J. P. Burbach, and M. P. Smidt, "U-SPECT-I: a novel system for submillimeter-resolution tomography with radiolabeled molecules in mice," *J. Nucl. Med.,* vol. 46, no. 7, pp. 1194-200, 2005.

[17]   O. Ivashchenko, F. van der Have, J. Villena, and F. J. Beekman, "Quarter millimeter resolution pre-clinical SPECT with quarter-mm pinholes.," *Eur. J. Nucl. Med. Mol. Imaging*, In Press.

[18]   N. U. Schramm, G. Ebel, U. Engeland, T. Schurrat, M. Behe, and T. M. Behr, "High-resolution SPECT using multipinhole collimation," *IEEE Trans. Nucl. Sci.,* vol. 50, no. 3, pp. 315-320, 2003.

[19]   R. A. de Kemp, F. H. Epstein, C. Catana, B. M. Tsui, and E. L. Ritman, "Small-animal molecular imaging methods," *J. Nucl. Med.,* vol. 51, no. Suppl, pp. 18S-32S, 2010.

[20]   R. Golestani, C. Wu, R. A. Tio, C. J. Zeebregts, A. D. Petrov, F. J. Beekman, R. A. Dierckx, H. H. Boersma, and R. H. Slart, "Small-animal SPECT and SPECT/CT: application in cardiovascular research," *Eur. J. Nucl. Med. Mol. Imaging,* vol. 37, no. 9, pp. 1766-77, 2010.

[21]   A. Kielland, and H. Carlsen, "Molecular imaging of transcriptional regulation during inflammation," *J. Inflamm. (Lond,)* vol. 7, pp. 20, 2010.

[22]   A. J. Studwell, and D. N. Kotton, "A shift from cell cultures to creatures: in vivo imaging of small animals in experimental regenerative medicine," *Mol. Ther.,* vol. 19, no. 11, pp. 1933-41, 2011.

[23]   D. Hanahan, and R. A. Weinberg, "The hallmarks of cancer," *Cell,* vol. 100, no. 1, pp. 57-70, 2000.

[24]   D. Hanahan, and R. A. Weinberg, "Hallmarks of cancer: the next generation," *Cell,* vol. 144, no. 5, pp. 646-74, 2011.

[25]   F. Cavallo, C. De Giovanni, P. Nanni, G. Forni, and P. L. Lollini, "2011: the immune hallmarks of cancer," *Cancer Immunol. Immunother.,* vol. 60, no. 3, pp. 319-26, 2011.

[26]   E. Ruoslahti, S. N. Bhatia, and M. J. Sailor, "Targeting of drugs and nanoparticles to tumors," *J. Cell Biol.,* vol. 188, no. 6, pp. 759-68, 2010.

[27]   K. Movahedi, S. Schoonooghe, D. Laoui, I. Houbracken, W. Waelput, K. Breckpot, L. Bouwens, T. Lahoutte, P. De Baetselier, G. Raes, N. Devoogdt, and J. A. Van Ginderachter, "Nanobody-based targeting of the macrophage mannose receptor for effective in vivo imaging of tumor-associated macrophages," *Cancer Res.,* vol. 72, no. 16, pp. 4165-77, 2012.

[28]   C. Muller, "Folate based radiopharmaceuticals for imaging and therapy of cancer and inflammation," *Curr. Pharm. Des.,* vol. 18, no. 8, pp. 1058-83, 2012.

[29]   C. Muller, "Single photon emission computed tomography tracer.," *Recent Results Cancer Res.,* vol. 187, pp. 65-105, 2013.

[30]   P. Vaupel, "Pathophysiology of solid tumors," *The Impact of Tumor Biology on Cancer Treatment and Multidisciplinary Strategies*, M. Molls, P. Vaupel, C. Nieder and M. S. Anscher, eds., pp. 51-92, Heidelberg: Springer-Verlag, 2009.

[31]   S. Bredow, M. Lewin, B. Hofmann, E. Marecos, and R. Weissleder, "Imaging of tumour neovasculature by targeting the TGF-beta binding receptor endoglin," *Eur. J. Cancer,* vol. 36, no. 5, pp. 675-81, 2000.

[32]    I. Tsiapa, G. Loudos, A. Varvarigou, E. Fragogeorgi, D. Psimadas, T. Tsotakos, S. Xanthopoulos, D. Mihailidis, P. Bouziotis, G. C. Nikiforidis, and G. C. Kagadis, "Biological evaluation of an ornithine-modified (99m)Tc-labeled RGD peptide as an angiogenesis imaging agent," *Nucl. Med. Biol.,* vol. 40, no. 2, pp. 262-72, 2013.

[33]    Y. Zhou, S. Chakraborty, and S. Liu, "Radiolabeled Cyclic RGD Peptides as Radiotracers for Imaging Tumors and Thrombosis by SPECT," *Theranostics,* vol. 1, pp. 58-82, 2011.

[34]    H. Fujii, M. Yamaguchi, K. Inoue, Y. Mutou, M. Ueda, H. Saji, S. Kizaka-Kondoh, N. Moriyama, and I. O. Umeda, "In vivo visualization of heterogeneous intratumoral distribution of hypoxia-inducible factor-1alpha activity by the fusion of high-resolution SPECT and morphological imaging tests," *J. Biomed. Biotechnol.,* vol. 2012, pp. 262741, 2012.

[35]    V. Kersemans, B. Cornelissen, R. Hueting, M. Tredwell, K. Hussien, P. D. Allen, N. Falzone, S. A. Hill, J. R. Dilworth, V. Gouverneur, R. J. Muschel, and S. C. Smart, "Hypoxia imaging using PET and SPECT: the effects of anesthetic and carrier gas on [Cu]-ATSM, [Tc]-HL91 and [F]-FMISO tumor hypoxia accumulation," *PLoS ONE,* vol. 6, no. 11, pp. e25911, 2011.

[36]    S. Kimura, I. O. Umeda, N. Moriyama, and H. Fujii, "Synthesis and evaluation of a novel (99m)Tc-labeled bioreductive probe for tumor hypoxia imaging," *Bioorg. Med. Chem. Lett.,* vol. 21, no. 24, pp. 7359-62, 2011.

[37]    I. O. Umeda, K. Tani, K. Tsuda, M. Kobayashi, M. Ogata, S. Kimura, M. Yoshimoto, S. Kojima, K. Moribe, K. Yamamoto, N. Moriyama, and H. Fujii, "High resolution SPECT imaging for visualization of intratumoral heterogeneity using a SPECT/CT scanner dedicated for small animal imaging," *Ann. Nucl. Med.,* vol. 26, no. 1, pp. 67-76, 2012.

[38]    M. Bauwens, M. De Saint-Hubert, J. Cleynhens, L. Brams, E. Devos, F. M. Mottaghy, and A. Verbruggen, "Radioiodinated phenylalkyl malonic acid derivatives as pH-sensitive SPECT tracers," *PLoS ONE,* vol. 7, no. 6, pp. e38428, 2012.

[39]    S. Macholl, M. S. Morrison, P. Iveson, B. E. Arbo, O. A. Andreev, Y. K. Reshetnyak, D. M. Engelman, and E. Johannesen, "In vivo pH imaging with (99m)Tc-pHLIP," *Mol. Imaging Biol.,* vol. 14, no. 6, pp. 725-34, 2012.

[40]    D. Weerakkody, A. Moshnikova, M. S. Thakur, V. Moshnikova, J. Daniels, D. M. Engelman, O. A. Andreev, and Y. K. Reshetnyak, "Family of pH (low) insertion peptides for tumor targeting," *Proc. Natl. Acad. Sci. U.S.A.,* vol. 110, no. 15, pp. 5834-9, 2013.

[41]    C. von Forstner, M. Zuhayra, O. Ammerpohl, Y. Zhao, S. Tiwari, O. Jansen, H. Kalthoff, E. Henze, and J. H. Egberts, "Expression of L amino acid transport system 1 and analysis of iodine-123-methyltyrosine tumor uptake in a pancreatic xenotransplantation model using fused high-resolution-micro-SPECT-MRI," *Hepatobiliary Pancreat. Dis. Int.,* vol. 10, no. 1, pp. 30-7, 2011.

[42]    N. Kondo, T. Temma, Y. Shimizu, H. Watanabe, K. Higano, Y. Takagi, M. Ono, and H. Saji, "Miniaturized antibodies for imaging membrane type-1 matrix metalloproteinase in cancers," *Cancer Sci.,* vol. 104, no. 4, pp. 495-501, 2013.

[43]    A. M. LeBeau, S. Duriseti, S. T. Murphy, F. Pepin, B. Hann, J. W. Gray, H. F. VanBrocklin, and C. S. Craik, "Targeting uPAR with antagonistic recombinant human antibodies in aggressive breast cancer," *Cancer Res.,* vol. 73, no. 7, pp. 2070-81, 2013.

[44]    M. Schottelius, and H. J. Wester, "Molecular imaging targeting peptide receptors," *Methods,* vol. 48, no. 2, pp. 161-77, 2009.

[45]    S. Heskamp, H. W. van Laarhoven, J. D. Molkenboer-Kuenen, W. H. Bouwman, W. T. van der Graaf, W. J. Oyen, and O. C. Boerman, "Optimization of IGF-1R SPECT/CT Imaging Using (111)In-Labeled F(ab')(2) and Fab Fragments of the Monoclonal Antibody R1507," *Mol. Pharm.*, 2012.

[46]    G. Mariani, S. Di Sacco, D. Volterrani, L. Di Luca, S. Buralli, R. Di Stefano, J. Baranowska-Kortylewicz, D. Bonora, F. Matteucci, S. Ricci, C. R. Bellina, A. Falcone, P. A. Salvadori, F. Mosca, S. Adelstein, and A. I. Kassis, "Tumor targeting by intra-arterial infusion of 5-[123I]iodo-2'-deoxyuridine in patients with liver metastases from colorectal cancer.," *J. Nucl. Med.,* vol. 37, pp. 22s-25s, 1996.

[47]    L. Aloj, M. Aurilio, V. Rinaldi, L. D'Ambrosio, D. Tesauro, P. K. Peitl, T. Maina, R. Mansi, E. von Guggenberg, L. Joosten, J. K. Sosabowski, W. A. Breeman, E. De Blois, S. Koelewijn, M. Melis, B. Waser, K. Beetschen, J. C. Reubi, and M. de Jong, "Comparison of the binding and

internalization properties of 12 DOTA-coupled and (1)(1)(1)In-labelled CCK2/gastrin receptor binding peptides: a collaborative project under COST Action BM0607," *Eur. J. Nucl. Med. Mol. Imaging,* vol. 38, no. 8, pp. 1417-25, 2011.

[48]  F. Forrer, R. Valkema, B. Bernard, N. U. Schramm, J. W. Hoppin, E. Rolleman, E. P. Krenning, and M. de Jong, "In vivo radionuclide uptake quantification using a multi-pinhole SPECT system to predict renal function in small animals," *Eur. J. Nucl. Med. Mol. Imaging,* vol. 33, no. 10, pp. 1214-7, 2006.

[49]  K. Abiraj, R. Mansi, M. L. Tamma, M. Fani, F. Forrer, G. Nicolas, R. Cescato, J. C. Reubi, and H. R. Maecke, "Bombesin antagonist-based radioligands for translational nuclear imaging of gastrin-releasing peptide receptor-positive tumors," *J. Nucl. Med.,* vol. 52, no. 12, pp. 1970-8, 2011.

[50]  M. Fani, F. Braun, B. Waser, K. Beetschen, R. Cescato, J. Erchegyi, J. E. Rivier, W. A. Weber, H. R. Maecke, and J. C. Reubi, "Unexpected sensitivity of sst2 antagonists to N-terminal radiometal modifications," *J. Nucl. Med.,* vol. 53, no. 9, pp. 1481-9, 2012.

[51]  A. B. Hwang, and B. H. Hasegawa, "Attenuation correction for small animal SPECT imaging using x-ray CT data," *Med. Phys.,* vol. 32, no. 9, pp. 2799-804, 2005.

[52]  L. Joosten, P. Laverman, O. C. Boerman, S. Roosenburg, A. Eek, F. P. Rutjes, and F. L. van Delft, "In vitro and in vivo characterization of three 68Ga- and 111In-labeled peptides for cholecystokinin receptor imaging.," *Mol. Imaging,* vol. 11, pp. 401-7, 2012.

[53]  C. Muller, I. R. Vlahov, H. K. Santhapuram, C. P. Leamon, and R. Schibli, "Tumor targeting using 67Ga-DOTA-Bz-folate--investigations of methods to improve the tissue distribution of radiofolates," *Nucl. Med. Biol.,* vol. 38, no. 5, pp. 715-23, 2011.

[54]  T. K. Nayak, H. J. Hathaway, C. Ramesh, J. B. Arterburn, D. Dai, L. A. Sklar, J. P. Norenberg, and E. R. Prossnitz, "Preclinical development of a neutral, estrogen receptor-targeted, tridentate 99mTc(I)-estradiol-pyridin-2-yl hydrazine derivative for imaging of breast and endometrial cancers," *J. Nucl. Med.,* vol. 49, no. 6, pp. 978-86, 2008.

[55]  M. van Essen, E. P. Krenning, B. L. Kam, M. de Jong, R. Valkema, and D. J. Kwekkeboom, "Peptide-receptor radionuclide therapy for endocrine tumors," *Nat. Rev. Endocrinol.,* vol. 5, no. 7, pp. 382-93, 2009.

[56]  S. P. Williams, "Tissue distribution studies of protein therapeutics using molecular probes: molecular imaging," *AAPS J.,* vol. 14, no. 3, pp. 389-99, 2012.

[57]  R. P. Brinkhuis, K. Stojanov, P. Laverman, J. Eilander, I. S. Zuhorn, F. P. Rutjes, and J. C. van Hest, "Size Dependent Biodistribution and SPECT Imaging of (111)In-Labeled Polymersomes," *Bioconjug. Chem.*, 2012.

[58]  Y. J. Chang, C. H. Chang, C. Y. Yu, T. J. Chang, L. C. Chen, M. H. Chen, T. W. Lee, and G. Ting, "Therapeutic efficacy and microSPECT/CT imaging of 188Re-DXR-liposome in a C26 murine colon carcinoma solid tumor model," *Nucl. Med. Biol.,* vol. 37, no. 1, pp. 95-104, 2010.

[59]  M. de Smet, S. Langereis, S. van den Bosch, K. Bitter, N. M. Hijnen, E. Heijman, and H. Grull, "SPECT/CT imaging of temperature-sensitive liposomes for MR-image guided drug delivery with high intensity focused ultrasound," *J. Control Release,* vol. 169, no. 1-2, pp. 82-90, 2013.

[60]  F. Y. Huang, T. W. Lee, C. H. Kao, C. H. Chang, X. Zhang, W. Y. Lee, W. J. Chen, S. C. Wang, and J. M. Lo, "Imaging, autoradiography, and biodistribution of (188)Re-labeled PEGylated nanoliposome in orthotopic glioma bearing rat model," *Cancer Biother. Radiopharm.,* vol. 26, no. 6, pp. 717-25, 2011.

[61]  C. C. Tsai, C. H. Chang, L. C. Chen, Y. J. Chang, K. L. Lan, Y. H. Wu, C. W. Hsu, I. H. Liu, C. L. Ho, W. C. Lee, H. C. Ni, T. J. Chang, G. Ting, and T. W. Lee, "Biodistribution and pharmacokinetics of 188Re-liposomes and their comparative therapeutic efficacy with 5-fluorouracil in C26 colonic peritoneal carcinomatosis mice," *Int. J. Nanomedicine,* vol. 6, pp. 2607-19, 2011.

[62]  W. Bult, S. G. Kroeze, M. Elschot, P. R. Seevinck, F. J. Beekman, H. W. de Jong, D. R. Uges, J. G. Kosterink, P. R. Luijten, W. E. Hennink, A. D. van het Schip, J. L. Bosch, J. F. Nijsen, and J. J. Jans, "Intratumoral administration of Holmium-166 acetylacetonate microspheres: Antitumor efficacy and feasibility of multimodality imaging in renal cancer," *PLoS ONE,* vol. 8, no. 1, pp. e52178, 2013.

[63] R. Madru, P. Kjellman, F. Olsson, K. Wingårdh, C. Ingvar, F. Ståhlberg, J. Olsrud, J. Lätt, S. Fredriksson, L. Knutsson, and S. E. Strand, "99mTc-labeled superparamagnetic iron oxide nanoparticles for multimodality SPECT/MRI of sentinel lymph nodes.," *J. Nucl. Med.,* vol. 53, pp. 459-63, 2012.

[64] M. M. Ali, B. Janic, A. Babajani-Feremi, N. R. Varma, A. S. Iskander, J. Anagli, and A. S. Arbab, "Changes in vascular permeability and expression of different angiogenic factors following anti-angiogenic treatment in rat glioma," *PLoS ONE,* vol. 5, no. 1, pp. e8727, 2010.

[65] M. De Saint-Hubert, H. Wang, E. Devos, K. Vunckx, L. Zhou, C. Reutelingsperger, A. Verbruggen, L. Mortelmans, Y. Ni, and F. M. Mottaghy, "Preclinical imaging of therapy response using metabolic and apoptosis molecular imaging," *Mol. Imaging Biol.,* vol. 13, no. 5, pp. 995-1002, 2011.

[66] C. Vangestel, C. Van de Wiele, G. Mees, K. Mertens, S. Staelens, C. Reutelingsperger, P. Pauwels, N. Van Damme, and M. Peeters, "Single-photon emission computed tomographic imaging of the early time course of therapy-induced cell death using technetium 99m tricarbonyl His-annexin A5 in a colorectal cancer xenograft model," *Mol. Imaging,* vol. 11, no. 2, pp. 135-47, 2012.

[67] K. Bol, J. C. Haeck, H. Groen, M. Bernsen, J. F. Veenland, and M. de Jong, "Correlation of SPECT and DCE-MRI in a neuroendocrine tumour model," *Eur. J. Nucl. Med. Mol. Imaging,* vol. 39, pp. s194-s194, 2012.

[68] R. Bar-Shalom, N. Yefremov, L. Guralnik, Z. Keidar, A. Engel, S. Nitecki, and O. Israel, "SPECT/CT using 67Ga and 111In-labeled leukocyte scintigraphy for diagnosis of infection," *J. Nucl. Med.,* vol. 47, no. 4, pp. 587-94, 2006.

[69] H. Hong, Y. Yang, Y. Zhang, and W. Cai, "Non-invasive cell tracking in cancer and cancer therapy," *Curr. Top. Med. Chem.,* vol. 10, no. 12, pp. 1237-48, 2010.

[70] A. Ruggiero, D. L. Thorek, J. Guenoun, G. P. Krestin, and M. R. Bernsen, "Cell tracking in cardiac repair: what to image and how to image," *Eur. Radiol.,* vol. 22, no. 1, pp. 189-204, 2012.

[71] M. M. Welling, M. Duijvestein, A. Signore, and L. van der Weerd, "In vivo biodistribution of stem cells using molecular nuclear medicine imaging," *J. Cell. Physiol.,* vol. 226, no. 6, pp. 1444-52, 2011.

[72] M. R. Bernsen, A. D. Moelker, P. A. Wielopolski, S. T. van Tiel, and G. P. Krestin, "Labelling of mammalian cells for visualisation by MRI," *Eur. Radiol.,* vol. 20, no. 2, pp. 255-74, 2010.

[73] E. F. de Vries, A. R. Buursma, G. A. Hospers, N. H. Mulder, and W. Vaalburg, "Scintigraphic imaging of HSVtk gene therapy," *Curr. Pharm. Des.,* vol. 8, no. 16, pp. 1435-50, 2002.

[74] A. R. Penheiter, S. J. Russell, and S. K. Carlson, "The sodium iodide symporter (NIS) as an imaging reporter for gene, viral, and cell-based therapies," *Curr. Gene Ther.,* vol. 12, no. 1, pp. 33-47, 2012.

[75] M. M. Doubrovin, E. S. Doubrovina, P. Zanzonico, M. Sadelain, S. M. Larson, and R. J. O'Reilly, "In vivo imaging and quantitation of adoptively transferred human antigen-specific T cells transduced to express a human norepinephrine transporter gene," *Cancer Res.,* vol. 67, no. 24, pp. 11959-69, 2007.

[76] C. Templin, R. Zweigerdt, K. Schwanke, R. Olmer, J. R. Ghadri, M. Y. Emmert, E. Muller, S. M. Kuest, S. Cohrs, R. Schibli, P. Kronen, M. Hilbe, A. Reinisch, D. Strunk, A. Haverich, S. Hoerstrup, T. F. Luscher, P. A. Kaufmann, U. Landmesser, and U. Martin, "Transplantation and tracking of human-induced pluripotent stem cells in a pig model of myocardial infarction: assessment of cell survival, engraftment, and distribution by hybrid single photon emission computed tomography/computed tomography of sodium iodide symporter transgene expression," *Circulation,* vol. 126, no. 4, pp. 430-9, 2012.

[77] W. P. Deng, C. C. Wu, C. C. Lee, W. K. Yang, H. E. Wang, R. S. Liu, H. J. Wei, J. G. Gelovani, J. J. Hwang, D. M. Yang, Y. K. Fu, and C. W. Wu, "Serial in vivo imaging of the lung metastases model and gene therapy using HSV1-tk and ganciclovir," *J. Nucl. Med.,* vol. 47, no. 5, pp. 877-84, 2006.

[78] M. Inubushi, Y. N. Jin, C. Murai, H. Hata, Y. Kitagawa, and T. Saga, "Single-photon emission computed tomography of spontaneous liver metastasis from orthotopically implanted human

colon cancer cell line stably expressing human sodium/iodide symporter reporter gene," *EJNMMI Res.,* vol. 2, no. 1, pp. 46, 2012.

[79]  D. K. Marsee, D. H. Shen, L. R. MacDonald, D. D. Vadysirisack, X. Lin, G. Hinkle, R. T. Kloos, and S. M. Jhiang, "Imaging of metastatic pulmonary tumors following NIS gene transfer using single photon emission computed tomography," *Cancer Gene Ther.,* vol. 11, no. 2, pp. 121-7, 2004.

[80]  A. Merron, P. Baril, P. Martin-Duque, A. de la Vieja, L. Tran, A. Briat, K. J. Harrington, I. A. McNeish, and G. Vassaux, "Assessment of the Na/I symporter as a reporter gene to visualize oncolytic adenovirus propagation in peritoneal tumours," *Eur. J. Nucl. Med. Mol. Imaging,* vol. 37, no. 7, pp. 1377-85, 2010.

[81]  M. A. Moroz, I. Serganova, P. Zanzonico, L. Ageyeva, T. Beresten, E. Dyomina, E. Burnazi, R. D. Finn, M. Doubrovin, and R. G. Blasberg, "Imaging hNET reporter gene expression with 124I-MIBG," *J. Nucl. Med.,* vol. 48, no. 5, pp. 827-36, 2007.

[82]  V. Ambrosini, M. Fani, S. Fanti, F. Forrer, and H. R. Maecke, "Radiopeptide imaging and therapy in Europe," *J. Nucl. Med.,* vol. 52 Suppl 2, pp. 42S-55S, 2011.

[83]  J. C. Reubi, "The role of peptides and their receptors as tumor markers," *Endocrinol. Metab. Clin. North Am.,* vol. 22, no. 4, pp. 917-39, 1993.

[84]  N. Devoogdt, C. Xavier, S. Hernot, I. Vaneycken, M. D'Huyvetter, J. De Vos, S. Massa, P. De Baetselier, V. Caveliers, and T. Lahoutte, "Molecular imaging using Nanobodies: a case study," *Methods Mol. Biol.,* vol. 911, pp. 559-67, 2012.

[85]  D. M. Goldenberg, E. A. Rossi, R. M. Sharkey, W. J. McBride, and C. H. Chang, "Multifunctional antibodies by the Dock-and-Lock method for improved cancer imaging and therapy by pretargeting," *J. Nucl. Med.,* vol. 49, no. 1, pp. 158-63, 2008.

[86]  J. Lofblom, J. Feldwisch, V. Tolmachev, J. Carlsson, S. Stahl, and F. Y. Frejd, "Affibody molecules: engineered proteins for therapeutic, diagnostic and biotechnological applications," *FEBS Lett.,* vol. 584, no. 12, pp. 2670-80, 2010.

[87]  T. Olafsen, and A. M. Wu, "Antibody vectors for imaging," *Semin. Nucl. Med.,* vol. 40, no. 3, pp. 167-81, 2010.

[88]  J. V. Jokerst, and S. S. Gambhir, "Molecular imaging with theranostic nanoparticles," *Acc. Chem. Res.,* vol. 44, no. 10, pp. 1050-60, 2011.

[89]  M. de Jong, W. A. Breeman, D. J. Kwekkeboom, R. Valkema, and E. P. Krenning, "Tumor imaging and therapy using radiolabeled somatostatin analogues," *Acc. Chem. Res.,* vol. 42, no. 7, pp. 873-80, 2009.

[90]  J. Booij, G. Tissingh, G. J. Boer, J. D. Speelman, J. C. Stoof, A. G. Janssen, E. C. Wolters, and E. A. van Royen, "[123I]FP-CIT SPECT shows a pronounced decline of striatal dopamine transporter labelling in early and advanced Parkinson's disease," *J. Neurol. Neurosurg. Psychiatry,* vol. 62, no. 2, pp. 133-40, 1997.

[91]  J. Booij, G. Tissingh, A. Winogrodzka, and E. A. van Royen, "Imaging of the dopaminergic neurotransmission system using single-photon emission tomography and positron emission tomography in patients with parkinsonism," *Eur. J. Nucl. Med.,* vol. 26, no. 2, pp. 171-82, 1999.

[92]  A. M. Catafau, and E. Tolosa, "Impact of dopamine transporter SPECT using 123I-Ioflupane on diagnosis and management of patients with clinically uncertain Parkinsonian syndromes," *Mov. Disord.,* vol. 19, no. 10, pp. 1175-82, 2004.

[93]  S. J. Kish, K. Shannak, and O. Hornykiewicz, "Uneven pattern of dopamine loss in the striatum of patients with idiopathic Parkinson's disease: Pathophysiologic and clinical implications," *N. Engl. J. Med.,* vol. 318, no. 14, pp. 876-80, 1988.

[94]  M. M. Ponsen, D. Stoffers, J. Booij, B. L. van Eck-Smit, E. Wolters, and H. W. Berendse, "Idiopathic hyposmia as a preclinical sign of Parkinson's disease," *Ann. Neurol.,* vol. 56, no. 2, pp. 173-81, 2004.

[95]  M. Ziebell, B. B. Andersen, G. Thomsen, L. H. Pinborg, M. Karlsborg, S. G. Hasselbalch, and G. M. Knudsen, "Predictive value of dopamine transporter SPECT imaging with [(1)(2)(3)I]PE2I in patients with subtle parkinsonian symptoms," *Eur. J. Nucl. Med. Mol. Imaging,* vol. 39, no. 2, pp. 242-50, 2012.

[96]     P. D. Acton, C. Hou, M. P. Kung, K. Plossl, C. L. Keeney, and H. F. Kung, "Occupancy of dopamine D2 receptors in the mouse brain measured using ultra-high-resolution single-photon emission tomography and [123]IBF," *Eur. J. Nucl. Med. Mol. Imaging,* vol. 29, no. 11, pp. 1507-15, 2002.

[97]     J. B. Habraken, K. de Bruin, M. Shehata, J. Booij, R. Bennink, B. L. van Eck Smit, and E. Busemann Sokole, "Evaluation of high-resolution pinhole SPECT using a small rotating animal," *J. Nucl. Med.,* vol. 42, no. 12, pp. 1863-9, 2001.

[98]     J. Booij, K. de Bruin, J. B. Habraken, and P. Voorn, "Imaging of dopamine transporters in rats using high-resolution pinhole single-photon emission tomography," *Eur. J. Nucl. Med. Mol. Imaging,* vol. 29, no. 9, pp. 1221-4, 2002.

[99]     C. Scherfler, E. Donnemiller, M. Schocke, K. Dierkes, C. Decristoforo, M. Oberladstatter, C. Kolbitsch, F. Zschiegner, G. Riccabona, W. Poewe, and G. Wenning, "Evaluation of striatal dopamine transporter function in rats by in vivo beta-[123I]CIT pinhole SPECT," *Neuroimage,* vol. 17, no. 1, pp. 128-41, 2002.

[100]   M. Laruelle, R. M. Baldwin, R. T. Malison, Y. Zea-Ponce, S. S. Zoghbi, M. S. al-Tikriti, E. H. Sybirska, R. C. Zimmermann, G. Wisniewski, J. L. Neumeyer, R. A. Milius, S. Wang, E. O. Smith, R. H. Roth, D. S. Charney, P. B. Hoffer, and R. B. Innis, "SPECT imaging of dopamine and serotonin transporters with [123I]beta-CIT: Pharmacological characterization of brain uptake in nonhuman primates," *Synapse,* vol. 13, no. 4, pp. 295-309, 1993.

[101]   G. Andringa, B. Drukarch, J. G. Bol, K. de Bruin, K. Sorman, J. B. Habraken, and J. Booij, "Pinhole SPECT imaging of dopamine transporters correlates with dopamine transporter immunohistochemical analysis in the MPTP mouse model of Parkinson's disease," *Neuroimage,* vol. 26, no. 4, pp. 1150-8, 2005.

[102]   J. Booij, K. de Bruin, M. M. de Win, C. Lavini, G. J. den Heeten, and J. B. Habraken, "Imaging of striatal dopamine transporters in rat brain with single pinhole SPECT and co-aligned MRI is highly reproducible," *Nucl. Med. Biol.,* vol. 30, no. 6, pp. 643-9, 2003.

[103]   J. A. Gleave, T. H. Farncombe, C. Saab, and L. C. Doering, "Correlative single photon emission computed tomography imaging of [123I]altropane binding in the rat model of Parkinson's," *Nucl. Med. Biol.,* vol. 38, no. 5, pp. 741-9, 2011.

[104]   D. Alvarez-Fischer, G. Blessmann, C. Trosowski, M. Behe, T. Schurrat, A. Hartmann, T. M. Behr, W. H. Oertel, G. U. Hoglinger, and H. Hoffken, "Quantitative [(123)I]FP-CIT pinhole SPECT imaging predicts striatal dopamine levels, but not number of nigral neurons in different mouse models of Parkinson's disease," *Neuroimage,* vol. 38, no. 1, pp. 5-12, 2007.

[105]   C. Depboylu, L. Maurer, A. Matusch, G. Hermanns, A. Windolph, M. Behe, W. H. Oertel, and G. U. Hoglinger, "Effect of long-term treatment with pramipexole or levodopa on presynaptic markers assessed by longitudinal [123I]FP-CIT SPECT and histochemistry," *Neuroimage,* vol. 79, pp. 191-200, 2013.

[106]   J. D. Lee, Y. H. Chu, C. W. Chen, and K. J. Lin, "Multi-image registration for evaluating the 99mTc-TRODAT-1 of Parkinson's rat model," *Conf. Proc. IEEE Eng. Med. Biol. Soc.,* vol. 2009, pp. 5801-4, 2009.

[107]   P. D. Acton, S. R. Choi, K. Plossl, and H. F. Kung, "Quantification of dopamine transporters in the mouse brain using ultra-high resolution single-photon emission tomography," *Eur. J. Nucl. Med. Mol. Imaging,* vol. 29, no. 5, pp. 691-8, 2002.

[108]   S. Nikolaus, R. Larisch, A. Wirrwar, M. Jamdjeu-Noune, C. Antke, M. Beu, N. Schramm, and H. W. Muller, "[123I]Iodobenzamide binding to the rat dopamine D2 receptor in competition with haloperidol and endogenous dopamine--an in vivo imaging study with a dedicated small animal SPECT," *Eur. J. Nucl. Med. Mol. Imaging,* vol. 32, no. 11, pp. 1305-10, 2005.

[109]   C. Scherfler, S. W. Scholz, E. Donnemiller, C. Decristoforo, M. Oberladstatter, N. Stefanova, E. Diederen, I. Virgolini, W. Poewe, and G. K. Wenning, "Evaluation of [123I]IBZM pinhole SPECT for the detection of striatal dopamine D2 receptor availability in rats," *Neuroimage,* vol. 24, no. 3, pp. 822-31, 2005.

[110]   R. S. Fisher, M. S. Levine, D. R. Sibley, and M. A. Ariano, "D2 dopamine receptor protein location: Golgi impregnation-gold toned and ultrastructural analysis of the rat neostriatum," *J. Neurosci. Res.,* vol. 38, no. 5, pp. 551-64, 1994.

[111]  K. Herholz, and K. Ebmeier, "Clinical amyloid imaging in Alzheimer's disease," *Lancet Neurol.,* vol. 10, no. 7, pp. 667-70, 2011.

[112]  M. M. Svedberg, O. Rahman, and H. Hall, "Preclinical studies of potential amyloid binding PET/SPECT ligands in Alzheimer's disease," *Nucl. Med. Biol.,* vol. 39, no. 4, pp. 484-501, 2012.

[113]  E. Teng, V. Kepe, S. A. Frautschy, J. Liu, N. Satyamurthy, F. Yang, P. P. Chen, G. B. Cole, M. R. Jones, S. C. Huang, D. G. Flood, S. P. Trusko, G. W. Small, G. M. Cole, and J. R. Barrio, "[F-18]FDDNP microPET imaging correlates with brain Abeta burden in a transgenic rat model of Alzheimer disease: effects of aging, in vivo blockade, and anti-Abeta antibody treatment," *Neurobiol. Dis.,* vol. 43, no. 3, pp. 565-75, 2011.

[114]  M. P. Kung, C. Hou, Z. P. Zhuang, A. J. Cross, D. L. Maier, and H. F. Kung, "Characterization of IMPY as a potential imaging agent for beta-amyloid plaques in double transgenic PSAPP mice," *Eur. J. Nucl. Med. Mol. Imaging,* vol. 31, no. 8, pp. 1136-45, 2004.

[115]  M. P. Kung, C. Hou, Z. P. Zhuang, B. Zhang, D. Skovronsky, J. Q. Trojanowski, V. M. Lee, and H. F. Kung, "IMPY: An improved thioflavin-T derivative for in vivo labeling of beta-amyloid plaques," *Brain Res.,* vol. 956, no. 2, pp. 202-10, 2002.

[116]  M. A. Nader, D. Morgan, H. D. Gage, S. H. Nader, T. L. Calhoun, N. Buchheimer, R. Ehrenkaufer, and R. H. Mach, "PET imaging of dopamine D2 receptors during chronic cocaine self-administration in monkeys," *Nat. Neurosci.,* vol. 9, no. 8, pp. 1050-6, 2006.

[117]  C. L. Crunelle, T. C. de Wit, K. de Bruin, R. M. Ramakers, F. van der Have, F. J. Beekman, W. van den Brink, and J. Booij, "Varenicline increases in vivo striatal dopamine D2/3 receptor binding: An ultra-high-resolution pinhole [123I]IBZM SPECT study in rats," *Nucl. Med. Biol.,* vol. 39, no. 5, pp. 640-4, 2012.

[118]  C. L. Crunelle, M. L. Miller, K. de Bruin, W. van den Brink, and J. Booij, "Varenicline increases striatal dopamine D(2/3) receptor binding in rats," *Addict. Biol.,* vol. 14, no. 4, pp. 500-2, 2009.

[119]  C. L. Crunelle, E. van de Giessen, S. Schulz, L. J. M. J. Vanderschuren, K. de Bruin, W. van den Brink, and J. Booij, "Cannabinoid-1 receptor antagonist rimonabant (SR141716) increases striatal dopamine D2 receptor availability," *Addict. Biol.,* vol. 18, no. 6, pp. 908-911, 2013.

[120]  B. Vastenhouw, F. van der Have, A. J. van der Linden, L. von Oerthel, J. Booij, J. P. Burbach, M. P. Smidt, and F. J. Beekman, "Movies of dopamine transporter occupancy with ultra-high resolution focusing pinhole SPECT," *Mol. Psychiatry,* vol. 12, no. 11, pp. 984-7, 2007.

[121]  Y. R. Huang, J. M. Shih, K. W. Chang, C. Huang, Y. L. Wu, and C. C. Chen, "[123I]Epidepride neuroimaging of dopamine D2/D3 receptor in chronic MK-801-induced rat schizophrenia model," *Nucl. Med. Biol.,* vol. 39, no. 6, pp. 826-32, 2012.

[122]  M. Laruelle, A. Abi-Dargham, C. H. van Dyck, W. Rosenblatt, Y. Zea-Ponce, S. S. Zoghbi, R. M. Baldwin, D. S. Charney, P. B. Hoffer, H. F. Kung, and R. B. Innis, "SPECT imaging of striatal dopamine release after amphetamine challenge," *J. Nucl. Med.,* vol. 36, no. 7, pp. 1182-90, 1995.

[123]  M. Laruelle, A. Abi-Dargham, C. H. van Dyck, R. Gil, C. D. D'Souza, J. Erdos, E. McCance, W. Rosenblatt, C. Fingado, S. S. Zoghbi, R. M. Baldwin, J. P. Seibyl, J. H. Krystal, D. S. Charney, and R. B. Innis, "Single photon emission computerized tomography imaging of amphetamine-induced dopamine release in drug-free schizophrenic subjects," *Proc. Natl. Acad. Sci. U.S.A.,* vol. 93, no. 17, pp. 9235-40, 1996.

[124]  D. Martinez, R. Narendran, R. W. Foltin, M. Slifstein, D. R. Hwang, A. Broft, Y. Huang, T. B. Cooper, M. W. Fischman, H. D. Kleber, and M. Laruelle, "Amphetamine-induced dopamine release: markedly blunted in cocaine dependence and predictive of the choice to self-administer cocaine," *Am. J. Psychiatry,* vol. 164, no. 4, pp. 622-9, 2007.

[125]  C. Jongen, K. de Bruin, F. Beekman, and J. Booij, "SPECT imaging of D2 dopamine receptors and endogenous dopamine release in mice," *Eur. J. Nucl. Med. Mol. Imaging,* vol. 35, no. 9, pp. 1692-8, 2008.

[126]  S. Nikolaus, C. Antke, M. Beu, K. Kley, A. Wirrwar, J. P. Huston, and H. W. Muller, "Binding of [123I]iodobenzamide to the rat D2 receptor after challenge with various doses of methylphenidate: an in vivo imaging study with dedicated small animal SPECT," *Eur. J. Nucl. Med. Mol. Imaging,* vol. 38, no. 4, pp. 694-701, 2011.

[127]    I. Apostolova, A. Wunder, U. Dirnagl, R. Michel, N. Stemmer, M. Lukas, T. Derlin, B. Gregor-Mamoudou, J. Goldschmidt, W. Brenner, and R. Buchert, "Brain perfusion SPECT in the mouse: Normal pattern according to gender and age," *Neuroimage,* vol. 63, no. 4, pp. 1807-17, 2012.

[128]    T. Zeniya, H. Watabe, T. Hayashi, T. Ose, K. Myojin, A. Taguchi, A. Yamamoto, N. Teramoto, M. Kanagawa, Y. Yamamichi, and H. Iida, "Three-dimensional quantitation of regional cerebral blood flow in mice using a high-resolution pinhole SPECT system and 123I-iodoamphetamine," *Nucl. Med. Biol.,* vol. 38, no. 8, pp. 1157-64, 2011.

[129]    A. G. Ceulemans, S. Hernot, T. Zgavc, V. Caveliers, S. Hachimi-Idrissi, S. Sarre, T. Lahoutte, and Y. Michotte, "Serial semiquantitative imaging of brain damage using micro-SPECT and micro-CT after endothelin-1-induced transient focal cerebral ischemia in rats," *J. Nucl. Med.,* vol. 52, no. 12, pp. 1987-92, 2011.

[130]    M. Figee, P. de Koning, S. Klaassen, N. Vulink, M. Mantione, P. van den Munckhof, R. Schuurman, G. van Wingen, T. van Amelsvoort, J. Booij, and D. Denys, "Deep Brain Stimulation Induces Striatal Dopamine Release in Obsessive-Compulsive Disorder," *Biol. Psychiatry*, 2013.

[131]    T. Wyckhuys, S. Staelens, B. Van Nieuwenhuyse, S. Deleye, H. Hallez, K. Vonck, R. Raedt, W. Wadman, and P. Boon, "Hippocampal deep brain stimulation induces decreased rCBF in the hippocampal formation of the rat," *Neuroimage,* vol. 52, no. 1, pp. 55-61, 2010.

[132]    G. Paxinos, and C. Watson, *The Rat Brain in Stereotaxic Coordinates*, San Diego: Academic Press, 1997.

[133]    F. Y. Yang, H. E. Wang, G. L. Lin, M. C. Teng, H. H. Lin, T. T. Wong, and R. S. Liu, "Micro-SPECT/CT-based pharmacokinetic analysis of 99mTc-diethylenetriaminepentaacetic acid in rats with blood-brain barrier disruption induced by focused ultrasound," *J. Nucl. Med.,* vol. 52, no. 3, pp. 478-84, 2011.

[134]    L. Han, Y. Ren, L. Long, Y. Zhong, C. Shen, P. Pu, X. Yuan, and C. Kang, "Inhibition of C6 glioma in vivo by combination chemotherapy of implantation of polymer wafer and intracarotid perfusion of transferrin-decorated nanoparticles," *Oncol. Rep.,* vol. 27, no. 1, pp. 121-8, 2012.

[135]    S. Nimmagadda, M. Pullambhatla, and M. G. Pomper, "Immunoimaging of CXCR4 expression in brain tumor xenografts using SPECT/CT," *J. Nucl. Med.,* vol. 50, no. 7, pp. 1124-30, 2009.

[136]    P. L. Chow, D. B. Stout, E. Komisopoulou, and A. F. Chatziioannou, "A method of image registration for small animal, multi-modality imaging," *Phys. Med. Biol.,* vol. 51, no. 2, pp. 379-90, 2006.

[137]    C. Ji, F. van der Have, H. Gratama van Andel, R. Ramakers, and F. Beekman, "Accurate Coregistration between Ultra-High-Resolution Micro-SPECT and Circular Cone-Beam Micro-CT Scanners," *Int. J. Biomed. Imaging,* vol. 2010, pp. 654506, 2010.

[138]    L. R. Furenlid, D. W. Wilson, Y. C. Chen, H. Kim, P. J. Pietraski, M. J. Crawford, and H. H. Barrett, "FastSPECT II: A Second-Generation High-Resolution Dynamic SPECT Imager," *IEEE Trans. Nucl. Sci.,* vol. 51, no. 3, pp. 631-635, 2004.

[139]    G. K. Kastis, H. B. Barber, H. H. Barrett, H. C. Gifford, I. W. Pang, D. D. Patton, J. D. Sain, G. Stevenson, and D. W. Wilson, "High resolution SPECT imager for three-dimensional imaging of small animals," *J. Nucl. Med.,* vol. 39, no. 5, pp. 9P-9P, 1998.

[140]    F. Van der Have, B. Vastenhouw, R. M. Ramakers, W. Branderhorst, J. O. Krah, C. Ji, S. G. Staelens, and F. J. Beekman, "U-SPECT-II: An Ultra-High-Resolution Device for Molecular Small-Animal Imaging," *J. Nucl. Med.,* vol. 50, no. 4, pp. 599-605, 2009.

[141]    W. Branderhorst, B. Vastenhouw, F. van der Have, E. L. Blezer, W. K. Bleeker, and F. J. Beekman, "Targeted multi-pinhole SPECT," *Eur. J. Nucl. Med. Mol. Imaging,* vol. 38, no. 3, pp. 552-61, 2011.

[142]    G. Shao, Y. Zhou, F. Wang, and S. Liu, "Monitoring glioma growth and tumor necrosis with the U-SPECT-II/CT scanner by targeting integrin alphavbeta3," *Mol. Imaging,* vol. 12, no. 1, pp. 39-48, 2013.

[143]   A. Bitar, A. Lisbona, P. Thedrez, C. Sai Maurel, D. Le Forestier, J. Barbet, and M. Bardies, "A voxel-based mouse for internal dose calculations using Monte Carlo simulations (MCNP)," *Phys. Med. Biol.,* vol. 52, no. 4, pp. 1013-25, 2007.

[144]   V. Kersemans, J. Thompson, B. Cornelissen, M. Woodcock, P. D. Allen, N. Buls, R. J. Muschel, M. A. Hill, and S. C. Smart, "Micro-CT for anatomic referencing in PET and SPECT: radiation dose, biologic damage, and image quality," *J. Nucl. Med.,* vol. 52, no. 11, pp. 1827-33, 2011.

[145]   M. Stabin, "Nuclear medicine dosimetry," *Phys. Med. Biol.,* vol. 51, no. 13, pp. R187-202, 2006.

[146]   I. Willekens, N. Buls, T. Lahoutte, L. Baeyens, C. Vanhove, V. Caveliers, R. Deklerck, A. Bossuyt, and J. de Mey, "Evaluation of the radiation dose in micro-CT with optimization of the scan protocol," *Contrast Media Mol. Imaging,* vol. 5, no. 4, pp. 201-7, 2010.

[147]   T. Xie, and H. Zaidi, "Age-dependent small-animal internal radiation dosimetry," *Mol. Imaging,* vol. 12, no. 6, pp. 364-75, 2013.

[148]   E. Breton, P. Choquet, C. Goetz, J. Kintz, P. Erbs, R. Rooke, and A. Constantinesco, "Dual SPECT MR imaging in small animal.," *Nucl. Instr. Meth. Phys. Res. A,* vol. 571, pp. 446-448, 2007.

[149]   D. Meier, D. J. Wagenaar, S. Chen, J. Xu, J. Yu, and B. M. Tsui, "A SPECT Camera for Combined MRI and SPECT for Small Animals," *Nucl. Instr. Meth. Phys. Res. A,* vol. 652, no. 1, pp. 731-734, 2011.

[150]   J.-W. Tan, L. Cai, and L.-J. Meng, "A prototype of the MRI-compatible ultra-high resolution SPECT for in vivo mice brain imaging," *2009 IEEE Nuclear Science Symposium Conference Record*, IEEE Nuclear Science Symposium Conference Record B. Yu, ed., pp. 2800-2805, New York: IEEE, 2009.

[151]   D. Beque, J. Nuyts, G. Bormans, P. Suetens, and P. Dupont, "Characterization of pinhole SPECT acquisition geometry," *IEEE Trans. Med. Imag.,* vol. 22, no. 5, pp. 599-612, 2003.

[152]   D. Beque, J. Nuyts, P. Suetens, and G. Bormans, "Optimization of geometrical calibration in pinhole SPECT," *IEEE Trans. Med. Imag.,* vol. 24, no. 2, pp. 180-90, 2005.

[153]   M. Defrise, C. Vanhove, and J. Nuyts, "Perturbative refinement of the geometric calibration in pinhole SPECT," *IEEE Trans. Med. Imag.,* vol. 27, no. 2, pp. 204-14, 2008.

[154]   J. Li, R. J. Jaszczak, H. Wang, K. L. Greer, and R. E. Coleman, "Determination of both mechanical and electronic shifts in cone beam SPECT," *Phys. Med. Biol.,* vol. 38, no. 6, pp. 743-54, 1993.

[155]   S. D. Metzler, and R. J. Jaszczak, "Simultaneous multi-head calibration for pinhole SPECT.," *IEEE Trans. Med. Imag.,* vol. 53, pp. 113-120, 2006.

[156]   Y. C. Chen, L. R. Furenlid, D. W. Wilson, and H. H. Barrett, "Calibration of scintillation cameras and pinhole SPECT Imaging systems," *Small Animal SPECT Imaging*, M. A. Kupinski and H. H. Barrett, eds., pp. 195-201, New York: Springer, 2005.

[157]   Z. L. Liu, G. A. Kastis, G. D. Stevenson, H. H. Barrett, L. R. Furenlid, M. A. Kupinski, D. D. Patton, and D. W. Wilson, "Quantitative analysis of acute myocardial infarct in rat hearts with ischemia-reperfusion using a high-resolution stationary SPECT system," *J. Nucl. Med.,* vol. 43, no. 7, pp. 933-939, 2002.

[158]   R. K. Rowe, J. N. Aarsvold, H. H. Barrett, J. C. Chen, W. P. Klein, B. A. Moore, I. W. Pang, D. D. Patton, and T. A. White, "A stationary hemispherical SPECT imager for three-dimensional brain imaging," *J. Nucl. Med.,* vol. 34, no. 3, pp. 474-80, 1993.

[159]   F. Van der Have, B. Vastenhouw, M. Rentmeester, and F. J. Beekman, "System calibration and statistical image reconstruction for ultra-high resolution stationary pinhole SPECT," *IEEE Trans. Med. Imag.,* vol. 27, no. 7, pp. 960-71, 2008.

[160]   B. F. Hutton, I. Buvat, and F. J. Beekman, "Review and current status of SPECT scatter correction," *Phys. Med. Biol.,* vol. 56, no. 14, pp. R85-112, 2011.

[161]   C. L. Chen, Y. Wang, J. J. Lee, and B. M. Tsui, "Toward quantitative small animal pinhole SPECT: assessment of quantitation accuracy prior to image compensations," *Mol. Imaging Biol.,* vol. 11, no. 3, pp. 195-203, 2009.

[162] A. B. Hwang, C. C. Taylor, H. F. VanBrocklin, M. W. Dae, and B. H. Hasegawa, "Attenuation correction of small animal SPECT images acquired with 125I-iodorotenone," *IEEE Trans. Nucl. Sci.,* vol. 53, pp. 1213-1220, 2006.

[163] C. Wu, J. R. de Jong, H. A. Gratama van Andel, F. van der Have, B. Vastenhouw, P. Laverman, O. C. Boerman, R. A. Dierckx, and F. J. Beekman, "Quantitative multi-pinhole small-animal SPECT: uniform versus non-uniform Chang attenuation correction," *Phys. Med. Biol.,* vol. 56, no. 18, pp. N183-N193, 2011.

[164] V. Keereman, Y. Fierens, C. Vanhove, T. Lahoutte, and S. Vandenberghe, "Magnetic resonace-based attenuation correction for micro-single-photon emission computed tomography," *Mol. Imaging,* vol. 11, no. 2, pp. 155-65, 2012.

[165] C. Vanhove, M. Defrise, A. Bossuyt, and T. Lahoutte, "Improved quantification in single-pinhole and multiple-pinhole SPECT using micro-CT information," *Eur. J. Nucl. Med. Mol. Imaging,* vol. 36, no. 7, pp. 1049-1063, 2009.

[166] C. Wu, H. A. Gratama van Andel, P. Laverman, O. C. Boerman, and F. J. Beekman, "Effects of attenuation map accuracy on attenuation-corrected micro-SPECT images," *EJNMMI Res.,* vol. 3, no. 1, pp. 7, 2013.

[167] C. Wu, F. van der Have, B. Vastenhouw, R. A. Dierckx, A. M. Paans, and F. J. Beekman, "Absolute quantitative total-body small-animal SPECT with focusing pinholes," *Eur. J. Nucl. Med. Mol. Imaging,* vol. 37, no. 11, pp. 2127-2135, 2010.

[168] L. T. Chang, "A method for attenuation correction in radionuclide computed tomography," *IEEE Trans. Nucl. Sci.,* vol. 25, pp. 638-43, 1978.

[169] J. E. Bowsher, V. E. Johnson, T. G. Turkington, R. J. Jaszczak, C. R. Floyd, and R. E. Coleman, "Bayesian reconstruction and use of anatomical a priori information for emission tomography," *IEEE Trans. Med. Imag.,* vol. 15, no. 5, pp. 673-86, 1996.

[170] K. Ogawa, Y. Harata, T. Ichihara, A. Kubo, and S. Hashimoto, "A practical method for position-dependent Compton-scatter correction in single photon emission CT," *IEEE Trans. Med. Imag.,* vol. 10, no. 3, pp. 408-12, 1991.

[171] M. F. Smith, and R. J. Jaszczak, "Generalized dual-energy-window scatter compensation in spatially varying media for SPECT," *Phys. Med. Biol.,* vol. 39, no. 3, pp. 531-46, 1994.

[172] F. van der Have, and F. J. Beekman, "Photon penetration and scatter in micro-pinhole imaging: a Monte Carlo investigation," *Phys. Med. Biol.,* vol. 49, no. 8, pp. 1369-86, 2004.

[173] C. T. Badea, X. Guo, D. Clark, S. M. Johnston, C. D. Marshall, and C. A. Piantadosi, "Dual-energy micro-CT of the rodent lung," *Am. J. Physiol. Lung Cell Mol. Physiol.,* vol. 302, no. 10, pp. L1088-97, 2012.

[174] B. De Man, J. Nuyts, P. Dupont, G. Marchal, and P. Suetens, "An iterative maximum-likelihood polychromatic algorithm for CT," *IEEE Trans. Med. Imag.,* vol. 20, no. 10, pp. 999-1008, 2001.

[175] J. Nuyts, B. De Man, J. A. Fessler, W. Zbijewski, and F. J. Beekman, "Modelling the physics in the iterative reconstruction for transmission computed tomography," *Phys. Med. Biol.,* vol. 58, no. 12, pp. r63-96, 2013.

[176] L. Ritschl, S. Sawall, M. Knaup, A. Hess, and M. Kachelriess, "Iterative 4D cardiac micro-CT image reconstruction using an adaptive spatio-temporal sparsity prior," *Phys. Med. Biol.,* vol. 57, no. 6, pp. 1517-25, 2012.

[177] J. P. Schlomka, E. Roessl, R. Dorscheid, S. Dill, G. Martens, T. Istel, C. Baumer, C. Herrmann, R. Steadman, G. Zeitler, A. Livne, and R. Proksa, "Experimental feasibility of multi-energy photon-counting K-edge imaging in pre-clinical computed tomography," *Phys. Med. Biol.,* vol. 53, no. 15, pp. 4031-47, 2008.

[178] G. Zentai, "Comparison of CMOS and a-Si flat panel imagers for X-ray imaging. Imaging Systems and Techniques (IST)," *2011 IEEE International Conference on*, 2011.

[179] J. S. Baba, C. J. Endres, C. A. Foss, S. Nimmagadda, H. Jung, J. S. Goddard, S. Lee, J. McKisson, M. F. Smith, A. V. Stolin, A. G. Weisenberger, and M. G. Pomper, "Molecular imaging of conscious, unrestrained mice with AwakeSPECT," *J. Nucl. Med.,* vol. 54, no. 6, pp. 969-76, 2013.

[180]    S. Gargiulo, A. Greco, M. Gramanzini, S. Esposito, A. Affuso, A. Brunetti, and G. Vesce, "Mice anesthesia, analgesia, and care, Part II: anesthetic considerations in preclinical imaging studies," *ILAR J.,* vol. 53, no. 1, pp. E70-81, 2012.

[181]    I. J. Hildebrandt, H. Su, and W. A. Weber, "Anesthesia and other considerations for in vivo imaging of small animals," *ILAR J.,* vol. 49, no. 1, pp. 17-26, 2008.

[182]    S. K. Carlson, K. L. Classic, C. E. Bender, and S. J. Russell, "Small animal absorbed radiation dose from serial micro-computed tomography imaging," *Mol. Imaging Biol.,* vol. 9, no. 2, pp. 78-82, 2007.

[183]    T. Funk, M. Sun, and B. H. Hasegawa, "Radiation dose estimate in small animal SPECT and PET," *Med. Phys.,* vol. 31, no. 9, pp. 2680-6, 2004.

# 3. Fast spiral SPECT with stationary γ-cameras and focusing pinholes

## *Abstract*

Small-animal SPECT systems with stationary detectors and focusing multiple pinholes (FMP-SPECT) can achieve excellent resolution-sensitivity trade-offs. These systems are able to perform fast total-body scans by shifting the animal bed through the collimator using an automated XYZ stage. However, so far, a large number of highly overlapping central-fields-of-view were used, at the cost of overhead time needed for animal repositioning, and long image reconstruction times due to high numbers of projections views.

In order to improve temporal resolution and reduce image reconstruction time for such scans, we have developed and tested spiral trajectories of the animal bed (ST) requiring fewer steps. In addition, we tested multiplane trajectories of the animal bed (MPT), which is the standard acquisition method of the U-SPECT-II system that is used in this study (MILabs B.V., Utrecht, The Netherlands). Both MPT and ST do not require rotation of the animal. Computer simulations and physical phantom experiments were performed for a wide range of number of bed positions. Furthermore, we tested ST *in vivo* for fast dynamic mouse scans.

We found that ST require less than half the number of bed positions compared to MPT in order to still achieve sufficient sampling. The reduced number of bed positions enabled by ST made it possible to perform a dynamic total-body bone scan and a dynamic hepatobiliary scan with time resolutions of 60 s and 15 s respectively. ST open up new possibilities for high-throughput and fast dynamic radio-molecular imaging.

## 3.1 Introduction

Single photon emission computed tomography (SPECT) is used to quantitatively and visually assess the distribution of radioactive biological markers (tracers) *in vivo* in order to e.g. study animal models of disease and test new pharmaceuticals. Most SPECT systems use rotating detectors and collimators to scan an animal or patient. Alternatively, SPECT systems have been developed which have 360º coverage and use stationary detectors and multi-pinhole collimators, a full ring stationary system being first realized at the University of Arizona [1, 2]. Combining stationary set-ups and focusing multiple pinholes with high pinhole magnification has resulted in dedicated small-animal SPECT systems that have overcome the limitation of poor spatial resolution and sensitivity: sub-half millimeter resolutions over the entire mouse and very detailed images of tracer uptake in tiny sub-compartments of organs and tumors have been achieved [3-16]. In such focusing multi-pinhole SPECT systems (FMP-SPECT), all pinholes focus on a central-field-of-view (CFOV) in order to maximize scan speed and count yield for imaging tumors or organs.

With FMP-SPECT, scans of volumes that are larger than the CFOV (such as total body scans of mice and rats), are performed by gently stepping the animal through the collimator with small steps using a high precision XYZ stage [12]; this warrants adequate sampling (no artifacts in the reconstructed images). Image reconstruction is performed with a dedicated iterative reconstruction algorithm that exploits all projections acquired from all positions of the animal inside the collimator simultaneously, rather than stitching reconstructions of separate sub-volumes (obtained from individual focus positions) together. This combined acquisition and reconstruction method is called the scanning focus method, (SFM [12, 14]). SFM enables both total-body and focused imaging, the latter is achieved by selecting volumes of interest by means of a special graphical user interface that uses radiographs or optical images of the animal.

FMP-SPECT systems that have stationary collimators and detectors are very well suited to perform fast dynamic studies, because there are no heavy detectors and collimators that need to be rotated during scanning. For fast scanning of volumes much larger than the CFOV, the minimum possible scan time crucially depends on the number of bed positions used; a significant fraction of acquisition time can be lost in bed movements when scan times are short (scan time lost in a bed translation is ~0.7 s). However, up to now, acquisition protocols have been relying on a conservatively high number of bed positions to ensure proper sampling (e.g. 100-150 for total-body mouse scans), making these protocols too slow for large-volume SPECT acquisitions with (sub-)minute time resolutions. These protocols use a number of bed positions in the same transaxial plane, whereafter the bed is shifted along the longitudinal axis until the object is scanned along its entire length. These bed trajectories are denoted hereafter as multiplane trajectories (MPT). MPT combined with a conservatively high number of bed positions as used until now guarantee sufficient sampling of the object, because every part of the selected scan volume is positioned at least once inside the CFOV. However, the entire field-of-view (FOV) of the collimator, at a single bed position, is much larger than the CFOV; it extends over the entire tube diameter as is illustrated in Fig. 1a.

Photons from activity outside the CFOV can therefore still be detected by a significant portion of the pinholes. Because the image reconstruction algorithm uses the projection views of all bed positions simultaneously to reconstruct the entire volume, even activity that is never positioned within the CFOV may still be sampled sufficiently well. Therefore, investigating other trajectories than those providing overlapping CFOVs can be very useful.

Main aims of this study are to determine if spiral trajectories (ST) can reduce the required number of bed positions compared to MPT and to demonstrate that ST with low numbers of bed positions can be used for ultra-fast dynamic mouse SPECT.

## *3.2 Materials and methods*

This section starts with an introduction to the scanner and collimator geometry of the U-SPECT-II system (MILabs B.V., Utrecht, The Netherlands) used in this study and a description of the different types of bed trajectories that were tested. Subsequently, digital phantom simulations and physical phantom experiments are described and experimental details of *in vivo* dynamic animal studies are provided. Finally, the image reconstruction algorithm is described.

### 3.2.1 Focusing multi-pinhole SPECT scanner

The collimator geometry of a U-SPECT-II focusing general-purpose mouse collimator is shown in Fig. 1a. The system has three large FOV gamma cameras placed in a triangular configuration with a focusing multi-pinhole collimator positioned at the center of the scanner. In the present study a collimator tube for mouse-sized animals was used [12], both for simulations and experiments. The 75 pinholes in this collimator are arranged in 5 rings of 15 pinholes. Each pinhole has a diameter of 0.6 mm and an opening angle of 30º. All pinholes together observe a FOV that extends over the entire collimator tube diameter (44 mm) and the FOV has the shape of an hourglass (Fig. 1a). The average longitudinal length of the collimator FOV is 25 mm. A part of the FOV, referred to as the CFOV, is sampled by all pinholes simultaneously. Within the CFOV, complete data acquisition is obtained without any translation of the bed. For the mouse collimator used here, the CFOV has a diameter of approx. 12 mm and a longitudinal length of approx. 8 mm. Equipped with this collimator the system achieves a spatial image resolution of 0.45 mm, and 0.35 mm can be achieved when the same collimator has 0.3-mm diameter pinholes [17].

### 3.2.2 Bed trajectories

In this study, images obtained with MPT and ST were compared. Both MPT and ST do not require rotation of the animal. Note that the position of the bed is defined as the

position of center of the selected scan volume in the coordinate system of the collimator. This coordinate system has its origin at the center of the CFOV, and the x-axis and y-axis lie perpendicular to the collimator's longitudinal axis, which is the z-axis (Fig. 1a). Both MPT and ST are step-and-shoot acquisition techniques, where the coordinates of successive bed positions lie either in multiple planes perpendicular to the collimator's longitudinal axis (MPT) or on a spiral curve (ST). In order to maximize scan speed, the bed does not follow a curve if the bed is repositioned, but rather the shortest path between successive bed positions. Both types of bed trajectories were tested for a decreasing number of bed positions to see when artifacts might appear in the reconstructed images. The MPT consist of longitudinally repeating scan planes with each scan plane having four transaxial bed positions (no longitudinal movement of the bed within a scan plane). Orientations of bed positions of successive scan planes were transaxially rotated by 45°; this way bed positions of successive scan planes minimally overlap especially when the longitudinal distance between subsequent scan planes was small (Fig. 1b). By doing this, angular sampling of the scanned volume was improved compared to successive scan planes that have the same transaxial position pattern. In order to test acquisitions with different numbers of bed positions, the longitudinal distances between subsequent scan planes were changed.
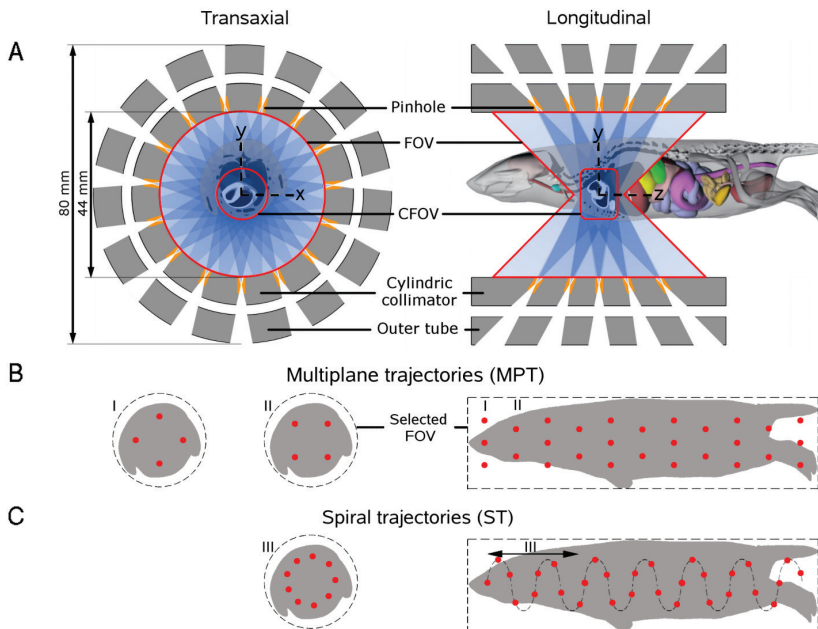


**Figure 1.** *(a) Illustration of mouse in collimator with focusing pinholes. (b) MPT with 4 transaxial CFOV positions (red dots) per longitudinal position. Orientation of CFOV positions are rotated by 45° in successive planes. (c) ST with 4.5 CFOV positions per spiral pitch length (after 9 bed steps, or two pitch lengths, bed returns to same transaxial position). Note that for both MPT and ST mouse bed is only shifted (not rotated) to position mouse in CFOV.*

To explain this in a more precise mathematical way; for a scan of a cylindrical volume (radius $R$ and length $L$) that is performed with $J > 1$ scan planes ($4J$ bed positions), the coordinates of bed position $i$ ($i=1...4$) in scan plane $j$ ($j=1...J$) are defined as:

$$x(i, j) = (R - R_f)\cos\left(\frac{\pi}{2}(i-1)\right)$$
$$y(i, j) = (R - R_f)\sin\left(\frac{\pi}{2}(i-1)\right) \quad \Bigg\} \quad \text{for odd } j$$

$$x(i, j) = (R - R_f)\cos\left(\frac{\pi}{2}(i-1)+\frac{\pi}{4}\right)$$
$$y(i, j) = (R - R_f)\sin\left(\frac{\pi}{2}(i-1)+\frac{\pi}{4}\right) \quad \Bigg\} \quad \text{for even } j \qquad (1)$$

$$z(i, j) = \left(\frac{L-\delta}{J-1}\right)(j-1)-\left(\frac{L-\delta}{2}\right) \qquad \text{for all } j$$

Here $R_f$ is the transaxial radius of the CFOV and $\delta$ is the longitudinal length of the CFOV. Note that these equations are valid if $R_f \leq R$ and $\delta \leq L$, which is the case for large-volume scans such as total-body scans.

If MPT are used with fewer bed positions, the longitudinal distances between the scan planes increase. In this case, the regions around the scan planes might be sampled sufficiently, whereas there is insufficient sampling in between these regions, because the interplanar distances are too large. If the bed follows a spiral trajectory, every bed position has a different longitudinal coordinate resulting in more uniform sampling of the object in the longitudinal direction compared to MPT. Therefore, ST might still achieve sufficient sampling for a lower number of bed positions than MPT.

For the ST investigated here, the spiral pitch length was varied in order to vary the number of bed positions. ST had 4.5 bed positions per spiral pitch and the bed returned to its initial transaxial position after 9 bed steps (two times the spiral pitch, Fig. 1c). This way, angular sampling of the scanned volume was improved compared to repeating the same transaxial position pattern with 4 bed positions each spiral pitch, especially in cases where the longitudinal step between successive bed positions was small. To put this description in equations, for ST with $N > 1$ bed positions, the coordinates of bed position $n$ in a scan of the above mentioned volume are defined as:

$$x(n) = (R - R_f)\cos\left(\frac{2\pi}{4.5}(n-1)\right)$$
$$y(n) = (R - R_f)\sin\left(\frac{2\pi}{4.5}(n-1)\right) \qquad (2)$$
$$z(n) = \left(\frac{L-\delta}{N-1}\right)(n-1)-\left(\frac{L-\delta}{2}\right)$$

## 3.2.3 Phantom scans

In order to test the performance of MPT and ST for different numbers of bed positions, scans of phantoms that are challenging for limited sampling were simulated and experimentally performed.

### 3.2.3.1 Digital image quality phantom scan simulations

The digital phantom (Fig. 2a) has a cylindrical shape with a diameter of 24 mm and a length of 90 mm (approximately the size of a mouse). This phantom addresses image uniformity and data completeness and consists of a uniform section and two Defrise disk phantom inserts with disk sets perpendicular and parallel to the long axis of the phantom (thickness of the disks and spacing between disks are both 1.5 mm). Note that the Defrise phantom is often used for studying the effects of incomplete data in various cone-beam-like geometries (e.g. pinhole SPECT and multi-slice CT). In order to mimic a realistic continuous activity distribution the voxel size of the phantom was 0.15 mm, half the size of the voxel size in the reconstructed image. To investigate possible bias effects on reconstructed images introduced by the sampling quality of the bed trajectories, high count projections were required. Therefore, high activity concentrations of 51 MBq/ml and a scan time of 30 min were assumed in the simulations [18].

The fast simulator used in this study is based on ray tracing to account for resolution-degrading effects of pinhole diameter and pinhole edge penetration [19, 20]. The radionuclide that was simulated is $^{99m}$Tc (140 keV gamma photons). The intrinsic resolution of the detectors and detection efficiency for 140 keV photons was set in correspondence with experimental data to a Gaussian response with a full-width-at-half-maximum (FWHM) of 3.5 mm and 89%, respectively. The simulator was used to simulate phantom projection data and to pre-calculate the system matrix by simulating point sources. To emulate noise, Poisson statistics were generated for the simulated projection data, taking into account administered activity and scan duration.

The accuracy of the reconstructed phantom images was visually evaluated by image profiles through longitudinal phantom slices and expressed in terms of the *normalized mean error* (NME) and *normalized mean square error* (NMSE) between a *volume-of-interest* (VOI) in the reconstructed images and the corresponding region in the digital phantom. The VOI was a cylindrical region with diameter and length of 18 mm and 87 mm respectively, and was centered and aligned with the digital phantom. In order to calculate both errors, the digital phantom was resampled to the voxel size of the reconstructed images. Let λ be the summed activity over all *M* voxels inside the VOI of the digital phantom:

$$\lambda = \sum_{i=1}^{M} \lambda_i \tag{3}$$

Similarly, the summed activity $\tilde{\lambda}$ over all $M$ voxels of the corresponding VOI in the reconstructed image can be calculated. With the above definitions, the NME between the digital phantom and reconstructed image can be written as:

$$NME = \sum_{i=1}^{M} \left| \left( \frac{\tilde{\lambda}_i}{\tilde{\lambda}} - \frac{\lambda_i}{\lambda} \right) \right| \tag{4}$$

The NMSE is expressed by:

$$NMSE = \sum_{i=1}^{M} \left( \frac{\tilde{\lambda}_i}{\tilde{\lambda}} - \frac{\lambda_i}{\lambda} \right)^2 \tag{5}$$

### 3.2.3.2 Physical Defrise phantom scans

Experimental phantom scans were performed using a Defrise phantom consisting of a set of parallel polymethylmethacrylate disks (Data Spectrum Corp.). The 20 mm diameter disks were 1.5 mm thick and the spacing between them equals their thickness (equivalent to the image quality phantom used in the scan simulations). The length of the phantom was 25.5 mm. Spaces between the disks were filled with 384 MBq $^{99m}$Tc-pertechnetate and the phantom was scanned for 30 min. Because the longitudinal length of the physical Defrise phantom was 3.5 times smaller than the length of the digital image quality phantom described in the previous section, the scans performed here using $N$ bed positions in the scan acquisition can be compared with the scan simulations of the digital image quality phantom using 3.5 x $N$ bed positions in the scan acquisition.

## 3.2.4 Animal studies

The dynamic capabilities that come into reach with the development of ST were illustrated by a dynamic total-body mouse bone scan and a dynamic hepatobiliary scan of the mouse's thorax and abdomen. All scans were obtained using ST that performed best in the phantom scans (smallest number of bed positions and still adequate sampling). Animal studies were conducted following protocols approved by the Animal Research Committee of the University Medical Center Utrecht. During all procedures, the animals' body temperatures were kept at approximately 37 ºC by a thin heating mat that was integrated in the bed.

### 3.2.4.1 Dynamic bone scan

A dynamic total-body bone scan of a mouse was performed using $^{99m}$Tc-hydroxymethylene diphosphonate ($^{99m}$Tc-HDP). A 29.5 g male mouse was anesthetized with

isoflurane. An amount of 189 MBq $^{99m}$Tc-HDP was injected in the tail vein. Scanning started right before radioligand injection and the mouse was scanned for 60 min in time frames of 1 minute.

From the reconstructed images, VOIs were selected covering the heart, the kidneys, the left shoulder, the left knee and the bladder. For each organ or structure the VOI outline was drawn in the reconstructed image where the organ or structure was most clearly visible. From these VOIs, time-activity-curves (TACs) were derived by measuring the average activity concentration in each VOI for each time frame.

### 3.2.4.2 Dynamic hepatobiliary scan

A dynamic hepatobiliary scan of the mouse's thorax and abdomen was performed. $^{99m}$Tc-mebrofenin is indicated as an imaging agent for the evaluation of the hepatobiliary tract. $^{99m}$Tc-mebrofenin was injected into the blood stream where it circulated to the liver and was excreted into the bowel. The scan area that was selected stretched from the pelvis to the neck. A 25 g male mouse was anesthetized with isoflurane and an amount of 145 MBq $^{99m}$Tc-mebrofenin (Bridatec, GE-Amersham Health) was injected via the tail vein. Right before radioligand injection, scanning started and the mouse was scanned for 5 min in time frames of 15 s. From the reconstructed images, VOIs were selected covering the vena cava inferior, the heart, the liver, the gallbladder and the duodenum. Each VOI outline was drawn in the reconstructed image where the organ was most clearly visible. TACs were derived by measuring the average activity concentration in each VOI for each time frame.

### 3.2.5 Image Reconstruction

The images of the digital image quality phantom scan simulations and physical Defrise phantom scans were reconstructed from the projections using the Pixel-based Ordered Subset Expectation Maximization algorithm (POSEM) with 16 subsets and 10 iterations. POSEM deviates from traditional OSEM image reconstruction in that subsets do not consist of grouped projection views, but the pixels in each subset are spread out in a regular pattern over the entire detector. At high acceleration factors (high numbers of subsets), images reconstructed with POSEM are closer to equivalent images reconstructed with MLEM compared to images reconstructed with OSEM with traditional selection of subsets [18]. The images of the digital image quality phantom scan simulations were reconstructed on a 0.3 mm voxel grid and these images were post-filtered with a Gaussian filter with a FWHM of 0.4 mm. For the physical Defrise phantom scans a photopeak window with a width of 25% was set around the $^{99m}$Tc photopeak. Images were reconstructed on a 0.2 mm voxel grid and were also post-filtered with a Gaussian filter with a FWHM of 0.4 mm.

For the dynamic bone scan, 60 images (from 60x1 min time frames) were reconstructed. For the dynamic hepatobiliary scan, 20 images (from 20x15 s time frames) were reconstructed. For both animal studies, a photopeak window with a width of 25% was

set around the [99mTc] photopeak. Because of the low-count projection data resulting from the short scan times per frame, only a low number of iterations were needed and the images were therefore reconstructed using an MLEM algorithm with 10 iterations. The voxel size of the reconstructed images was 0.4 mm. The reconstructed images were post-filtered using an edge and flux preserving Perona-Malik nonlinear diffusion filter (parameters: gradient modulus threshold = 10, integration constant = 3/44 and 2 iterations) [21].

## *3.3 Results*

### 3.3.1 Phantom Scans

#### 3.3.1.1 Digital image quality phantom scan simulations

Figure 2b shows longitudinal image profiles through the transaxial center of the reconstructed phantom images together with the digital phantom profile (ground truth). Both the slice thickness and the profile width were 3 mm. These image profiles show that the accuracy of the reconstructed images acquired with MPT degrades significantly faster than when using ST as the number of bed positions decreases; the image profile of MPT with 60 bed positions already shows a considerable mismatch in the middle section of the phantom, while the image profile of ST with 28 bed positions shows only a slight degradation. Figure 3 shows the NME (Fig. 3a) and NMSE (Fig. 3b) of the images of the image quality phantom scan simulations as a function of the number of bed positions, both for MPT and ST. ST resulted in a lower NME and NMSE than MPT at an equal number of bed positions, for all simulated bed trajectories. The increase in both errors for a decreasing number of bed positions is significantly less for ST than for MPT.
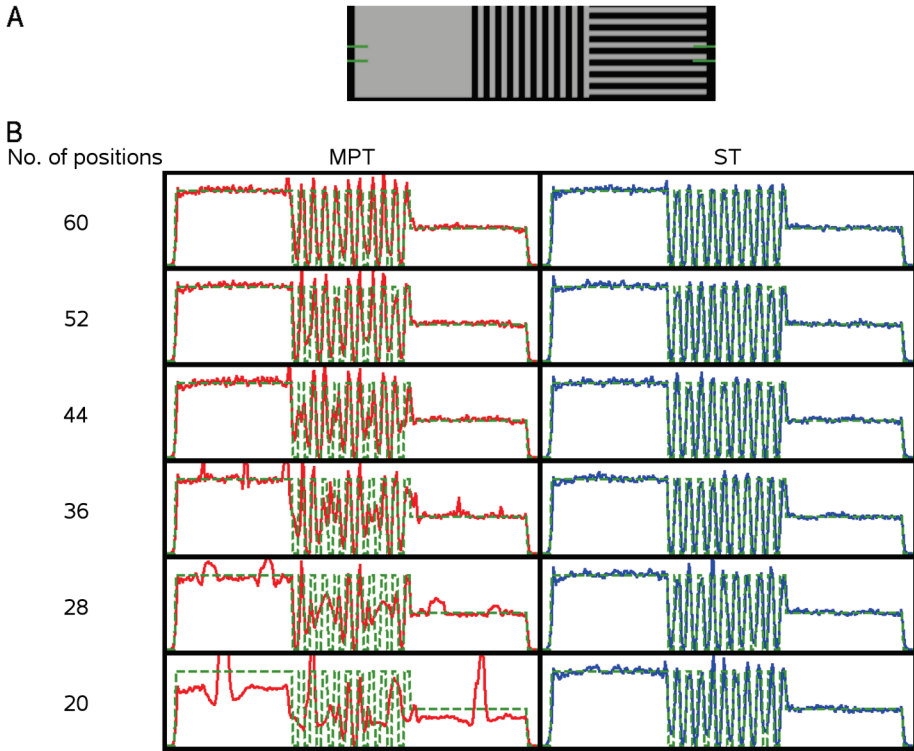
**Figure 2.** *(a) Digital image quality phantom with longitudinal profile region between green lines. (b) Image profiles through center of reconstructed phantom images for simulated scans with MPT (left column) and ST (right column) relative to original digital image quality phantom (dashed green line) for decreasing number of bed positions.*
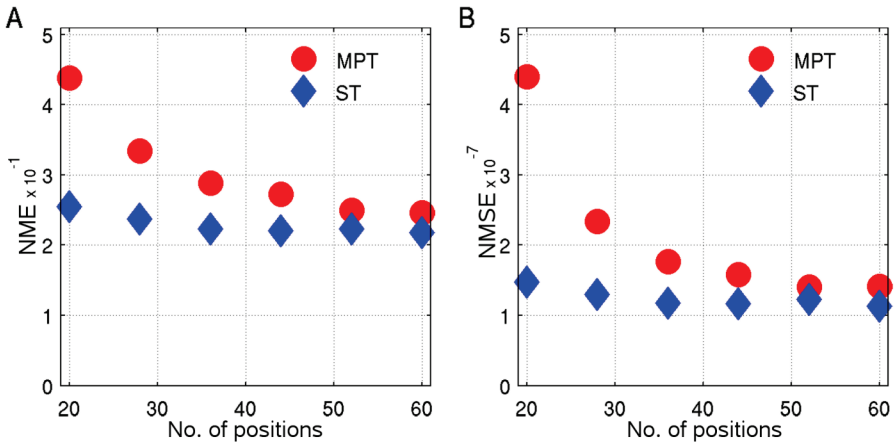


**Figure 3.** *(a) NME and (b) NMSE of reconstructed image quality phantom images as function of number of bed positions for MPT (red circles) and ST (blue diamonds).*

### 3.3.1.2 Physical Defrise phantom scans

Figure 4 shows 3 mm thick slices through the reconstructed images of the physical Defrise phantom acquired with MPT and ST for a decreasing number of bed positions. The experimental images convey the same message as the results of the scan simulations reported in the previous paragraph: MPT lead to axial blurring artifacts when the number of bed positions becomes 16 or less, corresponding to MPT with about 60 or less bed positions in the phantom scan simulations. Images acquired with ST start to show slight image degradation for 8 bed positions and still show no significant axial blurring artifacts. This result corresponds to ST with 28 bed positions in the phantom scan simulations.
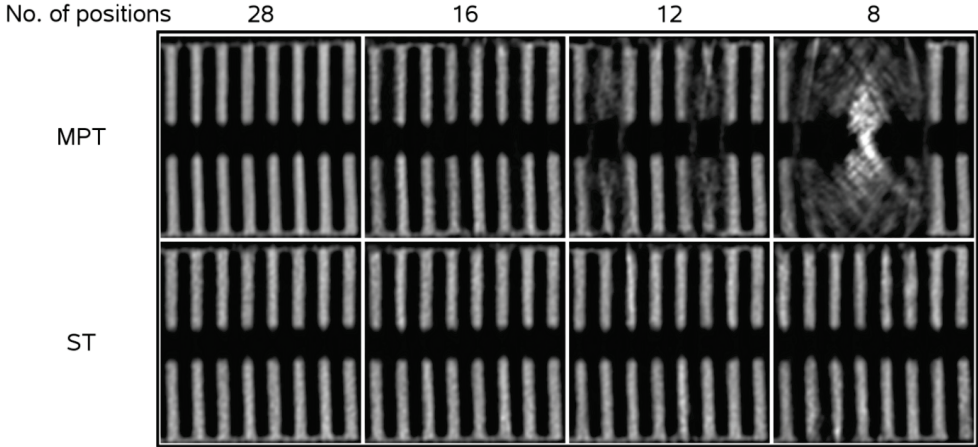


**Figure 4.** *Longitudinal slices through disks of the reconstructed physical Defrise phantom images for MPT (top row) and ST (bottom row) for decreasing number of bed positions.*

### 3.3.2 Animal Studies

All *in vivo* scans were performed using ST with an average longitudinal bed step size of 3.4 mm (equal to the bed step size of ST with 28 bed positions in the phantom scan simulations or the bed step size of ST with 8 bed positions in the physical Defrise phantom scans). This way, 23 bed positions were needed to scan the selected scan volume for the dynamic total-body bone scan and 9 bed positions were needed to perform the dynamic hepatobiliary scan.

### 3.3.2.1 Dynamic bone scan

Figure 5a shows sagittal maximum-intensity-projections (MIPs) of the distribution of $^{99m}$Tc-HDP in a mouse at different time frames with a time resolution of 1 minute. Figure 5b shows TACs of the tracer concentration in several organs and structures. In the first minutes after injection, highest tracer concentrations were in the heart, the liver, the kidneys and the bladder. From the tenth minute, uptake in the bone reached activity levels high enough so that bony structures like the left shoulder, the spine and left knee became clearly visible.
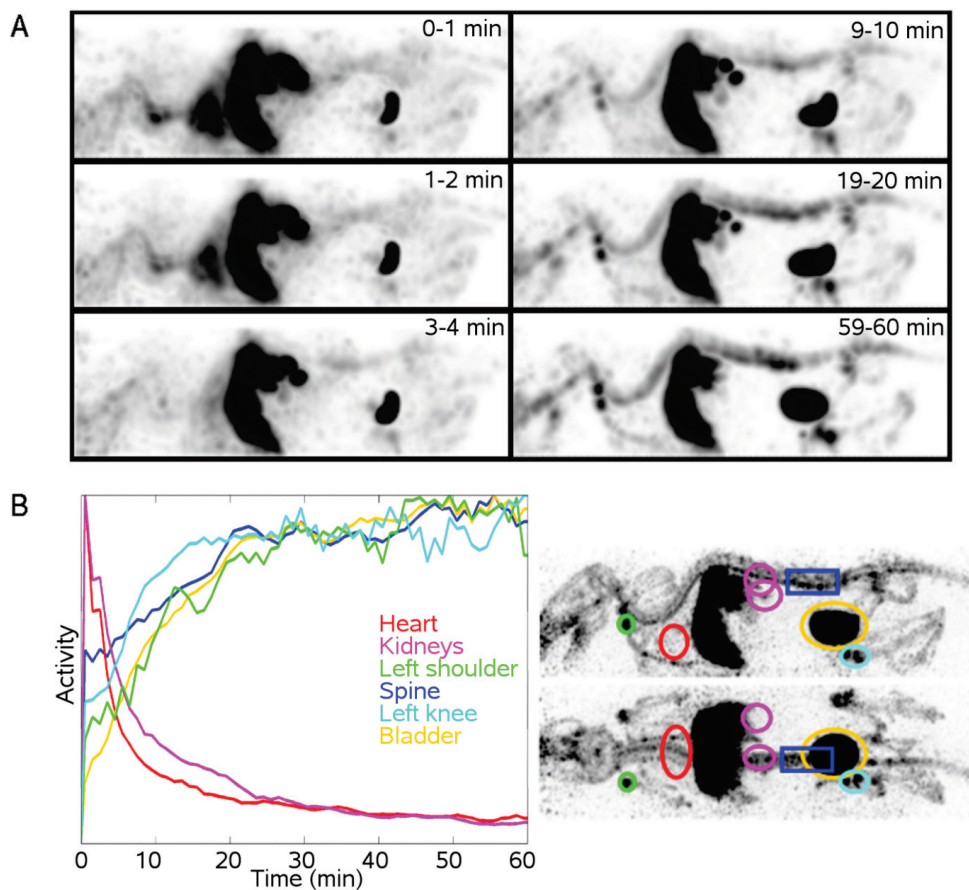


**Figure 5.** *(a) Top-to-bottom, left-to-right: MIPs of reconstructed dynamic $^{99m}$Tc-HDP scan with 1 minute time frames at different time points. (b) Left: TACs for several organs and structures. Each curve is normalized to its maximum. Right: Illustration of VOIs projected onto sagittal and coronal MIPs of high count reconstruction of summed projection data of last 30 frames (31-60 min).*

### 3.3.2.2 Dynamic hepatobiliary scan

Figure 6a shows a time series of coronal MIPs of the reconstructed dynamic $^{99m}$Tc-Mibrofenin scan with 15 s time frames. Figure 6b shows TACs of the tracer concentration in several organs. The tracer traveled via the vena cava inferior into the heart, went into the liver and accumulated in the gallbladder. The tracer finally left the gallbladder via the duodenum. Videos of both dynamic scans are available online as supplemental data at http://jnm.snmjournals.org.
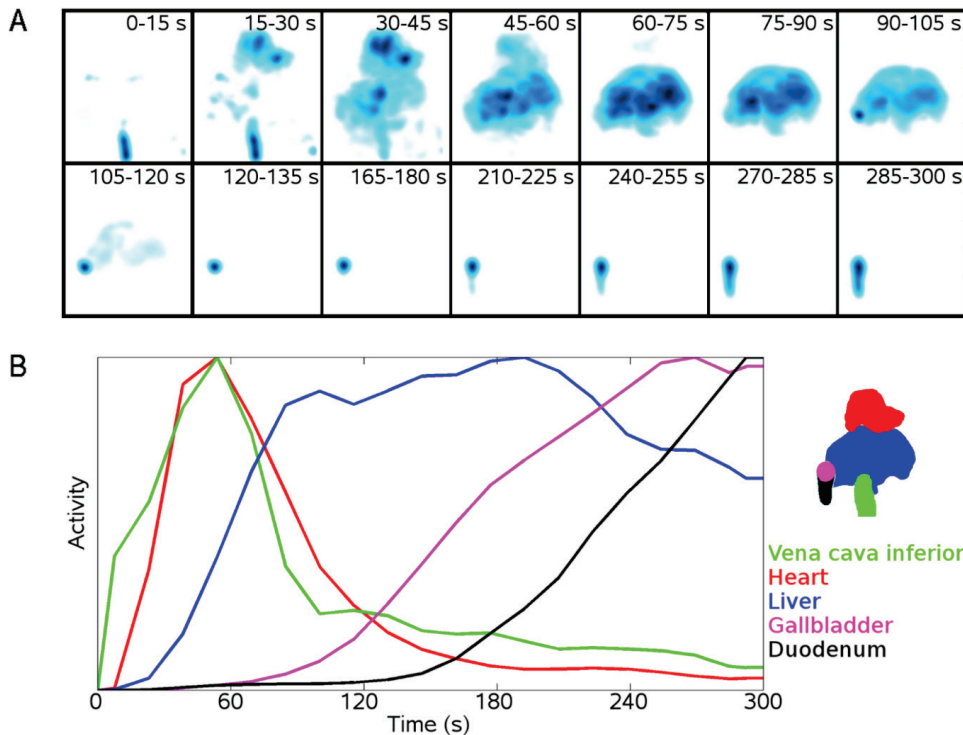


**Figure 6.** *(a) Left-to-right, top-to-bottom: MIPs of the reconstructed dynamic $^{99m}$Tc-Mibrofenin scan with 15 s time frames. (b) Left: TACs for several organs. Each curve is normalized to its maximum. Right: Coronal projections of the VOIs.*

## 3.4 Discussion

This study proposes fast acquisition protocols for total body SPECT with focusing pinhole collimators. The conducted experiments indicate that ST are suitable for fast total-body SPECT since the number of bed positions can be much smaller than with MPT. This lowers the overhead time due to bed repositioning and allows for speeding up image reconstruction.

The geometry of different U-SPECT-II collimators for mouse and rat imaging is very similar (cylindrical tubes with pinholes focusing on a central volume). Therefore, ST for fast dynamic SPECT imaging may well be applicable to other purpose-build focusing multi-pinhole collimators currently in use with this device (e.g. general-purpose rat collimator and high-sensitivity mouse collimator with 1 mm pinholes). However, to confirm this, further validation is required for these collimators.

In this paper, fast total-body mouse imaging with (sub-)minute resolutions was enabled by diminishing the number of bed positions. One could think of bringing imaging time further down by reducing the time that is lost per bed translation by increasing the speed of the XYZ stage during bed movements. However, there is a trade-off between the speed and accuracy of the XYZ stage; reduced positioning accuracy might lead to artifacts in the reconstructed images [14].

Time resolutions of dynamic total-body mouse scans that can be achieved by FMP-SPECT are also subject to collimator sensitivity. The higher a collimator's sensitivity, the faster a certain number of photons can be collected. However, increasing the collimator's sensitivity (e.g. by employing pinholes with larger diameters) may affect image resolution. Here we improved overall count yield at a fixed resolution-sensitivity trade-off of the system by significantly decreasing overhead times due to translations of the animal bed. However, with lower administered activities and shorter scan times, higher sensitivity, accomplished by, for example, the use of larger-diameter pinholes, may be beneficial. A high-sensitivity mouse collimator with 1 mm pinholes was recently constructed for U-SPECT-II and has about 2.5 times higher sensitivity than the collimator used for the present studies (0.6 mm pinholes). The ability to perform (fast) dynamic total-body small-animal SPECT may enable study types like tracer kinetic modeling in large body volumes, a research area that is currently dominated by small-animal PET.

ST allows for reducing the required number of bed positions by a factor of more than two compared to MPT. Therefore, for scans performed with ST, the number of projection bins used for image reconstruction can be more than halved compared to scans performed with MPT. The time needed for the forward-projection step and back-projection step in the reconstruction algorithm can therefore be reduced more than twofold compared to scans that are performed with MPT [14]. This is desirable, especially in studies where many images have to be reconstructed, like high-throughput studies or dynamic studies, where every scan consists of many short time frames.

## 3.5 Conclusions

This paper introduces ST of the animal bed in order to perform fast dynamic imaging with FMP-SPECT systems with a stationary detector set-up. Phantom studies show that ST can be used with a more than twofold smaller number of bed positions than MPT. The feasibility of applying ST to fast mouse scans was demonstrated, opening up new possibilities for high-throughput and fast dynamic SPECT studies.

**Acknowledgements**

## *Bibliography*

[1]     L. R. Furenlid, D. W. Wilson, Y. C. Chen, H. Kim, P. J. Pietraski, M. J. Crawford, and H. H. Barrett, "FastSPECT II: A Second-Generation High-Resolution Dynamic SPECT Imager," *IEEE Trans. Nucl. Sci.,* vol. 51, no. 3, pp. 631-635, 2004.

[2]     W. P. Klein, H. H. Barrett, I. W. Pang, D. D. Patton, M. M. Rogulski, J. D. Sain, and W. E. Smith, "FASTSPECT: electrical and mechanical design of a high-resolution dynamic SPECT imager," *Nuclear Science Symposium and Medical Imaging Conference Record, 1995., 1995 IEEE,* vol. 2, pp. 931-933 vol.2, 1995.

[3]     F. Beekman, and F. van der Have, "The pinhole: gateway to ultra-high-resolution three-dimensional radionuclide imaging," *Eur. J. Nucl. Med. Mol. Imaging,* vol. 34, no. 2, pp. 151-61, 2007.

[4]     F. J. Beekman, F. van der Have, B. Vastenhouw, A. J. van der Linden, P. P. van Rijk, J. P. Burbach, and M. P. Smidt, "U-SPECT-I: a novel system for submillimeter-resolution tomography with radiolabeled molecules in mice," *J. Nucl. Med.,* vol. 46, no. 7, pp. 1194-200, 2005.

[5]     W. Branderhorst, B. Vastenhouw, F. van der Have, E. L. Blezer, W. K. Bleeker, and F. J. Beekman, "Targeted multi-pinhole SPECT," *Eur. J. Nucl. Med. Mol. Imaging,* vol. 38, no. 3, pp. 552-61, 2011.

[6]     S. De Bruyne, L. Wyffels, T. L. Boos, S. Staelens, S. Deleye, K. C. Rice, and F. De Vos, "In vivo evaluation of [123I]-4-(2-(bis(4-fluorophenyl)methoxy)ethyl)-1-(4-iodobenzyl)piperidine, an iodinated SPECT tracer for imaging the P-gp transporter," *Nucl. Med. Biol.,* vol. 37, no. 4, pp. 469-77, 2009.

[7]     A. L. Goertzen, D. W. Jones, J. Seidel, K. Li, and M. V. Green, "First results from the high-resolution mouseSPECT annular scintillation camera," *IEEE Trans. Med. Imag.,* vol. 24, no. 7, pp. 863-7, 2005.

[8]     M. A. King, P. H. Pretorius, T. Farncombe, and F. J. Beekman, "Introduction to the physics of molecular imaging with radioactive tracers in small animals," *J. Cell. Biochem. Suppl.,* vol. 39, pp. 221-30, 2002.

[9]     Z. L. Liu, G. A. Kastis, G. D. Stevenson, H. H. Barrett, L. R. Furenlid, M. A. Kupinski, D. D. Patton, and D. W. Wilson, "Quantitative analysis of acute myocardial infarct in rat hearts with ischemia-reperfusion using a high-resolution stationary SPECT system," *J. Nucl. Med.,* vol. 43, no. 7, pp. 933-939, 2002.

[10]   D. P. McElroy, L. R. MacDonald, F. J. Beekman, Y. C. Wang, B. E. Patt, J. S. Iwanczyk, B. M. W. Tsui, and E. J. Hoffman, "Performance evaluation of A-SPECT: A high resolution desktop pinhole SPECT system for imaging small animals," *IEEE Trans. Nucl. Sci.,* vol. 49, no. 5, pp. 2139-2147, 2002.

[11]   S. R. Meikle, P. Kench, A. G. Weisenberger, R. Wojcik, M. F. Smith, S. Majewski, S. Eberl, R. R. Fulton, A. B. Rosenfeld, and M. J. Fulham, "A prototype coded aperture detector for small animal SPECT," *IEEE Trans. Nucl. Sci.,* vol. 49, no. 5, pp. 2167-2171, 2002.

[12]   F. Van der Have, B. Vastenhouw, R. M. Ramakers, W. Branderhorst, J. O. Krah, C. Ji, S. G. Staelens, and F. J. Beekman, "U-SPECT-II: An Ultra-High-Resolution Device for Molecular Small-Animal Imaging," *J. Nucl. Med.,* vol. 50, no. 4, pp. 599-605, 2009.

[13]   C. Van Steenkiste, S. Staelens, S. Deleye, F. De Vos, S. Vandenberghe, A. Geerts, C. Van de Wiele, M. De Vos, H. Van Vlierberghe, and I. Colle, "Measurement of porto-systemic shunting in mice by novel three-dimensional micro-single photon emission computed tomography imaging enabling longitudinal follow-up," *Liver Int.,* vol. 30, no. 8, pp. 1211-20, 2010.

[14]   B. Vastenhouw, and F. Beekman, "Submillimeter total-body murine imaging with U-SPECT-I," *J. Nucl. Med.,* vol. 48, no. 3, pp. 487-93, 2007.

[15]   B. Vastenhouw, F. van der Have, A. J. van der Linden, L. von Oerthel, J. Booij, J. P. Burbach, M. P. Smidt, and F. J. Beekman, "Movies of dopamine transporter occupancy with ultra-high resolution focusing pinhole SPECT," *Mol. Psychiatry,* vol. 12, no. 11, pp. 984-7, 2007.

[16]   T. Wyckhuys, S. Staelens, B. Van Nieuwenhuyse, S. Deleye, H. Hallez, K. Vonck, R. Raedt, W. Wadman, and P. Boon, "Hippocampal deep brain stimulation induces decreased rCBF in the hippocampal formation of the rat," *Neuroimage,* vol. 52, no. 1, pp. 55-61, 2010.

[17]   F. Van der Have, B. Vastenhouw, M. Rentmeester, and F. J. Beekman, "System calibration and statistical image reconstruction for ultra-high resolution stationary pinhole SPECT," *IEEE Trans. Med. Imag.,* vol. 27, no. 7, pp. 960-71, 2008.

[18]   W. Branderhorst, B. Vastenhouw, and F. J. Beekman, "Pixel-based subsets for rapid multi-pinhole SPECT reconstruction," *Phys. Med. Biol.,* vol. 55, no. 7, pp. 2023-34, 2010.

[19]   M. Gieles, H. W. de Jong, and F. J. Beekman, "Monte Carlo simulations of pinhole imaging accelerated by kernel-based forced detection," *Phys. Med. Biol.,* vol. 47, no. 11, pp. 1853-67, 2002.

[20]   M. C. Goorden, F. Van der Have, R. Kreuger, and F. J. Beekman, "An efficient simulator for pinhole imaging of PET isotopes," *Phys. Med. Biol.,* vol. 56, no. 6, pp. 1617-34, 2011.

[21]   P. Perona, and J. Malik, "Scale-Space and Edge-Detection Using Anisotropic Diffusion," *IEEE Trans. Pattern Anal. Mach. Intell.,* vol. 12, no. 7, pp. 629-639, 1990.

# 4. Simultaneous SPECT-PET imaging in rats

P. E. B. Vaissier, F. van der Have, M. C. Goorden, O. Ivashchenko, B. Vastenhouw, R. M. Ramakers, and F. J. Beekman. "Simultaneous SPECT-PET imaging in rats," in preparation.

## *Abstract*

Single Photon Emission Computed Tomography (SPECT) and Positron Emission Tomography (PET) are key modalities in preclinical imaging of small animals as they are widely used to study molecular mechanisms *in vivo* or in the development of new pharmaceuticals. Recently, SPECT and PET imaging have been combined in a novel versatile emission computed tomography system (VECTor). VECTor enables simultaneous sub-mm imaging of single-photon and positron emitting radio-labeled tracer molecules in mice by means of a dedicated clustered multi-pinhole (CMP) collimator that can be mounted on existing U-SPECT platforms. Here we present and validate the extended capability of VECTor to also image rat-sized small animals with a newly developed CMP collimator. It allows to perform simultaneous SPECT-PET by collimating gamma photons that are emitted by single-photon emitters as well as those produced after positron-electron annihilation. Compared to pinholes used in conventional SPECT collimators, the pinholes in the CMP collimator have more narrow opening angles to reduce photon penetration through the pinhole edges by high-energy annihilation photons. We validated our new collimator by performing resolution phantom scans, sensitivity measurements and simultaneous SPECT-PET scans of rats. For PET tracers ($^{18}$F), the tomographic resolution obtained with a Jaszczak hot rod phantom was 1.3 mm, while 1.1 mm resolution images of SPECT tracers ($^{99m}$Tc) were acquired. Capabilities of the system were further illustrated by simultaneously acquired SPECT-PET scans of rats (i.e. a cardiac scan, a brain scan and bone scans) including a fast dynamic scan with a temporal resolution of 20 s. With a new larger-diameter CMP collimator, VECTor now uniquely enables simultaneous SPECT-PET imaging of rats. Using VECTor, scientists can select the most suitable combinations of radiotracers from the entire complement of available SPECT and PET tracers to study the correlation between different biological functions in the same animal at the same time with a single dose of anesthesia.

## *4.1 Introduction*

Single Photon Emission Computed Tomography (SPECT) and Positron Emission Tomography (PET) imaging of small animals are key modalities in molecular imaging and are applied to study animal models of disease and test new pharmaceuticals [1, 2].

Over the last decade, the resolution of preclinical SPECT has improved dramatically [3-7]. Current state-of-the-art preclinical SPECT uses multiple pinholes that produce magnified projections of the tracer distribution on the gamma detectors. This way, small details can be resolved within small animals: reconstructed spatial resolutions of these systems can reach well below 0.5 mm in mice [8, 9]. Due to the larger size of rats, lower pinhole magnification factors are attained than with mice, which results in resolution degradation, although resolutions in rats can still reach below 0.75 mm [8].

Traditionally, preclinical PET is based on electronic collimation to construct a line-of-response between each detector pair that detected two 511 keV photons in coincidence. A 3-dimensional image of the tracer distribution can be reconstructed from these lines-of-response. However, a number of physical factors have a negative influence on PET spatial resolution, like finite positron range and non-collinearity of the detected 511 keV photon pairs, factors which are hard to correct. Additionally, compared to pinhole collimation, reconstructed resolution with electronic collimation depends much stronger on the intrinsic resolution of the detectors, including depth-of-interaction (DOI) effects. State-of-the-art preclinical coincidence PET can reach spatial resolutions around 1 mm [10-15], while commercially available coincidence PET systems generally reach resolutions that are a bit lower [16, 17].

In contrast to SPECT, simultaneous multi-tracer imaging with PET can be challenging since annihilation photons always have an energy of 511 keV  and it is therefore not possible to distinguish between gamma-photons originating from different PET tracers based on their energies. In order to enable multi-tracer PET imaging, effort is being spent in developing techniques that attempt to separate the tracer signals based on prior knowledge about the kinetics, distributions and decay rates of the injected tracers [18-21]. Next to adding complexity to the image reconstruction process or to kinetic parameter estimation, the reliability of the results that are obtained which such methods strongly depend on accuracy of the models that are used.

Imaging platforms that can perform SPECT and PET can take advantage of the entire complement of available SPECT and PET tracers. Most commercial imaging platforms that are capable of SPECT and PET apply a tandem configuration of a pinhole SPECT system with a coincidence PET system and these systems can therefore not perform truly simultaneous SPECT-PET. However, images reconstructed from truly simultaneously acquired SPECT and PET data are inherently registered in space and time, which allows for correlating multiple biological functions in one animal at a single time point. Such a system was recently introduced, namely the Versatile Emission Computed Tomography (VECTor) system [22]. VECTor applies physical (pinhole) collimation for gamma photons resulting from SPECT and PET tracer decay [23].  To decrease the effect of penetration of 511 keV gamma photons through the pinhole edges, which could severely degrade image resolution,

pinholes had relatively narrow opening angles. In order to compensate for the limited field-of-view (FOV) of narrow pinholes, pinholes were clustered in groups of four and within a cluster each pinhole sampled a different part of the FOV (Fig. 1a). This way, approximately the same area could be sampled as with traditional pinholes that have larger opening angles. As a result, the reconstructed spatial resolution of pinhole PET for ^{18}F in mice was found to be 0.75 mm [22]. It was also shown in [22] that SPECT images were hardly degraded by the simultaneous presence of a PET tracer, even for cases in which the activity concentration of the PET tracer exceeded the activity concentration of the SPECT tracer by up to a factor of 2.5.

The dedicated clustered multi-pinhole (CMP) collimator in [22] had a diameter suitable for imaging mouse-sized animals. In this work we present and test a CMP collimator that can also be used to image rat-sized animals. Compared to the CMP mouse collimator, the tungsten cylindrical CMP rat collimator (Fig. 1b) has a larger bore-size to accommodate rats, a larger FOV, and larger-diameter pinholes to compensate for reduced sensitivity due to the average increase in source-to-pinhole distance. We evaluate the performance of VECTor equipped with this collimator by sensitivity measurements, resolution-phantom scans and we show results of simultaneously acquired multiple functional data obtained from rats that were injected with a mix of a SPECT and a PET tracer.
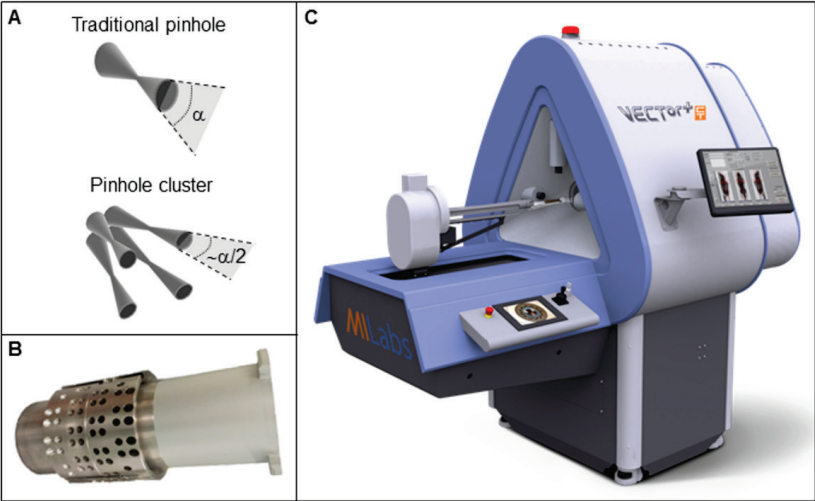


**Figure 1.** *(a) Top: pinhole with opening angle α. Bottom: cluster of four pinholes with approximately same field-of-view and pinhole opening angles of approximately α/2. (b) CMP collimator optimized for SPECT-PET imaging of rats. (c) VECTor[+]/CT system. VECTor[+] is a second-generation VECTor system.*

## *4.2 Materials and methods*

### 4.2.1 Pinhole geometry

The detector geometry and scanner design of VECTor are based on the U-SPECT system (MILabs B.V. Utrecht, The Netherlands). In this work we used a second-generation VECTor system, called VECTor[+] (Fig. 1c). Compared to VECTor, VECTor[+] applies additional reconstruction techniques to correct for DOI effects and various collimator-specific effects. Since these improvements are software-based, first-generation VECTor systems can be upgraded to VECTor[+] systems. For simplicity, we will only refer to the VECTor[+] system in the rest of this paper. The tungsten CMP rat collimator that is presented in this work has 48 clusters of four pinholes (ø 1.8 mm) placed in four rings (Fig. 1b). However, not all clusters contained four pinholes; in some clusters pinholes were left out since they would have projected largely outside the detector surface. The collimator contained 156 pinholes in total. The pinholes in the inner two rings of the collimator have opening angles of 17°, while in the outer rings opening angles of 15° were chosen in order to achieve a more uniform covering of the detectors with pinhole projections. The collimator has an inner diameter of 98 mm, the pinhole centers are placed at a diameter of 114 mm, and the collimator has a wall thickness of 37 mm.

All the clusters together observe a FOV which extends over the entire collimator tube diameter (98 mm). The central FOV (CFOV) is the area that is observed by all clusters together. The CFOV has a diameter of approximately 26 mm and a longitudinal length of approximately 20 mm. Within the CFOV, sufficient data –which is required for image reconstruction- is readily obtained without any translation of the bed. Larger areas can be scanned by stepping the animal-bed through the collimator [24, 25].

### 4.2.2 System calibration and image reconstruction

The system matrices for SPECT and PET tracers, which contain energy-specific models of photon transport from the source to the detectors (which are required for iterative image reconstruction), were calculated using a ray tracing code [26]. Inputs to this code were energy-specific photon attenuation coefficients of the collimator and detector materials and the positions and orientations of the pinholes and detectors. The positions and orientations of the pinholes and detectors were obtained from point-source measurements. The scanning focus method was used for data acquisition [24] in combination with a spiral bed-positioning protocol [25]. Pixel-based Ordered Subsets Expectation Maximization (POSEM; [27]) with 32 subsets was used for image reconstruction.

### 4.2.3 Scatter correction

In all experiments, scatter was corrected for by a triple-energy-window technique [28] and scatter was incorporated in the image reconstruction algorithm as described by Bowsher *et al.* [29]. All photopeak windows were set to a width of 15%. A background window was set adjacent to each side of the photopeak window. For $^{18}$F, the width of each background window was 30% of the width of the photopeak window. For $^{99m}$Tc and $^{123}$I, the width of each background window was 50% of the width of the photopeak window.

### 4.2.4 Evaluation of system characteristics

#### 4.2.4.1 Resolution for SPECT and PET tracers

To test the resolution of VECTor$^+$ for the new CMP rat collimator for the most common SPECT and PET isotopes ($^{99m}$Tc and $^{18}$F), a miniature resolution phantom ("Jaszczak" phantom) with 6 sectors was scanned. Each sector contains a set of equally sized capillaries with diameters of 1.7 mm (3 rods), 1.5 mm (3 rods), 1.3 mm (3 rods), 1.1 mm (3 rods), 0.95 mm (6 rods), and 0.85 mm (6 rods). The distance between the centers of neighboring capillaries within a sector equaled twice the diameter of the capillaries. Two 60-min scans were acquired, in one scan the phantom contained 59 MBq $^{99m}$Tc, in the other scan the phantom contained 31 MBq $^{18}$F.

#### 4.2.4.2 Sensitivity

Two small point sources were made by enclosing 6 μL $^{99m}$Tc solution and 6 μL $^{18}$F solution in separate small cylinders. Peak sensitivities of the system for $^{99m}$Tc and $^{18}$F were subsequently determined by positioning one of the sources in the center of the collimator. Sensitivity was defined as the ratio of the number of detected gamma photons to the number of (positron or gamma) emissions. Sensitivity was determined for photopeak windows with widths of 30%, 25%, 20% and 15%.

### 4.2.5 Animal studies

Animal studies were carried out in accordance with the Dutch Law on Animal Experimentation and conducted according to protocols approved by the Animal Research Committee of the University Medical Center Utrecht. All animals were anesthetized with isoflurane. For all scans radiotracers were administered via injection in the tail vein, except for the cardiac scan, for which radiotracers were administered via a catheter in the penal vein.

### 4.2.5.1 Rat cardiac scan

A 330 g male Wistar rat was anesthetized and an intravenous catheter was inserted in the penal vein. A mix of 419 MBq $^{99m}$Tc-sestamibi and 98 MBq $^{18}$F-deoxyglucose ($^{18}$F-FDG) was administered and a 70-minute SPECT-PET acquisition focused on the heart began just before injection. The rat was scanned in frames of 20 s.

### 4.2.5.2 Rat brain scan

A 310 g male Wistar rat, which had been kept fasting for 12 hours, was injected with 33 MBq $^{123}$I-FP-CIT and 58 MBq $^{18}$F-FDG. It was anesthetized 45 minutes after injection of the radiotracer. A 60-minute scan was made, starting 105 minutes post injection.

### 4.2.5.3 Rat bone scans

A 350 g male Wistar rat was anesthetized and injected with 75 MBq $^{99m}$Tc-methylenediphosphonate ($^{99m}$Tc-MDP) and 44 MBq $^{18}$F-fluoride. A 60-minute whole-body SPECT-PET acquisition was performed, starting 30 minutes post injection.

A 350 g male Wistar rat was anesthetized and injected with 288 MBq $^{99m}$Tc-MDP and 96 MBq $^{18}$F-fluoride. A 60-minute SPECT-PET acquisition of the lumbar spine and the pelvis was performed, starting 30 minutes post injection.

## 4.3 Results

### 4.3.1 Evaluation of system characteristics

#### 4.3.1.1 Resolution for SPECT and PET tracers

SPECT and PET images of the resolution phantom filled with either $^{99m}$Tc or $^{18}$F are shown in Fig. 2. Rods of 1.1 mm could be clearly distinguished in the $^{99m}$Tc image. For $^{18}$F, 1.3 mm rods were clearly visible for $^{18}$F, which indicates a competitive spatial resolution compared to commercially available preclinical coincidence PET systems.

#### 4.3.1.2 Sensitivity

The peak sensitivity of the system for $^{99m}$Tc and $^{18}$F for different photopeak window widths is provided in Table 1. For a photopeak window width of 30%, $^{99m}$Tc and $^{18}$F peak sensitivities were 0.48% and 0.28% respectively. Sensitivity differed only slightly for photopeak windows of 25%, 20% and 15%.

These results indicate that for ^{99m}Tc, the CMP rat collimator reaches a higher sensitivity but a lower resolution compared to U-SPECT's general-purpose rat SPECT collimator which employs less pinholes with smaller apertures (ø 1.0 mm) [8]. For ^{18}F, the peak sensitivity of the CMP rat collimator is comparable to the peak sensitivity of the CMP mouse collimator [22]. However, image resolution for ^{18}F that is reached by the CMP rat collimator is lower, which can be attributed to lower pinhole magnification factors and larger pinhole apertures.
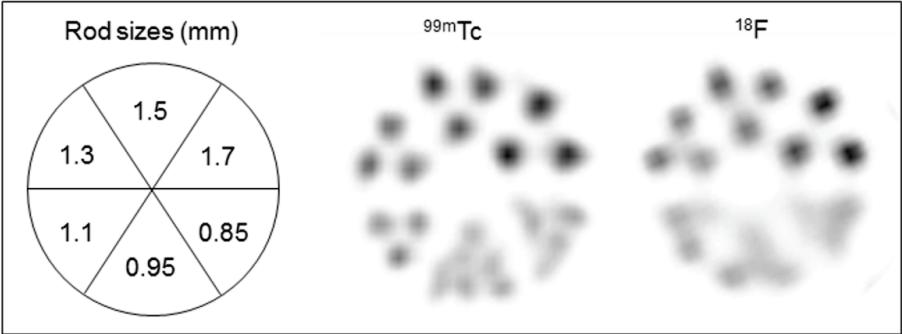


**Figure 2.** *Image slices (thickness 3.6 mm) through reconstructions of a 60-min SPECT scan (59 MBq ^{99m}Tc) and a 60min-PET scan (31 MBq ^{18}F) of a phantom with 6 segments with capillary diameters of 1.7, 1.5, 1.3, 1.1, 0.95 and 0.85 mm.*

TABLE I. Measured peak sensitivity for ^{99m}Tc and [18]F

| Photopeak window width | Sensitivity [99m]Tc | Sensitivity [18]F |
|---|---|---|
| 30% | 0.48% | 0.28% |
| 25% | 0.48% | 0.27% |
| 20% | 0.47% | 0.26% |
| 15% | 0.44% | 0.25% |

## 4.3.2 Simultaneous SPECT-PET imaging in living rats

To demonstrate the *in vivo* capabilities of VECTor[+] equipped with the new CMP rat collimator, simultaneously acquired SPECT-PET scans were performed. Similar tracer combinations as in [22] were used as these tracer combinations were selected with biological applications in mind that require the ability to directly correlate different biological functions.

### 4.3.2.1 Rat cardiac scan

[99m]Tc-sestamibi is a myocardial perfusion agent that is indicated for detecting coronary artery disease by identifying myocardial ischemia (reversible defects) and infarction (non-reversible defects). ^{18}F-FDG is used to distinguish viable myocardial tissue from non-

viable myocardial tissue in patients with coronary artery disease. The ability to measure both perfusion and viability of the myocardium in the same subject enables to distinguish between scarred and viable myocardium [30]. Moreover, the ability to acquire dynamic cardiac data could provide exact tracer kinetics which would be informative in studies where there is a mismatch between metabolism and perfusion in the myocardium [31].

For both tracers, images of the final hour of the 70-min scan were reconstructed. Figure 3a shows perpendicular slices through these images. Furthermore, from these images a volume-of-interest (VOI) for the heart was selected for each tracer. These VOIs were used to measure the activity of each tracer in the heart in the images reconstructed from the separate 20s-frames of the first hour after injection. The corresponding time-activity-curves for $^{99m}$Tc-sestamibi and $^{18}$F-FDG are presented in Figure 3b.
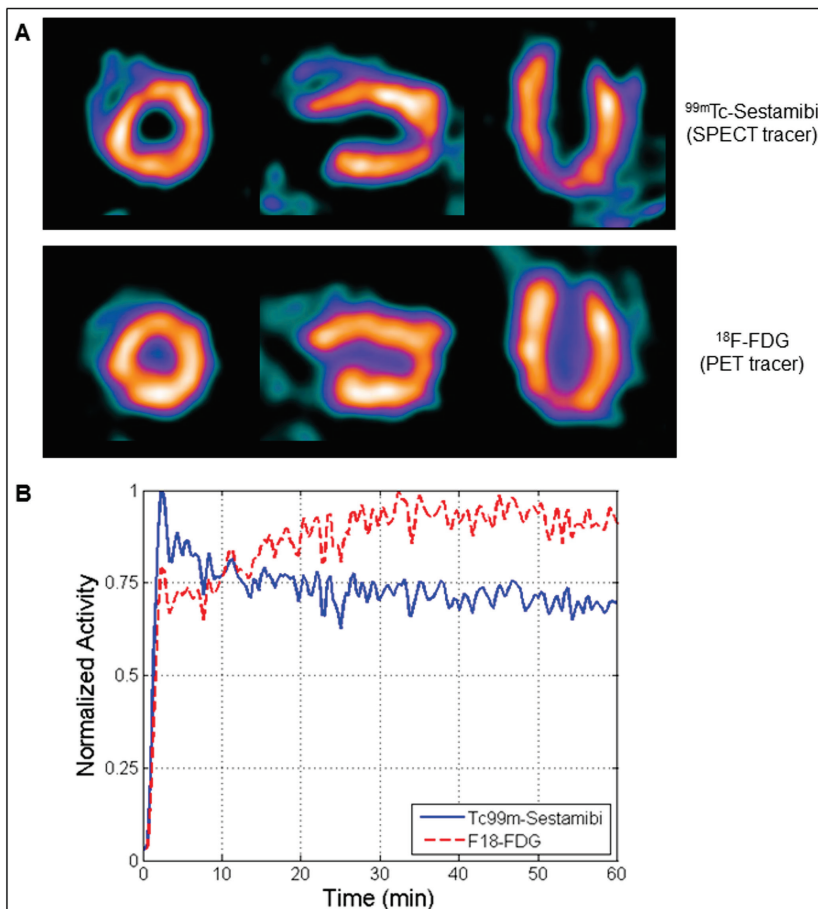


**Figure 3.** *Simultaneous SPECT-PET cardiac scan. The rat was injected with 419 MBq $^{99m}$Tc-sestamibi and 98 MBq $^{18}$F-FDG and scanned for 70 min. (a) Perpendicular slices through the rat-heart images reconstructed from the final 60 min of the scan. (b) Time-activity-curves of $^{99m}$Tc-sestamibi and $^{18}$F-FDG measured inside a volume-of-interest centered on the heart.*

### 4.3.2.2 Rat brain scan

A simultaneously acquired SPECT-PET brain scan was performed, combining a probe for dopamine transporters (^{123}I-FP-CIT; SPECT tracer) and a glucose analogue (^{18}F-FDG; PET tracer). In this example, simultaneous SPECT-PET imaging may enable to directly relate the binding location of a drug of abuse that blocks dopamine transport, like cocaine [32], to changes in metabolic brain activity, for which ^{18}F-FDG is indicated as a marker [33]. Figure 4 shows specific binding of ^{123}I-FP-CIT to dopamine transporters and uptake of ^{18}F-FDG in small substructures of the brain (indicated by arrows).
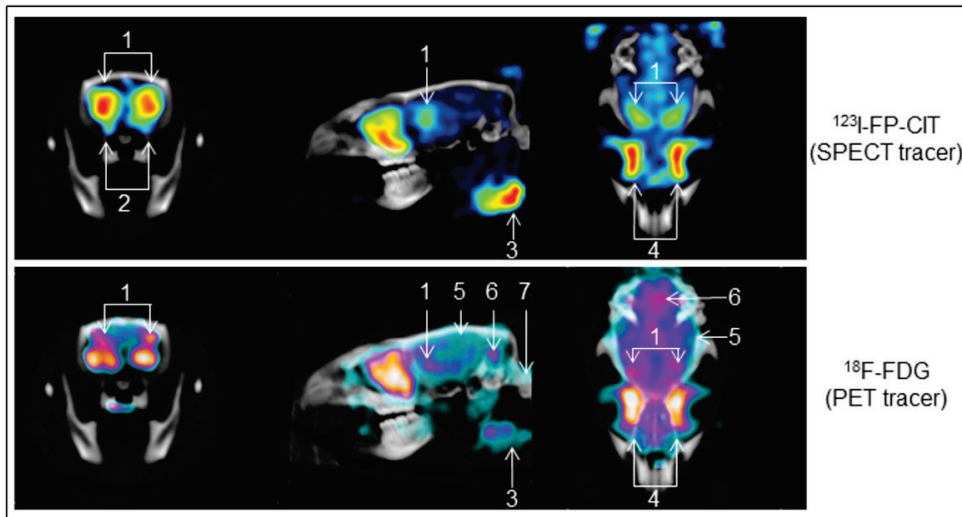


**Figure 4.** *Simultaneously acquired SPECT (top) and PET (bottom) images of the rat-brain registered with a CT image. Rat was injected with a mix of 33 MBq ^{123}I-FP-CIT and 58 MBq ^{18}F-FDG and imaged for 60 min starting 105 min after injection. From left to right, transversal, sagittal and coronal slices are shown. Uptake of ^{123}I-FP-CIT and ^{18}F-FDG in small brain structures such as striatum (1), olfactory tubercle (2) and Harderian glands (4). ^{18}F-FDG uptake is also seen in cerebral cortex (5), cerebellum (6) and spinal cord (7). Sagittal images show ^{123}I-FP-CIT and ^{18}F-FDG uptake in thyroid (3).*

### 4.3.2.3 Rat bone scans

Finally, rat bone-scans were performed to illustrate a SPECT and a PET tracer that target the same biological function under exactly the same physiological conditions. Two 60-min scans were performed and for each scan a rat was injected with a mix of ^{99m}Tc-MDP and ^{18}F-fluoride. One scan was a total-body scan, the other a focused scan of the lumbar-spine and pelvis. Figure 5 shows coronal maximum-intensity-projections of SPECT and PET reconstructions of the total-body scan. In Fig. 6 coronal and sagittal MIPs of the focused bone-scan are provided. From these images it is clear that in the SPECT images small structures are better resolved than in the PET images: e.g. in Fig. 5 individual ribs can be

better distinguished in the SPECT image and in Fig. 6 the processes of the vertebrae are better resolved in the SPECT image. This observation is in line with the resolution phantom images which showed a higher resolution for SPECT than for PET tracers.
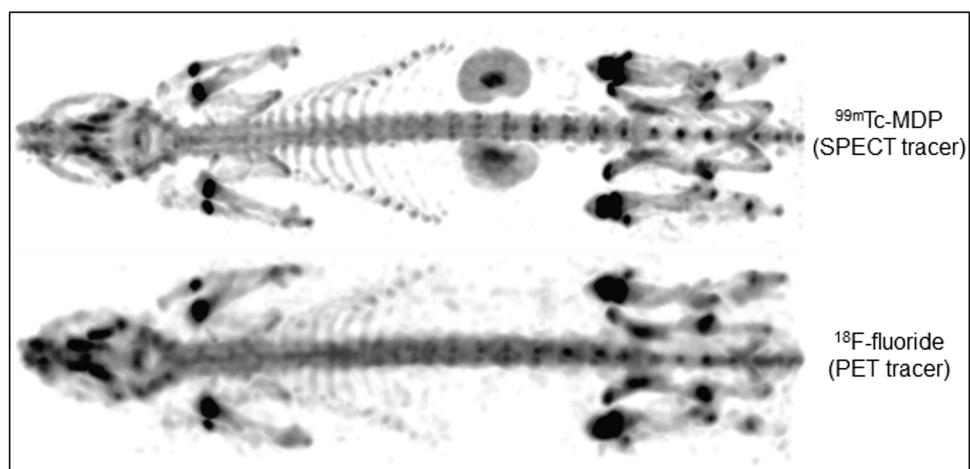


**Figure 5.** *Example of simultaneous SPECT-PET scan (60 min) of two bone tracers: Maximum-intensity-projections of rat injected with 75 MBq $^{99m}$Tc-MDP (top) and 44 MBq $^{18}$F-fluoride (bottom).*
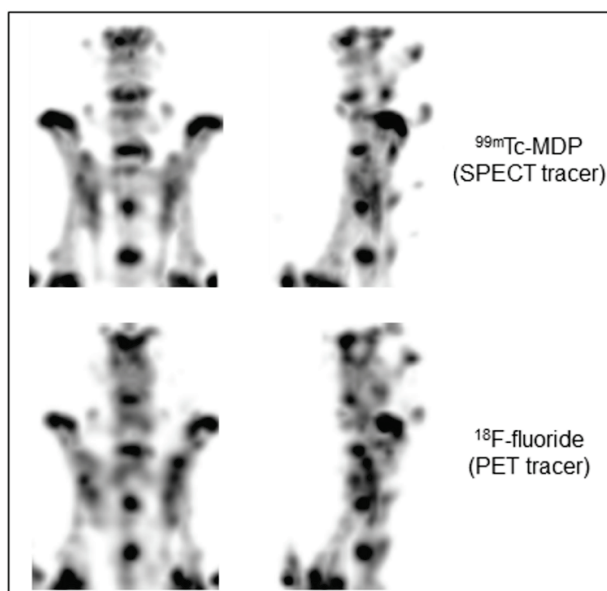


**Figure 6.** *MIPs of simultaneous SPECT-PET bone-scan of lumbar spine and pelvis. The rat was injected with 288 MBq $^{99m}$Tc-MDP (top) and 96 MBq $^{18}$F-fluoride (bottom) and was scanned for 60 min.*

## 4.4 Discussion

In this work we have demonstrated that VECTor[+] now also enables simultaneous SPECT-PET imaging of rats. Furthermore, we have shown that fast dynamic simultaneous SPECT-PET imaging is possible. The ability to scan fast may be necessary for tracer kinetic modeling studies of rapidly changing biological processes. The dynamic focused cardiac scan in this work was acquired using a spiral bed-positioning sequence and had a temporal resolution of 20 s. The use of spiral bed-positioning sequences has been shown to enable sub-min temporal resolutions for scanning larger areas of a mouse up to the whole body when using a general-purpose mouse collimator [25]. A similar temporal resolution may be reached for a dynamic total-body rat scan since the dimensions of the FOV of a rat collimator compared to a mouse collimator scale with the larger size of a rat compared to a mouse. Even higher temporal resolutions can be expected for total-body mouse SPECT-PET with the novel CMP rat collimator since the large FOV will only require a few positions of the animal-bed in the collimator. Moreover, sub-half-minute dynamic total-body mouse SPECT has already been demonstrated for U-SPECT when using a SPECT collimator for rat-sized animals [34].

The VECTor[+] system that was used in this work employed 9 mm-thick NaI detector crystals that are optimized for imaging SPECT tracers. However, at this thickness, the detectors only have an intrinsic photopeak detection efficiency of about 10% for 511 keV annihilation photons resulting from PET tracer decay. A strong increase in detection efficiency could be attained by using thicker crystals [22]. This would allow to decrease PET imaging times or allow for smaller pinholes -and therefore a higher spatial resolution- without a decrease in PET sensitivity compared to the current system. This will certainly be a topic of future investigations.

Compared to SPECT and PET scanners in a tandem configuration or to stand-alone SPECT and PET scanners, a fully integrated approach to SPECT-PET imaging may offer cost saving, a reduced scanner footprint, reduced imaging times and the ability to perform SPECT and PET scans with a single dose of anesthesia. Moreover, since VECTor[+] is based on the existing U-SPECT platform, any existing U-SPECT system can relatively easily be converted to a VECTor[+] system.

## 4.5 Conclusions

In this work we have demonstrated that VECTor[+], next to simultaneous SPECT-PET imaging of mice, also enables simultaneous (dynamic) SPECT-PET imaging of rats. With VECTor[+], scientists can select the most suitable combinations of radiotracers from the entire complement of available SPECT and PET tracers depending on the imaging task. The acquired images are inherently spatially and temporally registered which makes it possible to study the correlation between different biological functions in the same animal at the same time with a single dose of anesthesia.

**Acknowledgements**

## *Bibliography*

[1]     D. J. Rowland, and S. R. Cherry, "Small-animal preclinical nuclear medicine instrumentation and methodology," *Semin. Nucl. Med.,* vol. 38, no. 3, pp. 209-22, 2008.

[2]     R. Weissleder, B. D. Ross, A. Rehemtulla, and S. S. Gambhir, *Molecular Imaging : Principles and Practice*, p.^pp. 844-1178, Shelton, Conn.: People's Medical Pub. House-USA, 2010.

[3]     L. R. Furenlid, D. W. Wilson, Y. C. Chen, H. Kim, P. J. Pietraski, M. J. Crawford, and H. H. Barrett, "FastSPECT II: A Second-Generation High-Resolution Dynamic SPECT Imager," *IEEE Trans. Nucl. Sci.,* vol. 51, no. 3, pp. 631-635, 2004.

[4]     K. Ishizu, T. Mukai, Y. Yonekura, M. Pagani, T. Fujita, Y. Magata, S. Nishizawa, N. Tamaki, H. Shibasaki, and J. Konishi, "Ultra-high-resolution spect system using 4 pinhole collimators for small animal studies," *J. Nucl. Med.,* vol. 36, no. 12, pp. 2282-2287, 1995.

[5]     R. J. Jaszczak, J. Y. Li, H. L. Wang, M. R. Zalutsky, and R. E. Coleman, "Pinhole collimation for ultra-high-resolution, small-field-of-view spect," *Phys. Med. Biol.,* vol. 39, no. 3, pp. 425-437, 1994.

[6]     Z. L. Liu, G. A. Kastis, G. D. Stevenson, H. H. Barrett, L. R. Furenlid, M. A. Kupinski, D. D. Patton, and D. W. Wilson, "Quantitative analysis of acute myocardial infarct in rat hearts with ischemia-reperfusion using a high-resolution stationary SPECT system," *J. Nucl. Med.,* vol. 43, no. 7, pp. 933-939, 2002.

[7]     S. D. Metzler, R. J. Jaszczak, N. H. Patil, S. Vemulapalli, G. Akabani, and B. B. Chin, "Molecular imaging of small animals with a triple-head SPECT system using pinhole collimation," *IEEE Trans. Med. Imag.,* vol. 24, no. 7, pp. 853-862, 2005.

[8]     F. Van der Have, B. Vastenhouw, R. M. Ramakers, W. Branderhorst, J. O. Krah, C. Ji, S. G. Staelens, and F. J. Beekman, "U-SPECT-II: An Ultra-High-Resolution Device for Molecular Small-Animal Imaging," *J. Nucl. Med.,* vol. 50, no. 4, pp. 599-605, 2009.

[9]     F. Van der Have, B. Vastenhouw, M. Rentmeester, and F. J. Beekman, "System calibration and statistical image reconstruction for ultra-high resolution stationary pinhole SPECT," *IEEE Trans. Med. Imag.,* vol. 27, no. 7, pp. 960-71, 2008.

[10]    A. P. Jeavons, R. A. Chandler, and C. A. R. Dettmar, "A 3D HIDAC-PET camera with sub-millimetre resolution for imaging small animals," *IEEE Trans. Nucl. Sci.,* vol. 46, no. 3, pp. 468-473, 1999.

[11]    R. S. Miyaoka, M. L. Janes, K. Lee, B. Park, P. E. Kinahan, and T. K. Lewellen, "Development of a single detector ring micro crystal element scanner: QuickPET II," *Mol. Imaging,* vol. 4, no. 2, pp. 117-27, 2005.

[12]    N. C. Rouze, M. Schmand, S. Siegel, and G. D. Hutchins, "Design of a small animal PET imaging system with 1 microliter volume resolution," *IEEE Trans. Nucl. Sci.,* vol. 51, no. 3, pp. 757-763, 2004.

[13]    Y. C. Tai, A. F. Chatziioannou, Y. F. Yang, R. W. Silverman, K. Meadors, S. Siegel, D. F. Newport, J. R. Stickel, and S. R. Cherry, "MicroPET II: design, development and initial performance of an improved microPET scanner for small-animal imaging," *Phys. Med. Biol.,* vol. 48, no. 11, pp. 1519-1537, 2003.

[14]    Y. C. Tai, A. Ruangma, D. Rowland, S. Siegel, D. F. Newport, P. L. Chow, and R. Laforest, "Performance evaluation of the microPET focus: a third-generation microPET scanner dedicated to animal imaging," *J. Nucl. Med.,* vol. 46, no. 3, pp. 455-63, 2005.

[15]   Y. F. Yang, Y. C. Tai, S. Siegel, D. F. Newport, B. Bai, Q. Z. Li, R. M. Leahy, and S. R. Cherry, "Optimization and performance evaluation of the microPET II scanner for in vivo small-animal imaging," *Phys. Med. Biol.,* vol. 49, no. 12, pp. 2527-2545, 2004.

[16]   K. Magota, N. Kubo, Y. Kuge, K. Nishijima, S. Zhao, and N. Tamaki, "Performance characterization of the Inveon preclinical small-animal PET/SPECT/CT system for multimodality imaging," *Eur. J. Nucl. Med. Mol. Imaging,* vol. 38, no. 4, pp. 742-52, 2011.

[17]   F. Sanchez, A. Orero, A. Soriano, C. Correcher, P. Conde, A. Gonzalez, L. Hernandez, L. Moliner, M. J. Rodriguez-Alvarez, L. F. Vidal, J. M. Benlloch, S. E. Chapman, and W. M. Leevy, "ALBIRA: a small animal PETSPECTCT imaging system," *Med. Phys.,* vol. 40, no. 5, pp. 051906, 2013.

[18]   S. C. Huang, R. E. Carson, E. J. Hoffman, D. E. Kuhl, and M. E. Phelps, "An Investigation of a Double-Tracer Technique for Positron Computerized-Tomography," *J. Nucl. Med.,* vol. 23, no. 9, pp. 816-822, 1982.

[19]   D. J. Kadrmas, and J. M. Hoffman, "Methodology for Quantitative Rapid Multi-Tracer PET Tumor Characterizations," *Theranostics,* vol. 3, no. 10, pp. 757-773, 2013.

[20]   D. J. Kadrmas, and T. C. Rust, "Feasibility of rapid multitracer PET tumor imaging," *IEEE Trans. Nucl. Sci.,* vol. 52, no. 5, pp. 1341-1347, 2005.

[21]   R. A. Koeppe, E. P. Ficaro, D. M. Raffel, S. Minoshima, and M. R. Kilbourn, "Temporally overlapping dual-tracer PET studies," *Quantitative Functional Brain Imaging with Positron Emission Tomography*, pp. 359-366, 1998.

[22]   M. C. Goorden, F. van der Have, R. Kreuger, R. M. Ramakers, B. Vastenhouw, J. P. Burbach, J. Booij, C. F. Molthoff, and F. J. Beekman, "VECTor: a preclinical imaging system for simultaneous submillimeter SPECT and PET," *J. Nucl. Med.,* vol. 54, no. 2, pp. 306-12, 2013.

[23]   M. C. Goorden, and F. J. Beekman, "High-resolution tomography of positron emitters with clustered pinhole SPECT," *Phys. Med. Biol.,* vol. 55, no. 5, pp. 1265-77, 2010.

[24]   B. Vastenhouw, and F. Beekman, "Submillimeter total-body murine imaging with U-SPECT-I," *J. Nucl. Med.,* vol. 48, no. 3, pp. 487-93, 2007.

[25]   P. E. B. Vaissier, M. C. Goorden, B. Vastenhouw, F. van der Have, R. M. Ramakers, and F. J. Beekman, "Fast spiral SPECT with stationary gamma-cameras and focusing pinholes," *J. Nucl. Med.,* vol. 53, no. 8, pp. 1292-9, 2012.

[26]   M. C. Goorden, F. Van der Have, R. Kreuger, and F. J. Beekman, "An efficient simulator for pinhole imaging of PET isotopes," *Phys. Med. Biol.,* vol. 56, no. 6, pp. 1617-34, 2011.

[27]   W. Branderhorst, B. Vastenhouw, and F. J. Beekman, "Pixel-based subsets for rapid multi-pinhole SPECT reconstruction," *Phys. Med. Biol.,* vol. 55, no. 7, pp. 2023-34, 2010.

[28]   K. Ogawa, Y. Harata, T. Ichihara, A. Kubo, and S. Hashimoto, "A practical method for position-dependent Compton-scatter correction in single photon emission CT," *IEEE Trans. Med. Imag.,* vol. 10, no. 3, pp. 408-12, 1991.

[29]   J. E. Bowsher, V. E. Johnson, T. G. Turkington, R. J. Jaszczak, C. R. Floyd, and R. E. Coleman, "Bayesian reconstruction and use of anatomical a priori information for emission tomography," *IEEE Trans. Med. Imag.,* vol. 15, no. 5, pp. 673-86, 1996.

[30]   D. Delbeke, S. Videlefsky, J. A. Patton, M. G. Campbell, W. H. Martin, I. Ohana, and M. P. Sandler, "Rest myocardial perfusion/metabolism imaging using simultaneous dual-isotope acquisition spect with technetium-99m-mibi/fluorine-18-fdg," *J. Nucl. Med.,* vol. 36, no. 11, pp. 2110-2119, 1995.

[31]   H. Iida, T. Hayashi, S. Eberl, and H. Saji, "Quantification in SPECT cardiac imaging," *J. Nucl. Med.,* vol. 44, no. 1, pp. 40-42, 2003.

[32]   B. Vastenhouw, F. van der Have, A. J. van der Linden, L. von Oerthel, J. Booij, J. P. Burbach, M. P. Smidt, and F. J. Beekman, "Movies of dopamine transporter occupancy with ultra-high resolution focusing pinhole SPECT," *Mol. Psychiatry,* vol. 12, no. 11, pp. 984-7, 2007.

[33]   E. M. Reiman, A. Uecker, F. Gonzalez-Lima, D. Minear, K. W. Chen, N. L. Callaway, J. D. Berndt, and D. Games, "Tracking Alzheimer's disease in transgenic mice using fluorodeoxyglucose autoradiography," *Neuroreport,* vol. 11, no. 5, pp. 987-991, 2000.

[34]   R. M. Ramakers, B. Vastenhouw, P. E. B. Vaissier, and F. J. Beekman, "Whole-body sub-half-minute 4D pharmacokinetic SPECT in mice," *J. Nucl. Med. meeting abstracts,* vol. 54, no. 2, pp. 264, 2013.

# 5. Influence of respiratory gating, image filtering and animal positioning on high-resolution ECG-gated murine cardiac SPECT

C. Wu, P. E. B. Vaissier, B. Vastenhouw, J. R. de Jong, R. H. J. A. Slart, and F. J. Beekman. "Influence of respiratory gating, image filtering and animal positioning on high-resolution ECG-gated murine cardiac SPECT," Submitted to *Mol. Imaging*, 2014.

## *Abstract*

Cardiac parameters obtained from SPECT images can be affected by respiratory motion, image filtering and animal positioning. Here we investigate the influence of these factors on ultra-high-resolution murine myocardial perfusion SPECT. Five mice were injected with $^{99m}$Tc-tetrofosmin and each was scanned in supine and prone positions in a U-SPECT-II scanner with respiratory and ECG gating. ECG-gated SPECT images were created without applying respiratory-motion correction, or with two different respiratory-motion correction strategies. The images were filtered with a range of 3D Gaussian kernels after which end-diastolic volumes (EDVs), end-systolic volumes (ESVs), and left ventricular ejection fractions (LVEFs) were calculated. No significant differences in the measured cardiac parameters were detected when any strategy to reduce or correct for respiratory motion was applied, while big differences (> 5%) in EDV and ESV were found with regard to different positioning of animals. A linear relationship (p < 0.001) was found between the EDV or ESV and the kernel size of the Gaussian filter. In short, respiratory gating did not significantly affect cardiac parameters of mice obtained with ultra-high-resolution SPECT, while the position of the animals and the image filters should be the same in a comparative study with multiple scans to avoid systematic differences in measured cardiac parameters.

## 5.1 Introduction

In addition to tissue properties of the myocardium such as perfusion or viability, ECG-gated cardiac single-photon emission computed tomography (SPECT) can provide quantitative information about ventricular volumes, ventricular ejection fractions as well as myocardial wall-motion and thickness [1-4]. In such studies, image quality can degrade due to respiratory motion. Respiratory gating has been applied in tomography studies too, e.g. for imaging lung areas [5, 6]. It involves rebinning of the projection data into respiratory gates that represent different breathing phases. As the position and orientation of the heart are also affected by respiratory motion, it is prudent to investigate whether respiratory gating may also reduce image blur in cardiac imaging and improve cardiac imaging quality. As early as 1998, the scheme for simultaneous ECG and respiratory gating ("dual gating") and an algorithm for respiratory-motion compensation were already developed and tested with phantoms for clinical positron emission tomography (PET) [7]. It was found that the magnitude of the motion induced by respiration is close to the myocardial wall thickness [8, 9]. As a result of this study, many clinical cardiac studies are performed with simultaneous ECG and respiratory gating to obtain better resolved myocardial walls in the reconstructed images [10, 11].

ECG gating has been evaluated for small-animal SPECT for assessing left ventricular function and has been applied in studies where new pharmaceuticals were tested [12-18]. Simultaneous ECG and respiratory gating has been assessed for a high-resolution (1 mm) micro-PET system [19]. In this study, it was found that although respiratory motion was detectable in the images, its spatial extent and duration were small, and it could therefore likely be ignored for most studies. However, whether the assessment of cardiac function in SPECT with sub-half-millimeter resolution can benefit from simultaneous ECG and respiratory gating has not yet been investigated.

Image filtering is another factor that may influence the assessment of cardiac function. Cardiac quantification software usually fits a flexible 3D model of the left ventricle to the reconstructed activity in the myocardium and calculates cardiac parameters via this model. Image filtering changes the smoothness and thickness of the reconstructed activity in the ventricular wall, which may result in changes in the fit of the 3D model to the left ventricle in the image. Therefore, image filtering may change cardiac parameters that are calculated from the fitted model. Effects of filtering have already been observed in many clinical studies [20-24]. However, no investigations into filtering effects on murine cardiac SPECT have yet been published.

The position of an animal (supine or prone) during scanning affects arterial filling, which may result in differences in the cardiac parameters that are measured. This has already been investigated in clinical studies [25-27]. In these studies, changes in the left ventricular volume were detected but no significant differences in ejection fraction were found. However, such a study has yet to be performed for small-animal cardiac SPECT. A change in animal position may also change restrictions on thoracic movement, and thus may result in different levels of heart motion due to respiration.

The aim of the research presented in this chapter is to investigate the influence of respiratory gating, post-reconstruction image filtering and mouse positioning on high-resolution ECG-gated $^{99m}$Tc-tetrofosmin myocardial perfusion SPECT.

## 5.2 Materials and methods

Animal studies were conducted following protocols approved by the Animal Research Committee of the University Medical Center Utrecht. All persons gave their informed consent prior to their inclusion in the study.

### 5.2.1 In vivo myocardial perfusion SPECT of mice

The U-SPECT-II (MILabs B.V., Utrecht, the Netherlands) [28] multi-pinhole SPECT scanner was used in the present studies. This dedicated small-animal SPECT system has stationary detectors. The highest achievable spatial resolution of this system is < 0.4 mm for $^{99m}$Tc imaging when using a general-purpose mouse collimator (as was used in the present study and recommended by the manufacturer) with 75 pinholes (⌀ 0.6 mm). The system accepts three transistor–transistor logic (TTL) trigger signals for gated studies through three Bayonet Neill–Concelman (BNC) connectors mounted on the side panel. Both trigger and photon-counting events are recorded in list mode.

Five C57-BL6/J mice (about 30 grams each) were injected via the tail vein with 200–250 MBq $^{99m}$Tc-tetrofosmin in 0.3–0.4 ml. For each mouse, two focused cardiac SPECT scans were performed, the first scan starting about 30 min post injection. The first scan lasted 60 min, while the second scan lasted 70 minutes in order to obtain approximately equal numbers of counts in both scans (i.e. to compensate for the decay of $^{99m}$Tc). For each mouse, one scan was performed with the mouse in a supine position, while the other scan was performed with the mouse in a prone position, and the position order was alternated for different mice to avoid bias caused by the order of animal positioning. A heating pad was placed between the mice and the animal bed. The mice were anesthetized with a mixture of 1.6–2.0% isoflurane in medical air (Univentor, UNO B.V., Zevenaar, the Netherlands). ECG signals were measured by using three ECG leads (Neonatal Monitoring Electrode, 3M, Maplewood, MN, USA) and the respiratory signal was measured by using a respiration sensor (Graseby Respiration Sensor, Medicare, Kilmacanogue, Ireland). Both signals were sent to an animal monitoring and gating module (BioVet, m2m Imaging, Cleveland, OH, USA). Two channels of trigger signals were produced by this device (one channel for ECG signals and one channel for respiratory signals) and these signals were sent to the U-SPECT-II system via two BNC connectors.

## 5.2.2 Image reconstruction and strategies for respiratory-motion compensation

Trigger events were recovered during list-mode data processing. A histogram of the time intervals between adjacent ECG trigger events was made for each scan and a window was set to accept only the intervals in the main peak (width: about 12%) of the histogram. This way most irregular heartbeats and spurious or missing trigger signals were rejected. The same procedure was performed for the time intervals between adjacent respiratory trigger events. Next, each accepted ECG interval was divided into eight cardiac phases, and each accepted respiratory interval was split into eight respiratory phases. This resulted in 64 combinations of cardiac and respiratory phases. Each photon count in the list-mode data was sorted into one of 64 projection data sets depending on how its time stamp located in the ECG and respiratory intervals, as is illustrated in Fig. 1.
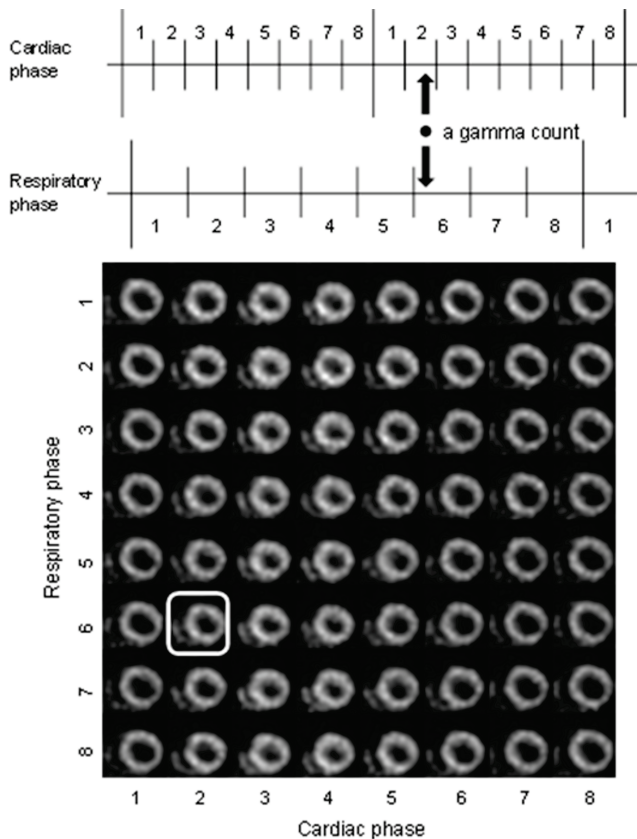


**Figure 1.** *Dual gating scheme with 8 ECG and 8 respiratory gates. A count that is e.g. in the 2nd cardiac phase and the 6th respiratory phase will be sorted into the projection data set corresponding to this combination of phases. The reconstructed image for this combination of phases is indicated by the white box.*

Images were reconstructed by a pixel-based ordered subset expectation maximization algorithm (POSEM) [29] with 16 subsets, and 6 iterations were performed. The voxel size of the reconstructions was 0.2 mm. In order to study the influence of respiratory motion, three different strategies were applied to form eight ECG-gated heart images from the 64 dual-gated images.

Firstly, the "standard strategy": images of all eight respiratory gates that were in the same cardiac phase were averaged directly. This way, the counts in all respiratory phases were used and no respiratory-motion correction was applied.

Secondly, the "motion-reduced strategy": images of $2^{nd}$ up to $7^{th}$ respiratory gates that were in the same cardiac phase were averaged directly. This strategy is based on a hypothesis that significant respiratory motion only occurs when a respiratory trigger signal is created, which was revealed in [19]. This way, counts acquired in respiratory gates that correspond to the largest respiratory motions were excluded from image formation and the resulting images may be less influenced by respiration.

Thirdly, the "motion-corrected strategy": images of all eight respiratory gates that were in the same cardiac phase were firstly registered to each other and then averaged. Details of the registration procedure are discussed in the following section.

## 5.2.3 Image registration for respiratory motion correction

Contraction and relaxation of the heart (i.e. cardiac phases) mainly change the shape of the heart, while respiratory motion primarily changes the position and orientation of the heart as the diaphragm, the chest wall and the lungs move during breathing [7]. The influence of respiratory motion on the cardiac images can therefore be corrected by using a rigid registration procedure. In principle, any dual-gated image can serve as a reference image for the registration of dual-gated images that correspond to the same cardiac phase but to different respiratory phases. However, the noise level in the 64 individual dual-gated images was relatively high, because of the relatively low number of counts with which each image was reconstructed. Therefore, we did not determine the registration parameters from these images directly, rather we calculated these parameters from eight respiratory-only-gated images: each of these images was an average of eight dual-gated images that corresponded to one respiratory phase but to different cardiac phases. The resulting image corresponding to the 5th respiratory phase served as the reference image for registration of the images corresponding to the other respiratory phases. As a result, seven transformation matrices were obtained. These transformations were then applied to the 56 dual-gated images that corresponded to the $1^{st}$–$4^{th}$ and $6^{th}$–$8^{th}$ respiratory phases.

The transformation matrices were calculated using the elastix toolbox [30]. The normalized correlation coefficient (NCC) between two images was selected as the metric for registration. To avoid influence of high activity uptake in the liver and the gall bladder on the registration procedure, a 3D elliptical mask that only covered the heart was used. This mask

was fixed to the reference image and the transformation matrices were calculated using only the voxels inside the mask region.

## 5.2.4 Image processing and analysis

All ECG-gated images that were obtained by the three strategies (standard, motion-reduced and motion-corrected) were spatially filtered with Gaussian kernels of 0.5 mm, 0.6 mm, 0.7 mm, 0.8 mm, 0.9 mm and 1.0 mm full width at half maximum (FWHM) and then filtered along temporal frames (cardiac phases) by means of a circular convolution with a [0.25, 0.5, 0.25] kernel function. We analyzed these images with the Corridor4DM software (INVIA, Ann Arbor, MI, USA) [31]. In order for the clinical Corridor4DM software to accept mouse-heart images, the voxel size of the images was changed from 0.2 mm to 2 mm. The cardiac volumes that were calculated by the software were rescaled afterwards to correspond to the original voxel size.

After importing the images into Corridor4DM, an initial manual reorientation of each image was performed to roughly align the heart's short axis (SA), vertical long axis (VLA) and horizontal long axis (HLA) with the three Cartesian axes, after which the software automatically fine-tuned the orientation using a built-in algorithm. Next, a flexible 3D left ventricle (LV) model was fitted to the LV walls in the images. The model uses gradient operators, contiguity assumptions, and weighted spline interpolators to detect and refine the LV endocardial and epicardial surfaces [31]. Using this model, the LV volume (LVV) in each cardiac phase was calculated and the maximum and minimum LVVs of all cardiac phases were respectively defined to be the end-diastolic volume (EDV) and end-systolic volume (ESV). The left ventricular ejection fraction (LVEF) was also provided by the software.

In addition to cardiac parameters, images were directly compared by generating line profiles along different positions and directions in the images. To this end, an extra rigid registration was applied between the images.

## *5.3 Results*

### 5.3.1 Respiratory motion and image profiles

The transformation matrices that were obtained with the motion-corrected strategy revealed that the largest heart motion (about 1 mm translation) occurred in the 8th respiratory phase in which the respiratory trigger signal was created. The second largest heart motion (about 0.4 mm) occurred in the 1st phase, while the heart motions in the rest of the respiratory phases were generally less than 0.2 mm (Fig. 2), which is smaller than the highest resolution that the imaging system can achieve (about 0.35 mm). This finding is consistent with the hypothesis that significant respiratory motion only occurs when a respiratory trigger signal is created, which is the justification for the motion-reduced strategy (i.e. only using the 2nd up to the 7th respiratory gate). Taking Mouse 2 and 5 as an example, almost no visual differences were found between the cardiac image slices and profiles corresponding to the three motion correction strategies (Fig. 3).
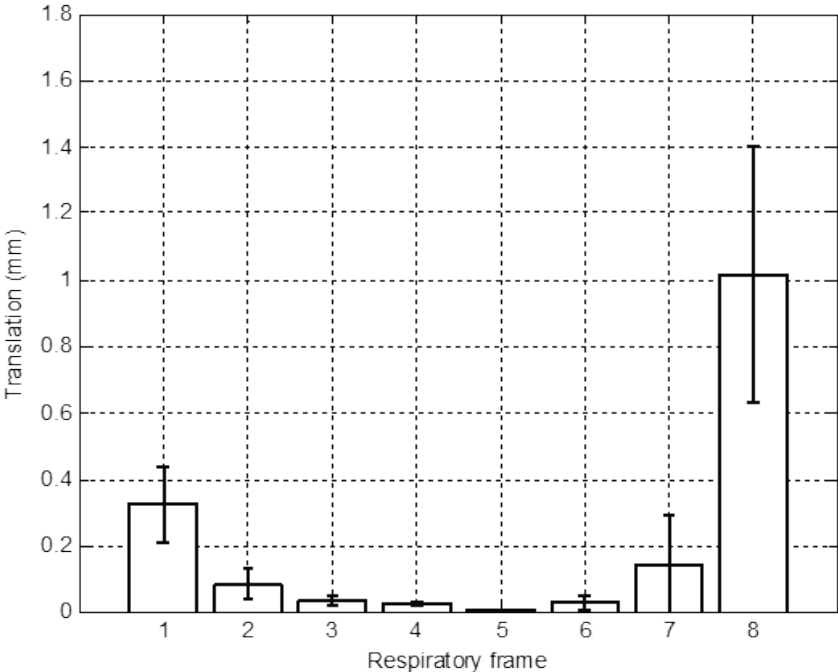


**Figure 2.** *Respiratory heart translations that were calculated by the rigid registration procedure in the motion-corrected strategy. Relatively large translations were found only in the 1st and 8th frames (average over all scans).*
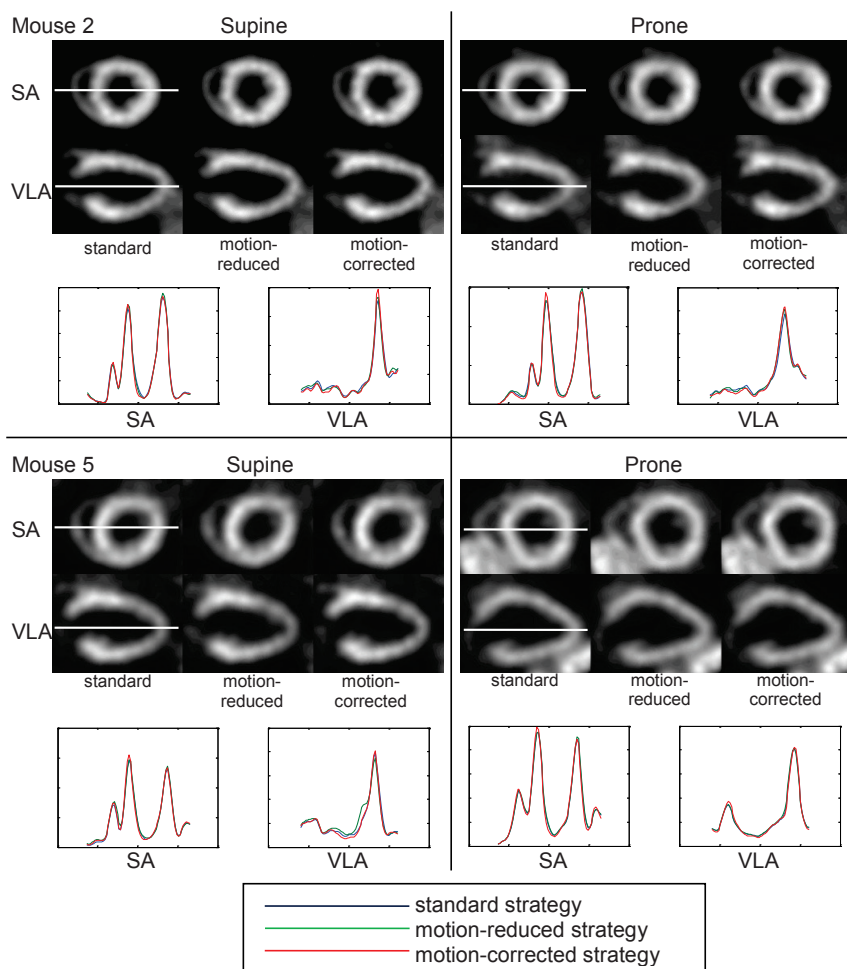
**Figure 3.** *SA and VLA slices and line profiles of Mouse 2 and Mouse 5 in supine and prone positions at ED. Images are filtered with a Gaussian kernel (0.7 mm FWHM).*

### 5.3.2 Cardiac parameters

The 180 ECG-gated heart images, resulting from all combinations between the five mice, the two positions, the three respiratory-motion correction strategies and the six Gaussian filter kernels, were analyzed by the Corridor4DM software. The resulting cardiac parameters are listed in Table 1 (all tables can be found at the end of this chapter, before the bibliography section). The EDV, ESV and LVEF obtained from the images that were formed by the "standard strategy" and that were filtered with a 0.7 mm FWHM kernel were respectively 50±11 µl, 22±8 µl and 0.57±0.07 (average over the ten scans). The mean values corresponding to this strategy and filter kernel served as reference values for comparing

cardiac parameters obtained by other combinations of motion correction strategies and filter kernels. Note that in this work the values of LVEF are expressed as decimal fractions to distinguish them from the relative changes in LVEF which are expressed as percentages.

The 180 ECG-gated heart images were separated into 36 different groups, each group corresponding to a combination of one of the three motion correction strategies, one of the two animal positions and one of the six filter kernels (each group contained reconstructions of five mouse scans). The average EDVs, ESVs and LVEFs were calculated for each group. The results are plotted in Fig. 4. This figure clearly shows that there were only slight changes in cardiac parameters induced by the different motion correction strategies.
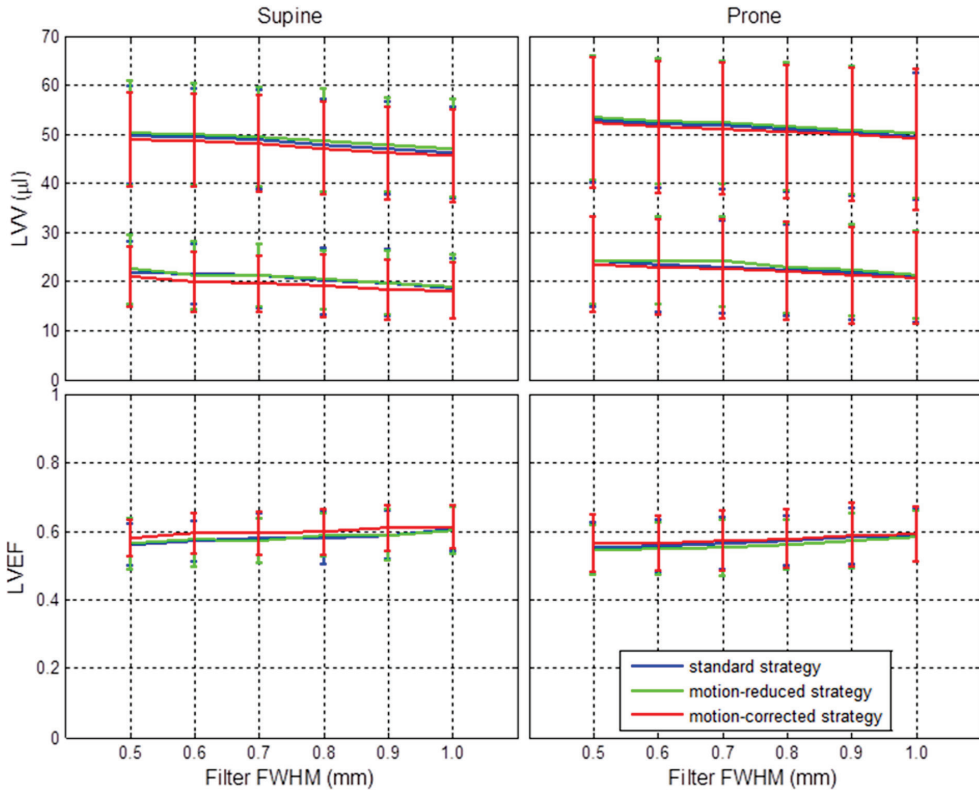


**Figure 4.** *Effects of positioning, motion correction strategy and Gaussian filter size on left ventricular EDVs, ESVs and LVEFs (average over all scans).*

In order to investigate the effects of image filtering, animal positioning and motion correction strategies on the measured cardiac parameters, we performed linear regression analyses on the 180 images (i.e. observations). The variables are listed in Table 2. The variable *prone* is a categorical dummy for animal positioning, and *mr* and *mc* are categorical dummies for respiratory-motion correction strategies. The supine position and the "standard strategy" were the reference categories in the regression. We also created categorical dummies *m2* to *m5* to represent individual differences between the mice. We omitted any

interaction terms between the variable *filter* and the categorical dummies mentioned above, because effects of image filtering should have no correlation with possible effects induced by the other variables. Therefore the dummies contributed only in the intercepts of the regression. The linear regression model is represented by:

$$dep_i = \beta_0 + \beta_1 filter_i + \beta_2 prone_i + \beta_3 mr_i + \beta_4 mc_i + \beta_5 m2_i + \beta_6 m3_i + \beta_7 m4_i + \beta_8 m5_i + \varepsilon_i \quad (1)$$

in which *i* denotes the index of observations, and *dep* represents the dependent variables (i.e. *edv*, *esv* or *lvef*) in the three regressions. The estimates of the ordinary-least-squares estimators (by Stata, StataCorp, College Station, TX, USA) are listed in Table 3.

The coefficient of determination ($R^2$) of each regression was larger than 0.85, which means that the data points fit the regression model quite well. Before any causal interpretations of the results are made, the statistical significance of the estimates at a 5% significance level is examined. Only if an estimated coefficient is statistically significant, one can state that the effect of the corresponding parameter does exist. In this study, we found strong evidence that filtering and animal positioning have influence on EDV, ESV and LVEF, since the p-values for the estimated coefficients for *filter* ($\hat{\beta}_1$) and *prone* ($\hat{\beta}_2$) were 0.00 ($< 0.05$) for all regressions. However, the p-values for the estimated coefficients for *mr* ($\hat{\beta}_3$) and *mc* ($\hat{\beta}_4$) were all larger than 0.05, except for $\hat{\beta}_4$ in the LVEF-regression. Hence we can conclude that compared to the "standard strategy", the influence of the "motion-reduced" or the "motion-corrected" strategies on the measured cardiac parameters are statistically insignificant at a 5% significance level, however the "motion-corrected strategy" induced a statistically significant change to the LVEF. The changes in cardiac parameters for each of the significant OLS-estimates are listed in Table 4.

We also noticed that the estimated parameters for dummies *m2* to *m5* are significant (their p-values are $< 0.05$). It means that the individual differences in the measured cardiac parameters were much bigger than the differences that could be induced by the different respiratory-motion correction strategies.

## 5.4 Discussion

In this study, three respiratory-motion correction strategies were examined in order to study the influence and potential benefit of respiratory-motion compensating for high-resolution ECG-gated myocardial perfusion SPECT in mice. Qualitatively, the line profiles through the images and cardiac parameters that were derived from the images that were formed using three different motion correction strategies showed no large differences. Furthermore, we can discuss the influence of respiratory-motion correction, image filtering and animal positioning on the measured cardiac parameters by using our statistical model.

*Influence of strategies to correct for respiratory motion*: Only the motion-corrected strategy induced a statistically significant change to LVEF. However the absolute change was

0.012, which is only 2.1% of the reference LVEF. Therefore we could state that the different motion-correction strategies that were tested in this chapter have no big influence on the measured cardiac parameters at all. In other words, compared to the "standard strategy", neither the "motion-reduced strategy" nor the "motion-corrected strategy" showed changes in the cardiac parameters larger than 2.1%. Nevertheless, the "standard strategy" (i.e. ECG-gating and no respiratory-motion compensation) is the simplest strategy since it does not require recording and processing of respiratory signals.

*Influence of image filtering*: According to the estimated regression models, 5% changes to the reference EDV, ESV and LVEF could be induced by respectively 0.37 mm, 0.18 mm and 0.40 mm changes in the FWHM of the Gaussian filter, with other factors remaining the same. In practice, researchers usually use the same filter for images from the same dataset, but may unconsciously use different filters for e.g. images reconstructed on different days in a longitudinal study before comparing them. One should be aware of this issue, because e.g. once the difference of the FWHM of the filter exceeds 0.4 mm, there could be errors of more than 5% in comparisons between the measured LVEFs.

*Influence of animal positioning*: An absolute change of about 3.1 µl (EDV), 2.5 µl (ESV) and 0.018 (LVEF) occurred when the animal positioning was changed, with other factors the same. These are 6.2%, 11% and 3.2% of the reference EDV, ESV and LVEF, respectively. Although further experiments and analysis are needed to investigate the underlying reasons causing the observed changes, it is wise that for the same group of cardiac studies one keeps the animal position the same.

The mouse model that is used in this study may play an important role as a preclinical model for evaluating effects of therapeutics on cardiac function in future studies. In the current study ^{99m}Tc-tetrofosmin was used. This tracer enables the quantification of myocardial perfusion and function in a single scan. In this study we determined the influence of respiratory motion, image filtering and animal positioning on cardiac parameters. There are still other effects such as scatter and attenuation that may influence the measurements, although these effects are very small and can be easily corrected in small-animal imaging when clinical tracers are used [32-36].

In short, even for sub-half-millimeter myocardial SPECT, our results indicate that respiratory gating has no significant effect on measured cardiac parameters, while image filtering and the position animal(s) should be kept the same for all scans in a comparative study. Of course, it could be that when animals that are scanned under different anesthetic regimes or have compromised pulmonary function, quite different ranges of respiratory motion may occur. In such cases, simultaneous ECG and respiratory gating combined with respiratory-motion correction may still be important and useful. Further investigations are required in order to study possible effects on measured cardiac parameters under such conditions.

## *5.5 Conclusions*

For high-resolution cardiac perfusion SPECT in mice, respiratory gating has no significant influence on measured LV volumes and LVEFs. Image filtering and animal positioning do have a big influence on these parameters and should therefore be kept the same for all scans in a comparative study.

**TABLE I**. Cardiac parameters measured from reconstructed images. S: standard strategy. MR: motion-reduced strategy. MC: motion-corrected strategy.

Mouse 1 (31 g)

| Filter (mm) | EDV (μl) | | | | | | ESV (μl) | | | | | | LVEF | | | | | |
|---|---|---|---|---|---|---|---|---|---|---|---|---|---|---|---|---|---|---|
| | Supine | | | Prone | | | Supine | | | Prone | | | Supine | | | Prone | | |
| | S | MR | MC | S | MR | MC | S | MR | MC | S | MR | MC | S | MR | MC | S | MR | MC |
| 0.5 | 59 | 59 | 58 | 50 | 51 | 48 | 26 | 27 | 25 | 18 | 19 | 18 | .56 | .54 | .58 | .64 | .62 | .63 |
| 0.6 | 58 | 58 | 57 | 49 | 50 | 47 | 25 | 25 | 24 | 17 | 19 | 17 | .56 | .57 | .58 | .65 | .63 | .64 |
| 0.7 | 58 | 58 | 57 | 48 | 50 | 47 | 24 | 25 | 23 | 18 | 18 | 16 | .59 | .56 | .59 | .63 | .64 | .65 |
| 0.8 | 57 | 58 | 56 | 47 | 48 | 46 | 24 | 24 | 23 | 17 | 18 | 16 | .57 | .59 | .59 | .63 | .62 | .66 |
| 0.9 | 56 | 57 | 56 | 46 | 48 | 45 | 24 | 23 | 22 | 17 | 16 | 15 | .57 | .59 | .60 | .64 | .66 | .66 |
| 1.0 | 55 | 56 | 55 | 45 | 47 | 44 | 22 | 23 | 22 | 15 | 16 | 15 | .59 | .60 | .60 | .66 | .65 | .67 |

Mouse 2 (30 g)

| Filter (mm) | EDV (μl) | | | | | | ESV (μl) | | | | | | LVEF | | | | | |
|---|---|---|---|---|---|---|---|---|---|---|---|---|---|---|---|---|---|---|
| | Supine | | | Prone | | | Supine | | | Prone | | | Supine | | | Prone | | |
| | S | MR | MC | S | MR | MC | S | MR | MC | S | MR | MC | S | MR | MC | S | MR | MC |
| 0.5 | 40 | 39 | 39 | 40 | 40 | 39 | 16 | 17 | 16 | 19 | 19 | 18 | .59 | .57 | .59 | .51 | .52 | .54 |
| 0.6 | 39 | 39 | 39 | 39 | 39 | 38 | 16 | 16 | 15 | 18 | 19 | 17 | .60 | .58 | .60 | .54 | .53 | .55 |
| 0.7 | 39 | 39 | 38 | 39 | 39 | 38 | 16 | 16 | 15 | 17 | 19 | 17 | .60 | .59 | .60 | .56 | .52 | .56 |
| 0.8 | 38 | 38 | 38 | 39 | 38 | 37 | 14 | 16 | 14 | 16 | 17 | 16 | .62 | .59 | .63 | .58 | .55 | .57 |
| 0.9 | 38 | 38 | 37 | 38 | 37 | 37 | 13 | 15 | 13 | 15 | 17 | 16 | .64 | .61 | .65 | .60 | .55 | .58 |
| 1.0 | 37 | 37 | 37 | 37 | 36 | 36 | 13 | 13 | 13 | 15 | 16 | 15 | .65 | .64 | .65 | .59 | .56 | .58 |

Mouse 3 (30 g)

| Filter (mm) | EDV (μl) | | | | | | ESV (μl) | | | | | | LVEF | | | | | |
|---|---|---|---|---|---|---|---|---|---|---|---|---|---|---|---|---|---|---|
| | Supine | | | Prone | | | Supine | | | Prone | | | Supine | | | Prone | | |
| | S | MR | MC | S | MR | MC | S | MR | MC | S | MR | MC | S | MR | MC | S | MR | MC |
| 0.5 | 38 | 39 | 38 | 42 | 43 | 42 | 14 | 13 | 13 | 16 | 16 | 14 | .62 | .68 | .66 | .62 | .62 | .67 |
| 0.6 | 38 | 39 | 38 | 41 | 42 | 41 | 14 | 12 | 12 | 15 | 16 | 14 | .64 | .69 | .68 | .62 | .62 | .65 |
| 0.7 | 37 | 38 | 37 | 41 | 42 | 40 | 13 | 13 | 12 | 14 | 16 | 13 | .66 | .67 | .68 | .65 | .63 | .67 |
| 0.8 | 37 | 37 | 36 | 40 | 41 | 40 | 12 | 12 | 11 | 14 | 14 | 13 | .68 | .68 | .68 | .65 | .65 | .67 |
| 0.9 | 36 | 37 | 35 | 40 | 40 | 39 | 12 | 11 | 11 | 13 | 14 | 12 | .67 | .69 | .69 | .68 | .65 | .71 |
| 1.0 | 35 | 36 | 34 | 39 | 40 | 37 | 11 | 11 | 11 | 13 | 13 | 12 | .69 | .69 | .69 | .67 | .68 | .68 |

Mouse 4 (30 g)

| Filter (mm) | EDV (μl) | | | | | | ESV (μl) | | | | | | LVEF | | | | | |
|---|---|---|---|---|---|---|---|---|---|---|---|---|---|---|---|---|---|---|
| | Supine | | | Prone | | | Supine | | | Prone | | | Supine | | | Prone | | |
| | S | MR | MC | S | MR | MC | S | MR | MC | S | MR | MC | S | MR | MC | S | MR | MC |
| 0.5 | 58 | 61 | 56 | 65 | 65 | 65 | 24 | 27 | 24 | 31 | 31 | 31 | .58 | .56 | .57 | .53 | .52 | .53 |
| 0.6 | 58 | 61 | 56 | 64 | 65 | 65 | 25 | 26 | 23 | 31 | 31 | 31 | .58 | .57 | .60 | .51 | .52 | .53 |
| 0.7 | 58 | 59 | 56 | 64 | 64 | 64 | 24 | 26 | 22 | 30 | 31 | 31 | .59 | .56 | .60 | .53 | .52 | .52 |
| 0.8 | 55 | 59 | 54 | 63 | 64 | 63 | 23 | 24 | 22 | 30 | 30 | 31 | .57 | .59 | .59 | .52 | .52 | .51 |
| 0.9 | 54 | 56 | 52 | 63 | 63 | 63 | 23 | 23 | 21 | 30 | 30 | 30 | .58 | .58 | .60 | .53 | .52 | .52 |
| 1.0 | 53 | 56 | 52 | 62 | 62 | 63 | 22 | 23 | 21 | 28 | 29 | 29 | .59 | .59 | .60 | .55 | .54 | .53 |

Mouse 5 (31 g)

| Filter (mm) | EDV (μl) | | | | | | ESV (μl) | | | | | | LVEF | | | | | |
|---|---|---|---|---|---|---|---|---|---|---|---|---|---|---|---|---|---|---|
| | Supine | | | Prone | | | Supine | | | Prone | | | Supine | | | Prone | | |
| | S | MR | MC | S | MR | MC | S | MR | MC | S | MR | MC | S | MR | MC | S | MR | MC |
| 0.5 | 54 | 54 | 54 | 68 | 68 | 68 | 29 | 29 | 27 | 37 | 37 | 37 | .46 | .47 | .51 | .46 | .45 | .46 |
| 0.6 | 54 | 53 | 54 | 68 | 67 | 67 | 28 | 28 | 26 | 37 | 37 | 36 | .48 | .47 | .51 | .46 | .45 | .46 |
| 0.7 | 53 | 53 | 53 | 67 | 67 | 67 | 29 | 27 | 26 | 36 | 37 | 36 | .46 | .49 | .50 | .46 | .45 | .46 |
| 0.8 | 52 | 52 | 52 | 67 | 67 | 67 | 28 | 26 | 26 | 35 | 35 | 35 | .47 | .50 | .50 | .48 | .47 | .48 |
| 0.9 | 52 | 51 | 51 | 66 | 66 | 66 | 27 | 27 | 25 | 34 | 35 | 34 | .49 | .48 | .51 | .48 | .48 | .48 |
| 1.0 | 51 | 51 | 50 | 65 | 66 | 66 | 25 | 25 | 24 | 34 | 33 | 33 | .52 | .50 | .52 | .48 | .50 | .50 |

**TABLE II**. Description of variables in regression analyses.

| Dependent variables | Description |
| --- | --- |
| *edv* | EDV (in µl) |
| *esv* | ESV (in µl) |
| *lvef* | LVEF (expressed as decimal) |
| Independent variables | Description |
| *filter* | FWHM (in mm) of Gaussian filter |
| *prone* | Dummy variable (= 1 for prone position and = 0 for supine position) |
| *mr* | Dummy variable (= 1 for motion-reduced strategy and = 0 for others) |
| *mc* | Dummy variable (= 1 for motion-corrected strategy and = 0 for others) |
| *m2* | Dummy variable (= 1 for Mouse 2 and = 0 for others) |
| *m3* | Dummy variable (= 1 for Mouse 3 and = 0 for others) |
| *m4* | Dummy variable (= 1 for Mouse 4 and = 0 for others) |
| *m5* | Dummy variable (= 1 for Mouse 5 and = 0 for others) |

**TABLE III**. OLS estimates of regression of EDV, ESV and LVEF by using linear model (1).

### EDV

| Estimate | Mean | Standard Error | $p$-value | $R^2$ |
|---|---|---|---|---|
| $\hat{\beta}_1$ (for *filter*) | −6.70 | 1.81 | 0.000 | |
| $\hat{\beta}_2$ (for *prone*) | 3.13 | 0.62 | 0.000 | |
| $\hat{\beta}_3$ (for *mr*) | 0.57 | 0.76 | 0.456* | |
| $\hat{\beta}_4$ (for *mc*) | −0.65 | 0.76 | 0.393* | |
| $\hat{\beta}_5$ (for *m2*) | −14.14 | 0.98 | 0.000 | 0.8552 |
| $\hat{\beta}_6$ (for *m3*) | −13.58 | 0.98 | 0.000 | |
| $\hat{\beta}_7$ (for *m4*) | 7.69 | 0.98 | 0.000 | |
| $\hat{\beta}_8$ (for *m5*) | 7.31 | 0.98 | 0.000 | |
| $\hat{\beta}_0$ (constant) | 55.82 | 1.62 | 0.000 | |

### ESV

| Estimate | Mean | Standard Error | $p$-value | $R^2$ |
|---|---|---|---|---|
| $\hat{\beta}_1$ (for *filter*) | −6.14 | 1.25 | 0.000 | |
| $\hat{\beta}_2$ (for *prone*) | 2.50 | 0.43 | 0.000 | |
| $\hat{\beta}_3$ (for *mr*) | 0.42 | 0.52 | 0.425* | |
| $\hat{\beta}_4$ (for *mc*) | −0.77 | 0.52 | 0.143* | |
| $\hat{\beta}_5$ (for *m2*) | −4.53 | 0.67 | 0.000 | 0.8608 |
| $\hat{\beta}_6$ (for *m3*) | −7.39 | 0.67 | 0.000 | |
| $\hat{\beta}_7$ (for *m4*) | 6.44 | 0.67 | 0.000 | |
| $\hat{\beta}_8$ (for *m5*) | 10.67 | 0.67 | 0.000 | |
| $\hat{\beta}_0$ (constant) | 23.92 | 1.11 | 0.000 | |

### LVEF

| Estimate | Mean | Standard Error | $p$-value | $R^2$ |
|---|---|---|---|---|
| $\hat{\beta}_1$ (for *filter*) | 0.072 | 0.011 | 0.000 | |
| $\hat{\beta}_2$ (for *prone*) | −0.018 | 0.004 | 0.000 | |
| $\hat{\beta}_3$ (for *mr*) | −0.004 | 0.005 | 0.385* | |
| $\hat{\beta}_4$ (for *mc*) | 0.012 | 0.005 | 0.017 | |
| $\hat{\beta}_5$ (for *m2*) | −0.028 | 0.006 | 0.000 | 0.8605 |
| $\hat{\beta}_6$ (for *m3*) | 0.053 | 0.006 | 0.000 | |
| $\hat{\beta}_7$ (for *m4*) | −0.057 | 0.006 | 0.000 | |
| $\hat{\beta}_8$ (for *m5*) | −0.131 | 0.006 | 0.000 | |
| $\hat{\beta}_0$ (constant) | 0.564 | 0.010 | 0.000 | |

* insignificant ($p > 0.05$).

**TABLE IV**. Interpretation of statistically significant coefficients.

| Estimate | Interpretation |
|---|---|
| **For EDV:** | |
| $\hat{\beta}_1 = -6.7$ | When FWHM of the Gaussian filter increases by 1 mm, EDV decreases by 6.7 µl, ceteris paribus. |
| $\hat{\beta}_2 = 3.1$ | When position changes from supine to prone, EDV increases by 3.1 µl, ceteris paribus. |
| **For ESV:** | |
| $\hat{\beta}_1 = -6.1$ | When FWHM of the Gaussian filter increases by 1 mm, ESV decreases by 6.1 µl, ceteris paribus. |
| $\hat{\beta}_2 = 2.5$ | When position changes from supine to prone, ESV increases by 2.5 µl, ceteris paribus. |
| **For LVEF:** | |
| $\hat{\beta}_1 = 0.072$ | When FWHM of the Gaussian filter increases by 1 mm, LVEF increases by 0.072, ceteris paribus. |
| $\hat{\beta}_2 = -0.018$ | When position changes from supine to prone, LVEF decreases by 0.018, ceteris paribus. |
| $\hat{\beta}_4 = 0.012$ | When strategy changes from standard to motion-corrected, LVEF increases by 0.012, ceteris paribus. |

## *Bibliography*

[1] H. L. Boyd, R. N. Gunn, N. V. Marinho, S. P. Karwatowski, D. L. Bailey, D. C. Costa, and P. G. Camici, "Non-invasive measurement of left ventricular volumes and function by gated positron emission tomography," *Eur. J. Nucl. Med.,* vol. 23, no. 12, pp. 1594-602, 1996.

[2] K. Rajappan, L. Livieratos, P. G. Camici, and D. J. Pennell, "Measurement of ventricular volumes and function: a comparison of gated PET and cardiovascular magnetic resonance," *J. Nucl. Med.,* vol. 43, no. 6, pp. 806-10, 2002.

[3] R. H. Slart, J. J. Bax, R. M. de Jong, J. de Boer, H. J. Lamb, P. H. Mook, A. T. Willemsen, W. Vaalburg, D. J. van Veldhuisen, and P. L. Jager, "Comparison of gated PET with MRI for evaluation of left ventricular function in patients with coronary artery disease," *J. Nucl. Med.,* vol. 45, no. 2, pp. 176-82, 2004.

[4] R. H. Slart, J. J. Bax, D. J. van Veldhuisen, E. E. van der Wall, R. A. Dierckx, and P. L. Jager, "Imaging techniques in nuclear cardiology for the assessment of myocardial viability," *Int. J. Cardiovasc. Imaging,* vol. 22, no. 1, pp. 63-80, 2006.

[5] L. Boucher, S. Rodrigue, R. Lecomte, and F. Benard, "Respiratory gating for 3-dimensional PET of the thorax: feasibility and initial results," *J. Nucl. Med.,* vol. 45, no. 2, pp. 214-9, 2004.

[6]     F. Lamare, M. J. Ledesma Carbayo, T. Cresson, G. Kontaxakis, A. Santos, C. C. Le Rest, A. J. Reader, and D. Visvikis, "List-mode-based reconstruction for respiratory motion correction in PET using non-rigid body transformations," *Phys. Med. Biol.,* vol. 52, no. 17, pp. 5187-204, 2007.

[7]     G. J. Klein, B. W. Reutter, M. H. Ho, J. H. Reed, and R. H. Huesman, "Real-time system for respiratory-cardiac gating in positron tomography," *IEEE Trans. Nucl. Sci.,* vol. 45, no. 4, pp. 2139-2143, 1998.

[8]     L. Livieratos, K. Rajappan, L. Stegger, K. Schafers, D. L. Bailey, and P. G. Camici, "Respiratory gating of cardiac PET data in list-mode acquisition," *Eur. J. Nucl. Med. Mol. Imaging,* vol. 33, no. 5, pp. 584-8, 2006.

[9]     A. Martinez-Moller, D. Zikic, R. M. Botnar, R. A. Bundschuh, W. Howe, S. I. Ziegler, N. Navab, M. Schwaiger, and S. G. Nekolla, "Dual cardiac-respiratory gated PET: implementation and results from a feasibility study," *Eur. J. Nucl. Med. Mol. Imaging,* vol. 34, no. 9, pp. 1447-54, 2007.

[10]    F. Buther, M. Dawood, L. Stegger, F. Wubbeling, M. Schafers, O. Schober, and K. P. Schafers, "List mode-driven cardiac and respiratory gating in PET," *J. Nucl. Med.,* vol. 50, no. 5, pp. 674-681, 2009.

[11]    F. Gigengack, L. Ruthotto, M. Burger, C. H. Wolters, X. Y. Jiang, and K. P. Schafers, "Motion correction in dual gated cardiac PET using mass-preserving image registration," *IEEE Trans. Med. Imag.,* vol. 31, no. 3, pp. 698-712, 2012.

[12]    A. Constantinesco, P. Choquet, L. Monassier, V. Israel-Jost, and L. Mertz, "Assessment of left ventricular perfusion, volumes, and motion in mice using pinhole gated SPECT," *J. Nucl. Med.,* vol. 46, no. 6, pp. 1005-1011, 2005.

[13]    R. A. de Kemp, F. H. Epstein, C. Catana, B. M. Tsui, and E. L. Ritman, "Small-animal molecular imaging methods," *J. Nucl. Med.,* vol. 51, no. Suppl, pp. 18S-32S, 2010.

[14]    L. R. Goethals, F. De Geeter, C. Vanhove, B. Roosens, H. Devos, and T. Lahoutte, "Improved quantification in pinhole gated myocardial perfusion SPECT using micro-CT and ultrasound information," *Contrast Media Mol. Imaging,* vol. 7, no. 2, pp. 167-74, 2012.

[15]    C. Goetz, L. Monassier, P. Choquet, and A. Constantinesco, "Assessment of right and left ventricular function in healthy mice by blood-pool pinhole gated SPECT," *C. R. Biol.,* vol. 331, no. 9, pp. 637-47, 2008.

[16]    R. Golestani, C. Wu, R. A. Tio, C. J. Zeebregts, A. D. Petrov, F. J. Beekman, R. A. Dierckx, H. H. Boersma, and R. H. Slart, "Small-animal SPECT and SPECT/CT: application in cardiovascular research," *Eur. J. Nucl. Med. Mol. Imaging,* vol. 37, no. 9, pp. 1766-77, 2010.

[17]    J. H. Strydhorst, F. H. Leenen, T. D. Ruddy, and R. G. Wells, "Reproducibility of serial left ventricle perfusion, volume, and ejection fraction measurements using multiplexed multipinhole SPECT in healthy rats and rats after myocardial infarction," *J. Nucl. Med.,* vol. 52, no. 8, pp. 1285-92, 2011.

[18]    C. Vanhove, T. Lahoutte, M. Defrise, A. Bossuyt, and P. R. Franken, "Reproducibility of left ventricular volume and ejection fraction measurements in rat using pinhole gated SPECT," *Eur. J. Nucl. Med. Mol. Imaging,* vol. 32, no. 2, pp. 211-20, 2005.

[19]    Y. F. Yang, S. Rendig, S. Siegel, D. F. Newport, and S. R. Cherry, "Cardiac PET imaging in mice with simultaneous cardiac and respiratory gating," *Phys. Med. Biol.,* vol. 50, no. 13, pp. 2979-2989, 2005.

[20]    V. R. D. Kakhki, and R. Sadeghi, "Gated myocardial perfusion SPECT in patients with a small heart: Effect of zooming and filtering," *Clin. Nucl. Med.,* vol. 32, no. 5, pp. 404-406, 2007.

[21]    F. M. Lavender, R. T. Meades, A. Al-Nahhas, and K. S. Nijran, "Factors affecting the measurement of left ventricular ejection fraction in myocardial perfusion imaging," *Nucl. Med. Commun.,* vol. 30, no. 5, pp. 350-355, 2009.

[22]    M. Pai, Y. J. Yang, K. C. Im, I. K. Hong, S. C. Yun, D. H. Kang, J. K. Song, and D. H. Moon, "Factors affecting accuracy of ventricular volume and ejection fraction measured by gated Tl-201 myocardial perfusion single photon emission computed tomography," *Int. J. Cardiovasc. Imaging,* vol. 22, no. 5, pp. 671-681, 2006.

[23]    P. Vera, A. Manrique, V. Pontvianne, A. Hitzel, R. Koning, and A. Cribier, "Thallium-gated SPECT in patients with major myocardial infarction: Effect of filtering and zooming in comparison with equilibrium radionuclide imaging and left ventriculography," *J. Nucl. Med.,* vol. 40, no. 4, pp. 513-521, 1999.

[24]    G. A. Wright, M. McDade, W. Martin, and I. Hutton, "Quantitative gated SPECT: the effect of reconstruction filter on calculated left ventricular ejection fractions and volumes," *Phys. Med. Biol.,* vol. 47, no. 8, pp. N99-N105, 2002.

[25]    D. Berman, G. Germano, H. Lewin, X. P. Kang, P. B. Kavanagh, P. Tapnio, M. Harris, and J. Friedman, "Comparison of post-stress ejection fraction and relative left ventricular volumes by automatic analysis of gated myocardial perfusion single-photon emission computed tomography acquired in the supine and prone positions," *J. Nucl. Cardiol.,* vol. 5, no. 1, pp. 40-47, 1998.

[26]    W. M. Schaefer, C. S. Lipke, H. P. Kuhl, K. C. Koch, H. J. Kaiser, P. Reinartz, B. Nowak, and U. Buell, "Prone versus supine patient positioning during gated $^{99m}$Tc-sestamibi SPECT: effect on left ventricular volumes, ejection fraction, and heart rate," *J. Nucl. Med.,* vol. 45, no. 12, pp. 2016-20, 2004.

[27]    K. Yap, P. Campbell, M. Cherk, C. McGrath, and V. Kalff, "Effect of prone versus supine positioning on left ventricular ejection fraction (LVEF) and heart rate using ECG gated Tl-201 myocardial perfusion scans and gated cardiac blood pool scans," *J. Med. Imaging Radiat. Oncol.,* vol. 56, no. 5, pp. 525-31, 2012.

[28]    F. van der Have, B. Vastenhouw, R. M. Ramakers, W. Branderhorst, J. O. Krah, C. Ji, S. G. Staelens, and F. J. Beekman, "U-SPECT-II: an ultra-high-resolution device for molecular small-animal imaging," *Journal of Nuclear Medicine,* vol. 50, no. 4, pp. 599-605, 2009.

[29]    W. Branderhorst, B. Vastenhouw, and F. J. Beekman, "Pixel-based subsets for rapid multi-pinhole SPECT reconstruction," *Physics in Medicine and Biology,* vol. 55, no. 7, pp. 2023-34, 2010.

[30]    S. Klein, M. Staring, K. Murphy, M. A. Viergever, and J. P. Pluim, "elastix: a toolbox for intensity-based medical image registration," *IEEE Trans. Med. Imag.,* vol. 29, no. 1, pp. 196-205, 2010.

[31]    E. P. Ficaro, B. C. Lee, J. N. Kritzman, and J. R. Corbett, "Corridor4DM: the Michigan method for quantitative nuclear cardiology," *J. Nucl. Cardiol.,* vol. 14, no. 4, pp. 455-65, 2007.

[32]    C. L. Chen, Y. Wang, J. J. Lee, and B. M. Tsui, "Toward quantitative small animal pinhole SPECT: assessment of quantitation accuracy prior to image compensations," *Mol. Imaging Biol.,* vol. 11, no. 3, pp. 195-203, 2009.

[33]    C. Vanhove, M. Defrise, A. Bossuyt, and T. Lahoutte, "Improved quantification in single-pinhole and multiple-pinhole SPECT using micro-CT information," *Eur. J. Nucl. Med. Mol. Imaging,* vol. 36, no. 7, pp. 1049-1063, 2009.

[34]    C. Wu, J. R. de Jong, H. A. Gratama van Andel, F. van der Have, B. Vastenhouw, P. Laverman, O. C. Boerman, R. A. Dierckx, and F. J. Beekman, "Quantitative multi-pinhole small-animal SPECT: uniform versus non-uniform Chang attenuation correction," *Phys. Med. Biol.,* vol. 56, no. 18, pp. N183-N193, 2011.

[35]    C. Wu, H. A. Gratama van Andel, P. Laverman, O. C. Boerman, and F. J. Beekman, "Effects of attenuation map accuracy on attenuation-corrected micro-SPECT images," *EJNMMI Res.,* vol. 3, no. 1, pp. 7, 2013.

[36]    C. Wu, F. van der Have, B. Vastenhouw, R. A. Dierckx, A. M. Paans, and F. J. Beekman, "Absolute quantitative total-body small-animal SPECT with focusing pinholes," *Eur. J. Nucl. Med. Mol. Imaging,* vol. 37, no. 11, pp. 2127-2135, 2010.

# 6. Fast count-regulated OSEM reconstruction with adaptive resolution recovery

## *Abstract*

Ordered Subsets Expectation Maximization (OSEM) is widely used to accelerate tomographic reconstruction. Speed-up of OSEM over Maximum Likelihood Expectation Maximization (MLEM) is close to the number of subsets (NS). Recently we significantly increased the speed-up achievable with OSEM by specific subset choice (Pixel-based OSEM). However, a high NS can cause undesirable noise levels, quantitative inaccuracy or even disappearance of lesions in low-activity image regions, while a low NS leads to prohibitively long reconstructions or unrecovered details in highly active regions.

Here we introduce Count-Regulated OSEM (CROSEM) that locally adapts the effective NS based on the estimated amount of detected photons originating from individual voxels. CROSEM was tested using multi-pinhole SPECT simulations and *in vivo* imaging. With the maximum NS set to 128, CROSEM attained acceleration factors close to 128 in high-activity regions and kept quantitative accuracy in low-activity regions close to that of MLEM. At equal cold-lesion contrast in high-activity regions, CROSEM exhibited lower noise than MLEM in low-activity regions. CROSEM is a fast and stable alternative to OSEM preventing excessive image noise and quantitative errors in low-activity regions while achieving high-resolution recovery in structures with high activity uptake.

## 6.1 Introduction

In recent years, statistical iterative algorithms have become the method of choice for reconstructing Single Photon Emission Computed Tomography (SPECT) and Positron Emission Tomography (PET) images [1-5]. Additionally, significant interest is being shown in accelerated versions of these algorithms for X-ray Computed Tomography [6-13]. Compared to analytical reconstruction methods, statistical iterative methods have been shown to (i) be more robust to statistical noise, (ii) be applicable to complex detector- and collimator geometries and (iii) allow better modeling of the physical detection process, which can be used to correct for several image-degrading effects. Of these iterative methods, Maximum Likelihood Expectation Maximization (MLEM, [14, 15]) has become the gold standard, mostly due to its consistent and predictable convergence behavior, non-negativity constraint and ease of implementation.

Despite the ever increasing computer speed, MLEM remains computationally costly as the size of system matrices is also increasing over time. This trend is driven by, on the one hand, the use of more refined models of photon transport which are desired for better resolution recovery and quantitatively accurate images [16], and on the other hand by the demand for finer voxel grids to accommodate the increasing resolution of modern (preclinical) SPECT and PET [17]. A major breakthrough that has led to the widespread application of statistical iterative algorithms in medical image reconstruction was the introduction of block-iterative methods. These methods use ordered subsets (OS) of the projection data in each sub-iteration of the algorithm to accelerate resolution recovery. This principle was applied to MLEM to yield the Ordered Subsets Expectation Maximization algorithm (OSEM, [18]). Despite the fact that OSEM has no theoretical convergence proof and that the approach is heuristically motivated, OSEM is currently the most widely used iterative reconstruction method in emission tomography: OSEM is fast, easy to implement and has been shown to yield acceptable images for a large variety of imaging studies. Studies have shown that for parallel hole-collimated SPECT, OSEM provides almost the same reconstructed images as MLEM, when the number of subsets (NS) is not too high [19, 20] and that the acceleration factor is roughly proportional to the NS [18, 19]. In most OSEM implementations, each subset contains a number of complete SPECT projections. It was recently shown that it can be more advantageous to use pixel-based subset schemes (Pixel-based OSEM; POSEM, [21]). These schemes deviate from traditional subset schemes in that subsets do not consist of grouped projection views, rather the detector pixels in each subset are spread out in a regular pattern over the entire detector and therefore each subset contains detector pixels from all projection views. This way, subset balance does not deteriorate as fast as with traditional subset schemes as the NS increases. In a number of cases POSEM could achieve acceleration factors that were an order of magnitude higher than those of traditional OSEM when applied to multi-pinhole SPECT.

This paper addresses and solves a shortcoming of OSEM that, to our knowledge, has not been reported previously in literature. The problems that can rise when OSEM is operated at a high NS are illustrated in Fig. 1a. This figure shows maximum-intensity-projections

(MIPs) of MLEM and OSEM reconstructions of a SPECT scan of a tumor-bearing mouse. From the MLEM reconstruction it is clear that the tracer accumulated in the kidneys and to a much lesser extent in the tumor. In OSEM reconstructed images activity in more and more voxels was erased as the NS increased; e.g. for OSEM with 64 subsets activity in the tumor completely disappeared and for OSEM with 128 subsets activity in the entire image was erased. Note that the grayscale is the same for all MIPs in Fig. 1. These major reconstruction artifacts occur if a large fraction of the (small) detector pixels in each subset contain no counts. In such cases, it may happen that a subset exists in which all detector pixels that occur in the update term of a certain voxel do not contain any counts and, as a consequence, the activity in this voxel will be updated to zero in the sub-iteration that uses this subset. Due to the multiplicative nature of the OSEM update step the activity in this voxel will then remain zero, even if detector pixels in other subsets that are used to update the voxel do contain counts. As shown in Fig. 1a, this can lead to the permanent erasure of activity. Furthermore, because OSEM strives to make re-projected activity consistent with measured projections, extra activity may accumulate in surrounding voxels. The occurrence of these effects becomes more likely for a decreasing number of counts and/or an increase of the NS.

To prevent these reconstruction artifacts fewer subsets could be used. However, since there is no general rule for selecting a low enough NS to avoid quantification errors and tumor/lesion detection loss in regions with low activity, one needs to always select a low NS and ends up with (i) very time consuming reconstructions and noisy low-activity regions due to the high number of iterations that is required to achieve a high resolution in high-activity regions, or (ii) a low resolution in the entire image if a low number of iterations is performed to save reconstruction time. As a simple solution, one may also consider to only perform nonzero activity updates (Fig. 1b) or to simply exclude detector pixels that contain no counts (Fig. 1c). Although these two strategies may work for moderate/high count (PET) data, we have tried these options and found reconstructions full of artifacts when applied to (low-count) pinhole SPECT. Note that with pinhole SPECT it may regularly occur that the majority of the detector pixels contain no counts. Therefore, leaving out the detector pixels that contain no counts means not using a substantial amount of the detector pixels. These pixels do contain information about the likelihood of a certain activity distribution as they indicate that the voxels that project onto them probably contain low activities. Therefore, simply excluding these pixels resulted in severe overestimation of the activity in all images presented in Fig. 1c (i.e. overall black MIPs).
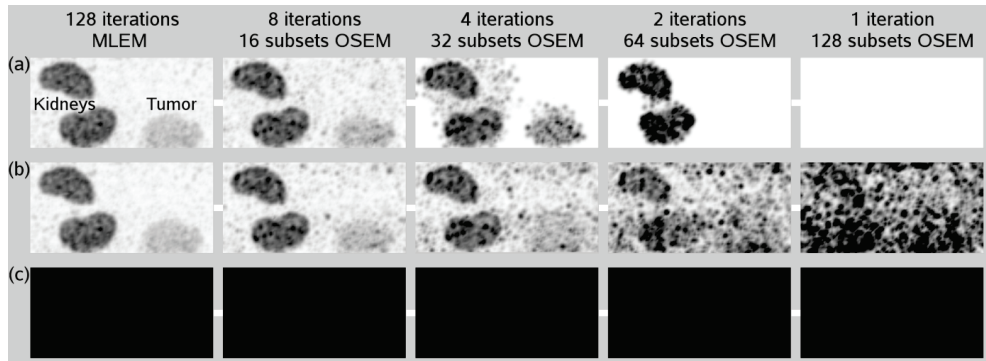
**Figure 1**. *Maximum-intensity-projections (MIPs) of SPECT reconstructions of mouse with tumour (16.7 MBq $^{99m}$Tc-prostate-specific-membrane-antigen-targeted ($^{99m}$Tc-PSMA) radioligand [22], scanned for 32 min starting 4 h post injection). The grayscale is the same for all MIPs. MLEM and OSEM reconstructions* **(a)** *if voxel updates to zero activity are allowed,* **(b)** *if voxel updates to zero activity are not allowed* **(c)** *if detector pixels with no counts are simply excluded from the measured data.*

These problems can be prevented by the use of an algorithm that adapts its acceleration speed (i.e. the NS) automatically and locally depending on local activity estimates. Such a type of EM algorithm was already introduced in [23] and referred to as Statistically Regulated EM (StatREM). StatREM utilizes the concepts of statistically adaptive subset formation and spatially adaptive voxel updates. StatREM closely resembles OSEM in that subsets of the measured projection data are used for voxel updates. However, while OSEM updates all voxels in each sub-iteration, StatREM only updates a voxel if it passes a statistical hypothesis test which considers the differences between the simulated and measured counts for those detector pixels that occur in the update term of a certain voxel; i.e. the system matrix elements (sensitivities) corresponding to these voxel-pixel combinations are nonzero. If the test passes (the difference is significant) the conclusion is drawn that this voxel is at least partially responsible for the mismatch between the simulated and measured data and the voxel is updated. It was shown that StatREM accelerated recovery of spatial resolution in high-activity image regions, while noise artifacts in low-activity regions were reduced. However, the voxel-wise test used within StatREM does not take into account how likely it is that counts in a certain detector pixel originate from the voxel under consideration. For example, a pixel may only be slightly sensitive to the photons originating from a certain voxel (i.e. low value of the system matrix element) and therefore the voxel may not be expected to contribute much to that detector pixel. Or, alternatively, a voxel may be estimated to have a low activity and therefore it will not contribute many counts to any detector pixel. This may result in suboptimal images, as we will show later in this paper. To overcome these problems we introduce a new Count-Regulated version of the OSEM algorithm (CROSEM): CROSEM also uses adaptive subset formation and spatially adaptive voxel updates by means of a voxel-wise test, however the test used within CROSEM is based on the estimated contribution (i.e. counts) of individual voxels to the detector pixels taking into account (i) the probability that a

photon from that voxel ends up being detected in a certain detector pixel (i.e. the value of the system matrix element) and, (ii) the estimated activity level of the voxel under consideration.

The aim of this paper is to introduce and validate CROSEM and to show that it automatically achieves a locally adapted resolution-noise trade-off, prevents erasure of activity and noise over-amplification in low-activity image regions while still enabling fast resolution recovery in high-activity regions. We compare CROSEM to MLEM, OSEM and StatREM for multi-pinhole SPECT and illustrate the benefit of CROSEM with reconstructions of *in vivo* data.

## 6.2 Materials and methods

### 6.2.1 Image Reconstruction Algorithms

#### 6.2.1.1 MLEM

In this study we used an implementation of MLEM according to [14] as a basis for OSEM, StatREM and CROSEM. The MLEM update equation is given by:

$$\widetilde{a}_i^{(k)} = \frac{\widetilde{a}_i^{(k-1)}}{\sum_j M_{ij}} \sum_j M_{ij} \frac{p_j}{\widetilde{p}_j^{(k)}} \tag{1}$$

$$\widetilde{p}_j^{(k)} = \sum_i M_{ij} \widetilde{a}_i^{(k-1)} \tag{2}$$

Here, $\widetilde{a}_i^{(k)}$ is the estimated activity in voxel $i$ at the $k^{\text{th}}$ iteration, $p_j$ and $\widetilde{p}_j^{(k)}$ are the measured and estimated (simulated) number of gamma photon counts in detector pixel $j$ with an energy that lies within the selected photopeak window and $M_{ij}$ is the system matrix element representing the probability that a photon emitted from voxel $i$ is detected in detector pixel $j$. In this study the start image is a cylinder with uniform activity.

#### 6.2.1.2 OSEM

OSEM uses the same equation as MLEM to update the image estimate but for each update only a subset of the projection data is used. Such an update step is called a sub-iteration. Only after all subsets have been traversed sequentially, a single OSEM iteration is defined to be completed (full iteration). The OSEM image update is defined by:

$$\widetilde{a}_i^{(k,l)} = \frac{\widetilde{a}_i^{(k,l-1)}}{\sum\limits_{j \in S_l} M_{ij}} \sum_{j \in S_l} M_{ij} \frac{p_j}{\widetilde{p}_j^{(k,l)}}$$ (3)

In (3), $\widetilde{a}_i^{(k,l)}$ represents the activity in voxel $i$ after processing subset $l$ of iteration $k$ and $S_l$ contains the detector pixels of subset $l$.

### 6.2.1.3 StatREM

We implemented StatREM with voxel-wise statistical hypothesis testing according to [23]. The test (paired-sample two-tailed t-test) considers the differences between the measured and simulated counts for the detector pixels that occur in the update term of a certain voxel and assumes that these differences are normally distributed. To make sure that the statistical test is also meaningful in the first iteration, the initial (uniform) start image is scaled such that the total activity in the image is consistent with the total number of counts in the projection data.

The test statistic $TT_i^{(k,l)}$ for voxel $i$ in sub-iteration $(k,l)$ is calculated as follows: the sum of weighted differences $d_i^{(k,l)}$ between the measured and estimated detector counts that occur in the correction term of voxel $i$ in sub-iteration $(k,l)$ is defined as:

$$d_i^{(k,l)} = \sum_{\substack{j \in S_l \\ M_{ij} \neq 0}} \frac{\left(p_j - \widetilde{p}_j^{(k,l)}\right)}{\sqrt{\widetilde{p}_j^{(k,l)}}}$$ (4)

The variable $tt_i^{(k,l)}$ is a running sum that increases each sub-iteration by $d_i^{(k,l)}$:

$$tt_i^{(k,l)} = tt_i^{(k,l-1)} + d_i^{(k,l)}$$ (5)

The test statistic $TT_i^{(k,l)}$ is then calculated by:

$$TT_i^{(k,l)} = \frac{1}{\sqrt{U}} \left(tt_i^{(k,l)}\right)$$ (6)

Note that in (4) $d_i^{(k,l)}$ only includes those detector pixels that occur in the update term of voxel $i$ (i.e. $M_{ij} \neq 0$) and $U$ in (6) is the number of detector pixels that are considered in the calculation of $tt_i^{(k,l)}$. At the same time, both the correction term $C_i^{k,l}$ and the normalization term $N_i^l$, which respectively multiply and normalize the voxel value in each update, are also running sums: each sub-iteration, a new correction and normalization term are defined, which are the correction and normalization term acquired in the current subset added to the terms

acquired in all previous sub-iterations of the current iteration that have been traversed since the last update of voxel $i$:

$$C_i^{(k,l)} = C_i^{(k,l-1)} + \sum_{j \in S_l} M_{ij} \frac{p_j}{\widetilde{p}_j^{(k,l)}} \tag{7}$$

$$N_i^{(l)} = N_i^{(l-1)} + \sum_{j \in S_l} M_{ij} \tag{8}$$

If the t-test demonstrates a statistically significant difference between the measured and simulated projection counts for a specified statistical test level $\alpha$ (i.e. the value of the test statistic $TT_i^{(k,l)}$ that is calculated in (6) lies outside the confidence interval for a confidence level of $100(1-\alpha)\%$ ), the null-hypothesis that the current activity estimates resulted in the measured data is rejected and voxel $i$ is updated:

$$\widetilde{a}_i^{(k,l)} = \frac{\widetilde{a}_i^{(k,l-1)}}{N_i^{(l)}} C_i^{(k,l)} \tag{9}$$

After the update, $tt_i^{(k,l)}, C_i^{(k,l)}$ and $N_i^{(l)}$ are reset to zero. Note that StatREM might still allow activity updates to zero: in case the test passes (i.e. there is a significant difference between the simulated and measured projection counts) and $C_i^{(k,l)}$ is zero (i.e. zero measured counts in the pixels that contributed to $C_i^{(k,l)}$ ) voxel $i$ is updated to zero.

### 6.2.1.4 CROSEM

Like StatREM, CROSEM uses update equations (7)-(9) and only updates voxels that pass a test. However, with CROSEM a different test is performed that is based on the current activity estimate of the voxel under consideration. In order to obtain an initial estimate of each voxel's activity the CROSEM algorithm commences with a single MLEM iteration:

$$\widetilde{a}_i^{(1)} = \frac{\widetilde{a}_i^{(0)}}{\sum_j M_{ij}} \sum_j M_{ij} \frac{p_j}{\widetilde{p}_j^{(1)}} \tag{10}$$

Here, $\widetilde{a}^{(0)}$ and $\widetilde{p}^{(1)}$ are respectively the (uniform) start image and its estimated projection. Further iterations are, like StatREM, performed, using a fixed (high) NS, in this work denoted by $NS^{max}$. Starting from the second iteration, in each sub-iteration one determines the number of counts that a certain voxel is expected to contribute to the detector pixels of the current subset based on the current activity estimate of the voxel. This number, added to the number of counts that this voxel was expected to contribute to all previous subsets since its last update,

determines if the voxel will be updated or not: the voxel is only updated when this number is higher than a certain Count Threshold Value (CTV). To put this in equations, consider the test for voxel $i$ in sub-iteration $(k,l)$: define $\tilde{t}_i^{(k,l)}$ as the estimated (simulated) number of photons originating from voxel $i$ that is detected in the detector pixels of subset $l$:

$$\tilde{t}_i^{(k,l)} = \sum_{j \in S_l} M_{ij} \tilde{a}_i^{(k,l-1)} \qquad (11)$$

The value $T_i^{(k,l)}$ is a running sum that increases each sub-iteration by $\tilde{t}_i^{(k,l)}$:

$$T_i^{(k,l)} = T_i^{(k,l-1)} + \tilde{t}_i^{(k,l)} \qquad (12)$$

Once the running test value $T_i^{(k,l)}$ exceeds the CTV *and* the correction term in (7) is nonzero (i.e. $C_i^{(k,l)} > 0$), the contribution of voxel $i$ to the projection data is deemed high enough to justify an update and the voxel is updated as in (9). Note that requiring $C_i^{(k,l)} > 0$ serves as an extra safety measure in preventing the voxel activity from being updated to zero, which might occur if the voxel's activity estimate is much higher than the actual activity (e.g. activity estimates in early iterations), while there are no measured counts in the detector pixels that occur in its correction term ($C_i^{(k,l)} = 0$). After the update, $T_i^{(k,l)}$, $C_i^{(k,l)}$ and $N_i^{(l)}$ are reset to zero. Furthermore, if voxel $i$ was updated in a certain sub-iteration, but was not updated in all consecutive sub-iterations of the full iteration, $T_i^{(k,l)}$, $C_i^{(k,l)}$ and $N_i^{(l)}$ are carried into the next full iteration until the test passes. However, if a voxel was not updated over a number of sub-iterations equal to $NS^{max}$, an update for that voxel is forced by using detector pixels from all subsets. Thus, the total number of individual voxel updates in a full CROSEM iteration can range from 1 (MLEM-like update) up to $NS^{max}$. With CROSEM, the activity in a voxel can still be updated to zero if none of the detector pixels in all subsets that are associated with that voxel contain any counts. In such case, MLEM would also update the corresponding voxel activity to zero. Since CROSEM automatically reduces the effective NS to update low-activity regions in an image, CROSEM can always be used with a high $NS^{max}$ irrespective of the details of a scan.

To make the CTV independent of the reconstructed voxel size, the CTV is in units of the number of (estimated) counts per milliliter. Before image reconstruction commences, the CTV is scaled to the number of counts per voxel, a number that depends on voxel size. The CTV is closely related to the count levels in the image as it functions as a regulation parameter for the minimum counts that a voxel has to contribute to the projection data before an update of that voxel is performed. Low-count image voxels are less likely to meet this requirement each sub-iteration; only after projection pixels from a number of subsets are added together to form a larger subset this requirement is met. The contribution from a high-activity voxel to each subset of the projection data can be larger than the CTV for every

subset and therefore these voxels can be updated every sub-iteration. To illustrate how CROSEM updates voxels depending on their activity estimate, assume that CROSEM reconstruction is performed on 0.5 mm voxels with the $NS^{max} = 128$ and the $CTV = 40,000$ counts/ml. These reconstruction parameters imply that each voxel has to contribute at least 5 counts to the projection data before it is updated (the volume of a single voxel is 1/8,000 ml; a CTV of 40,000 counts/ml corresponds to a CTV of 5 counts/voxel). As a result, a voxel that contributed ≥5 counts to the projection data of each subset would be updated every sub-iteration , while a voxel that contributed less than 5 counts to the entire projection data would be updated only once every full iteration, thereby using detector pixels from all subsets.

Note that OSEM requires that each voxel is seen by every subset. If not, reconstruction artifacts arise because voxels that are not seen in a certain subset have zero-valued normalization terms in that subset. In most OSEM implementations this is overcome by not updating voxels that have zero-valued normalization terms or by allocating zero activity to these voxels, however these strategies may still result in artifacts. CROSEM inherently prevents these artifacts by its requirement that a voxel must contribute counts to the subset with which it is updated, which implies that normalization terms are never zero.

In this work, OSEM, StatREM and CROSEM were applied with pixel-based subset schemes [21] and StatREM and CROSEM were always operated with $NS^{max} = 128$ subsets. In the remainder of this work, $k$ iterations MLEM is denoted as "$k$it MLEM", $k$ iterations OSEM applied with $L$ subsets as "$k$it OSEM-$L$", $k$ iterations StatREM with a statistical test level $\alpha$ as "$k$it StatREM-$\alpha$" and $k$ iterations CROSEM with a CTV $\beta$ as "$k$it CROSEM-$\beta$".

## 6.2.2 Focusing multi-pinhole SPECT scanner

In this study we used the U-SPECT-II/CT scanner (MILabs B.V., Utrecht, The Netherlands) which is dedicated to ultra-fast, ultra-sensitive and ultra-high-resolution imaging of rodents [17]. It has three large-area gamma cameras (595 x 472 mm NaI(Tl)) and each camera is subdivided into pixels of about 1 mm$^2$. The energy and spatial resolution of these cameras are about 10% and 3.5 mm full-width-at-half-maximum (FWHM), respectively. The cameras are placed in a triangular configuration with a focusing multi-pinhole collimator positioned at the center of the scanner. In the present study a collimator tube for mouse-sized animals was used [17], both for simulations and experiments. The 75 pinholes in this collimator all have an opening angle of 30º and together create a field-of-view (FOV) that encompasses the entire collimator tube diameter (44 mm) and has the shape of an hourglass. A central part of the FOV (CFOV; transaxial diameter 12 mm, axial length 8 mm) is sampled by all pinholes simultaneously and within the CFOV complete data is readily obtained. Imaging of larger volumes is performed by translating the animal through the collimator along a spiral trajectory [24]. Evaluations show that the spatial resolution that can be achieved with this collimator can reach 0.4 mm (0.6 mm pinholes), while <0.3 mm can be achieved when using smaller pinholes. The system matrix $M$ is obtained through PSF measurements,

modeling and interpolations [25]. The image reconstruction algorithm exploits all projections, acquired from all positions of the animal inside the collimator, simultaneously, rather than stitching together reconstructions of sub-volumes that each correspond to a single position of the animal inside the collimator. This method of combined acquisition and reconstruction is called the scanning focus method (SFM, [26]).

## 6.2.3 Digital image quality phantom SPECT simulation

To evaluate the quantitative accuracy and the rate of convergence (the iterative recovery of image features) of MLEM, OSEM, StatREM and CROSEM, SPECT simulations of a digital image quality phantom were performed. The cylindrical phantom was mouse-sized (Fig. 2; diameter 24 mm, length 100 mm) and it contained 5 spheres (diameter 10 mm) filled with different activity concentrations. To simulate both low- and high-count projection data, every consecutive sphere contained a 10 times lower activity concentration (highest for sphere 1, lowest for sphere 5). While such large differences in activity concentration might not commonly occur in a single scan, it may represent count levels from different scans with a large difference in activity concentration and/or scan time (since the number of counts depends on both activity and scan time). The center of each sphere contained a small spherical cold-lesion for contrast measurements (diameter 2 mm, no activity). The activity concentration in the remainder of the phantom was uniform and 10 times lower than the activity concentration inside sphere 5. To mimic a realistic continuous activity distribution, the voxel size of the phantom was 0.15 mm, half the size of the voxels in the reconstructed images.

The fast simulator that was used in this study is based on ray tracing to account for resolution-degrading effects of pinhole diameter and pinhole edge penetration [27, 28]. The radionuclide that was simulated is $^{99m}$Tc (140 keV gamma photons). The intrinsic resolution of the detectors and detection efficiency for 140 keV gamma photons were set in correspondence with experimental data to a Gaussian response with a FWHM of 3.5 mm and a value of 89%, respectively. The simulator was used to simulate noiseless phantom projection data and to pre-calculate the system matrix. From the noiseless projections, 10 noise realizations were created by generating Poisson statistics, taking into account total administered activity and scan duration (57.7 MBq and 60 min respectively, resulting in 19.5M counts in each noise realization).

All noise realizations were reconstructed with MLEM, with OSEM for a range of NS (NS = 16, 32, 64 and 128 subsets), with StatREM for a range of statistical test levels (NS$^{max}$ = 128; statistical test level = 0.01, 0.05, 0.1 and 0.2) and with CROSEM for a range of CTVs (NS$^{max}$ = 128; CTV = 40k, 20k, 10k and 5k counts/ml). All reconstructions were post-filtered with a 3D Gaussian kernel with a FWHM of 0.4 mm.

To evaluate the quantitative accuracy of each algorithm, a mean reconstructed image was determined by averaging images over all noise realizations. From this mean image longitudinal image slices through the transaxial centers of the spheres were made.

Furthermore, reconstructed activities inside 11 mm diameter spherical volumes-of-interest (VOIs; centered on the spheres) were determined in each of the noise realizations. This resulted in a mean and standard deviation of the reconstructed activity in each sphere, expressed in terms of percentage reconstructed activity relative to the true sphere activity.

To assess differences in iterative convergence speed and compare contrast and noise characteristics between the algorithms, cold-lesion contrast and noise were calculated. The average contrast inside a sphere at iteration $k$ was defined to be the cold-lesion contrast at that iteration averaged over all noise realizations, with the contrast in noise realization $r$ at iteration $k$ being defined as:

$$\text{Contrast}^{(r,k)} = \frac{\left\langle A_{hot}^{(r,k)} \right\rangle - \left\langle A_{cold}^{(r,k)} \right\rangle}{\left\langle A_{hot}^{(r,k)} \right\rangle} \tag{13}$$

Here $\left\langle A_{cold}^{(r,k)} \right\rangle$ is the average reconstructed activity per voxel inside a 1 mm diameter spherical VOI centered on the cold-lesion and $\left\langle A_{hot}^{(r,k)} \right\rangle$ is the average reconstructed activity per voxel in a spherical annulus surrounding the cold-lesion (inner and outer diameter 4 mm and 8 mm respectively).

As a measure of the noise in each sphere, the normalized standard deviation inside the cold-lesion region was averaged over all noise realizations, with the noise in noise realization $r$ at iteration $k$ being defined as:

$$\text{Noise}^{(r,k)} = \frac{1}{\left\langle A_{cold}^{(r,k)} \right\rangle} \sqrt{\frac{\sum_{q=1}^{Q} (A_{cold}^{(r,k)}(q) - \left\langle A_{cold}^{(r,k)} \right\rangle)^2}{Q-1}} \tag{14}$$

Here $A_{cold}^{r,k}(q)$ is the reconstructed activity in voxel $q$ inside the cold-lesion VOI, which consisted of $Q$ voxels. If due to reconstruction artifacts (i.e. erasure of activity) contrast and/or noise for one of the spheres could not be calculated, contrast and/or noise for that sphere were defined to be zero.
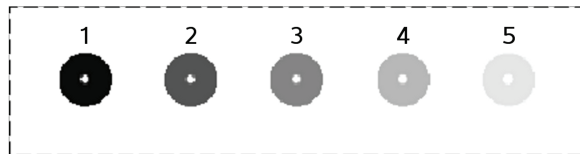


**Figure 2**. *Longitudinal slice through center of digital image quality phantom containing 5 activity-filled spheres (diameter = 10 mm) with spherical cold-lesions (diameter = 2 mm) at their centers. Each consecutive sphere contains a factor 10 lower activity. Image is presented on log-grayscale.*

## 6.2.4 In vivo SPECT

To illustrate the performance of CROSEM on experimental data, *in vivo* data was reconstructed. We compared these reconstructions to MLEM reconstructions (gold standard) and also performed OSEM and StatREM reconstructions. Considering the performance of StatREM and CROSEM in the phantom SPECT simulation study, a test level of 0.05 (StatREM) and a CTV of 20k counts/ml (CROSEM) were used and 8 iterations were performed with both algorithms. The number of OSEM iterations at which OSEM reconstructions were compared to MLEM reconstructions was based on the rule of thumb that performing $k$ iterations OSEM with $L$ subsets leads to a resolution and contrast approximately equivalent to applying $k*L$ iterations MLEM [18, 19]. From this rule of thumb follows that 128 MLEM iterations are required to compare MLEM to OSEM with up to 128 subsets (16, 32, 64 and 128 subsets were tested).

### 6.2.4.1 Scan of a Tumor-bearing Mouse

A 20 g male mouse was inoculated in the shoulder with 22R*v1* human prostatic carcinoma cells. The tumor developed for 3 weeks and the mouse was then intravenously injected with 16.7 MBq of a proprietary ^{99m}Tc-prostate-specific-membrane-antigen-targeted (^{99m}Tc-PSMA) radioligand [22]. Four hours post-injection the mouse was sacrificed and a SPECT scan was performed for 32 min. For the generation of the projection data a 20% energy window was set around the ^{99m}Tc-photopeak. Images were reconstructed on 0.375 mm voxels and the images were post-filtered with a 3D Gaussian kernel with a FWHM of 1.0 mm. From these images MIPs, image slices and image slice profiles were generated. Furthermore, VOIs were selected for the kidneys and the tumor from the MLEM reconstructed image. Using these VOIs reconstructed activities were determined in the OSEM, StatREM and CROSEM images, expressed as percentages of the activities that were reconstructed with MLEM. This experiment was conducted in accordance with Purdue University Animal Care and Use Committee guidelines.

### 6.2.4.2 Bone-scan of a Mouse

A 30 g male mouse was anesthetized with isoflurane. An amount of 189 MBq ^{99m}Tc-hydroxymethylene diphosphonate (^{99m}Tc-HDP) was injected in the tail vein. Scanning started right before radioligand injection and the mouse was scanned for 60 min in frames of 1 min. Low-count projection data was obtained from the last scan frame using a 25% energy window set around the ^{99m}Tc-photopeak. Images were reconstructed on 0.4 mm voxels and the images were post-filtered with a 3D Gaussian kernel with a FWHM of 1.0 mm. From the same scan, projection data containing more counts was obtained by summing the projection data of the final 50 min of the scan. Images from this high-count data were reconstructed on 0.2 mm voxels and the images were post-filtered with a 3D Gaussian kernel with a FWHM of 0.4 mm. For all reconstructions MIPs were generated. Furthermore, VOIs were selected for the bladder

and a section of the spine from the MLEM reconstructed images. Using these VOIs reconstructed activities were determined in the OSEM, StatREM and CROSEM images, expressed as percentages of the activities that were reconstructed with MLEM. This experiment was conducted following protocols approved by the Animal Research Committee of the University Medical Center Utrecht.

## *6.3 Results*

### 6.3.1 Digital Image Quality Phantom SPECT Simulation

Figure 3 shows longitudinal slices (thickness: 1.2 mm) through the mean reconstructed phantom images (average over 10 noise realizations) for (a) MLEM, (b) OSEM, (c) StatREM and (d) CROSEM. The MLEM reconstructed image is shown for 128 iterations, OSEM reconstructions are shown at an iteration number approximately equivalent to 128 MLEM iterations and both StatREM and CROSEM reconstructions are shown for iteration #8. To adequately visualize all spheres with strongly varying activity between them, the spheres are displayed one by one with a different grayscale for each sphere.

For MLEM as well as for all tested CROSEM reconstructions, all spheres were clearly visible. However, OSEM reconstructions increasingly deviated from MLEM as the NS increased; more and more activity in spheres 4 and 5 was erased until their activity completely disappeared in the reconstruction with 128 subsets. For all tested StatREM reconstructions spheres 1 to 4 were clearly visible, but the reconstructions of sphere 5 showed considerable artifacts as activity in many voxels was erased in the reconstructions of the individual noise realizations, although these artifacts were found to be not as severe as in the OSEM reconstructions.

Table 1 shows for each algorithm the percentage of reconstructed activity in spheres 1 to 5 relative to the true activity. All algorithms recovered >95% of the activity in spheres 1, 2 and 3. For sphere 4, MLEM still performed well in quantifying the activity and CROSEM performed almost as well for all tested CTVs. OSEM showed increasing quantification errors for reconstruction with an increasing NS. StatREM preformed approximately as good as CROSEM, except for the strictest (lowest) test level. For sphere 5, MLEM and CROSEM still performed very similar in terms of quantification, whereas all of the tested OSEM reconstructions performed significantly worse; for OSEM-32, OSEM-64 and OSEM-128 even all activity was erased. All tested StatREM reconstructions showed severe quantification errors in terms of large standard deviations, which increased with less strict (higher) test levels. For the lowest and highest test level not only high standard deviations were observed but also large errors in mean reconstructed activity. These results indicate that for quantification of activity, CROSEM performs significantly better than OSEM and StatREM and that CROSEM almost matches MLEM.
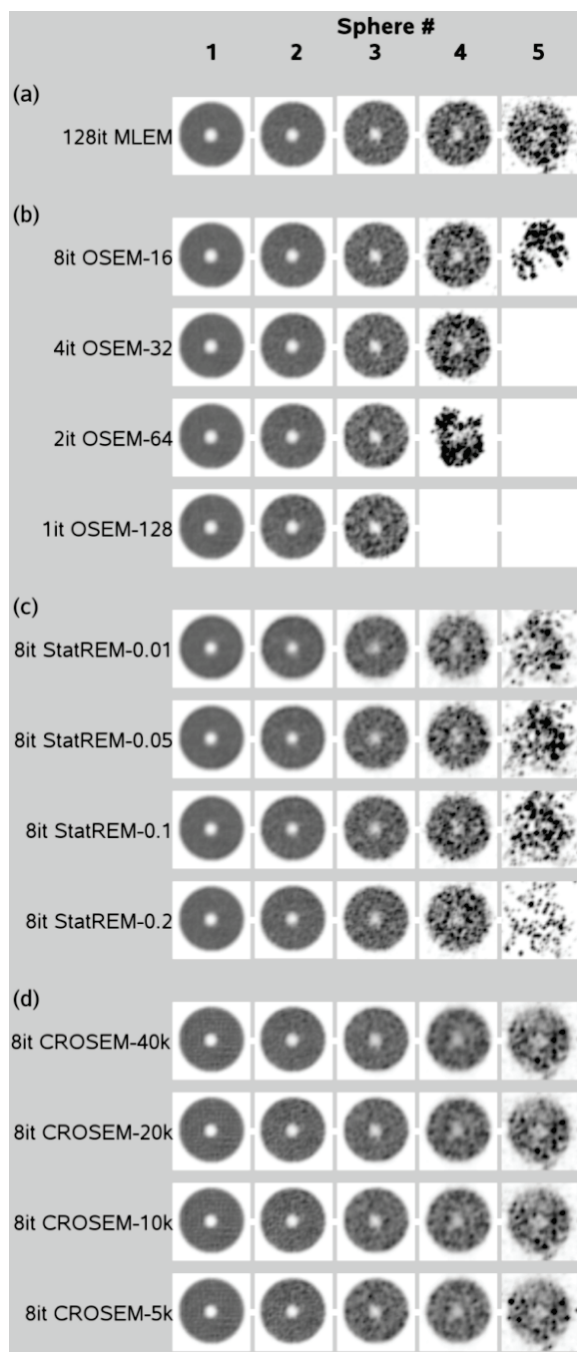
**Figure 3**. *Reconstructions (average over 10 noise realizations) of simulated image quality phantom scan (57.7 MBq $^{99m}$Tc, 60 min scan time). Longitudinal image slices through centers of spheres (different grayscale per sphere) for (a) MLEM, (b) OSEM, (c) StatREM and (d) CROSEM.*

**TABLE I**. Reconstructed activities (% of gold standard)

| Algorithm | Sphere #  1 | 2 | 3 | 4 | 5 |
|---|---|---|---|---|---|
| 128it MLEM | 99.8±0.0 | 99.9±0.1 | 99.7±0.3 | 99.4±1.2 | 88.6±2.5 |
| 8it OSEM-16 | 99.8±0.1 | 99.8±0.3 | 99.3±1.2 | 99.1±3.0 | 72.4±7.3 |
| 4it OSEM-32 | 99.8±0.2 | 100.0±0.5 | 98.9±1.3 | 101.3±4.4 | 0.0±0.0 |
| 2it OSEM-64 | 99.8±0.2 | 99.9±0.5 | 98.4±2.0 | 77.6±4.7 | 0.0±0.0 |
| 1it OSEM-128 | 99.9±0.3 | 100.0±0.7 | 99.9±2.8 | 0.0±0.0 | 0.0±0.0 |
| 8it StatREM-0.01 | 99.9±0.0 | 99.5±0.1 | 96.5±0.3 | 86.9±0.8 | 68.8±9.1 |
| 8it StatREM-0.05 | 99.9±0.0 | 99.8±0.1 | 98.3±0.2 | 95.0±1.0 | 82.1±10.4 |
| 8it StatREM-0.1 | 100.0±0.0 | 100.0±0.1 | 99.4±0.3 | 98.6±1.7 | 85.3±14.0 |
| 8it StatREM-0.2 | 100.0±0.0 | 100.3±0.1 | 100.6±0.4 | 94.5±2.8 | 41.1±14.4 |
| 8it CROSEM-40k | 99.9±0.3 | 99.6±0.4 | 98.2±0.5 | 96.7±1.1 | 85.8±2.2 |
| 8it CROSEM-20k | 99.9±0.3 | 99.8±0.4 | 98.0±0.8 | 97.1±1.2 | 85.6±2.3 |
| 8it CROSEM-10k | 99.9±0.3 | 99.8±0.6 | 97.8±1.1 | 96.1±1.6 | 84.8±2.4 |
| 8it CROSEM-5k | 100.0±0.3 | 99.9±0.6 | 97.9±1.4 | 94.4±2.3 | 84.7±2.6 |

Figure 4 shows average contrast versus average noise (average over 10 noise realizations) inside sphere 1 and sphere 5 for OSEM, StatREM and CROSEM. The graphs also display the corresponding MLEM curves (solid lines).

For OSEM, contrast and noise characteristics inside sphere 1 were found to be comparable to MLEM (Fig. 4a). The contrast recovery speed-up of OSEM over MLEM in sphere 1 was found to be approximately equal to the NS, which can be deduced from the MLEM and OSEM iteration numbers at approximately equal contrast and noise which are also displayed in the figure. For sphere 5, all OSEM reconstructions showed large artifacts and the average noise could therefore not be calculated and was defined to be zero (Fig. 4b). Furthermore, because of these artifacts all OSEM reconstructions resulted in zero contrast, except for OSEM-16 where an unrealistically high contrast was calculated. Figure 4b only shows the first iteration for each tested OSEM since contrast-noise characteristics did not improve at later iterations.

For sphere 1, all tested StatREM reconstructions resulted in a lower contrast than MLEM at approximately equal noise levels (Fig. 4c). It can also be seen that higher (less strict) test levels resulted in faster convergence in high-activity regions: e.g. 23it StatREM-0.01, 15it StatREM-0.05, 13it StatREM-0.1 and 10it StatREM-0.2 were required to obtain a contrast and noise level approximately equivalent to 384it MLEM. For all test levels of StatREM, activities in many voxels of sphere 5 were erased in individual noise realizations and the average noise could therefore not be calculated and was defined to be zero (Fig. 4d). Furthermore, negative contrasts were found for some test levels of StatREM, because in some of the noise realizations the average activity in the cold lesion was higher than the average activity in the hot region. Figure 4d only shows the first iteration for each test level of StatREM since contrast-noise characteristics did not improve at later iterations. For CROSEM, contrast and noise characteristics inside sphere 1 were found to be comparable to MLEM (Fig. 4e). CROSEM attained high speed-up over MLEM for sphere 1: e.g. 4it CROSEM-40k,

2it CROSEM-20k, 2it CROSEM-10k and 2it CROSEM-5k resulted in a contrast and noise level approximately equivalent to 128it MLEM (Note that the first CROSEM iteration was an ordinary MLEM iteration so there was no speed-up over MLEM in this iteration). It can also be seen that a lower CTV resulted in faster convergence in high-activity regions: e.g. 13it CROSEM-40k, 8it CROSEM-20k, 5it CROSEM-10k and 4it CROSEM-5k were required to obtain a contrast and noise level approximately equivalent to 384it MLEM. For sphere 5 (Fig. 4f), CROSEM-40k and CROSEM-20k behaved approximately MLEM-like in terms of contrast and noise characteristics and speed, although their contrast at higher iterations was slightly worse than MLEM. CROSEM operated with CTVs lower than 20k counts/ml behaved approximately MLEM-like in early iterations, however at higher iterations more iterations than MLEM were required to arrive at a similar contrast-noise as MLEM, which indicates that these CTVs are suboptimal (e.g. 41it CROSEM-10k resulted in a similar contrast-noise as 24it MLEM). Figure 4e-f clearly illustrate that CROSEM achieves a local contrast-noise tradeoff: CROSEM attained high speed-up factors over MLEM inside high-activity regions (sphere 1) and at the same time no speed-up over MLEM in very low-activity regions (sphere 5): 8it CROSEM-20k resulted in a contrast and noise equivalent to 384it MLEM inside sphere 1 and resulted in a contrast and noise equivalent to 8it MLEM inside sphere 5.

These results indicate that CROSEM (for CTVs $\geq$ 20k counts/ml) can achieve very high speed-up over MLEM and that CROSEM is comparable to MLEM in terms of local contrast and noise characteristics, whereas OSEM and StatREM resulted in severe reconstruction artifacts in low-activity regions.
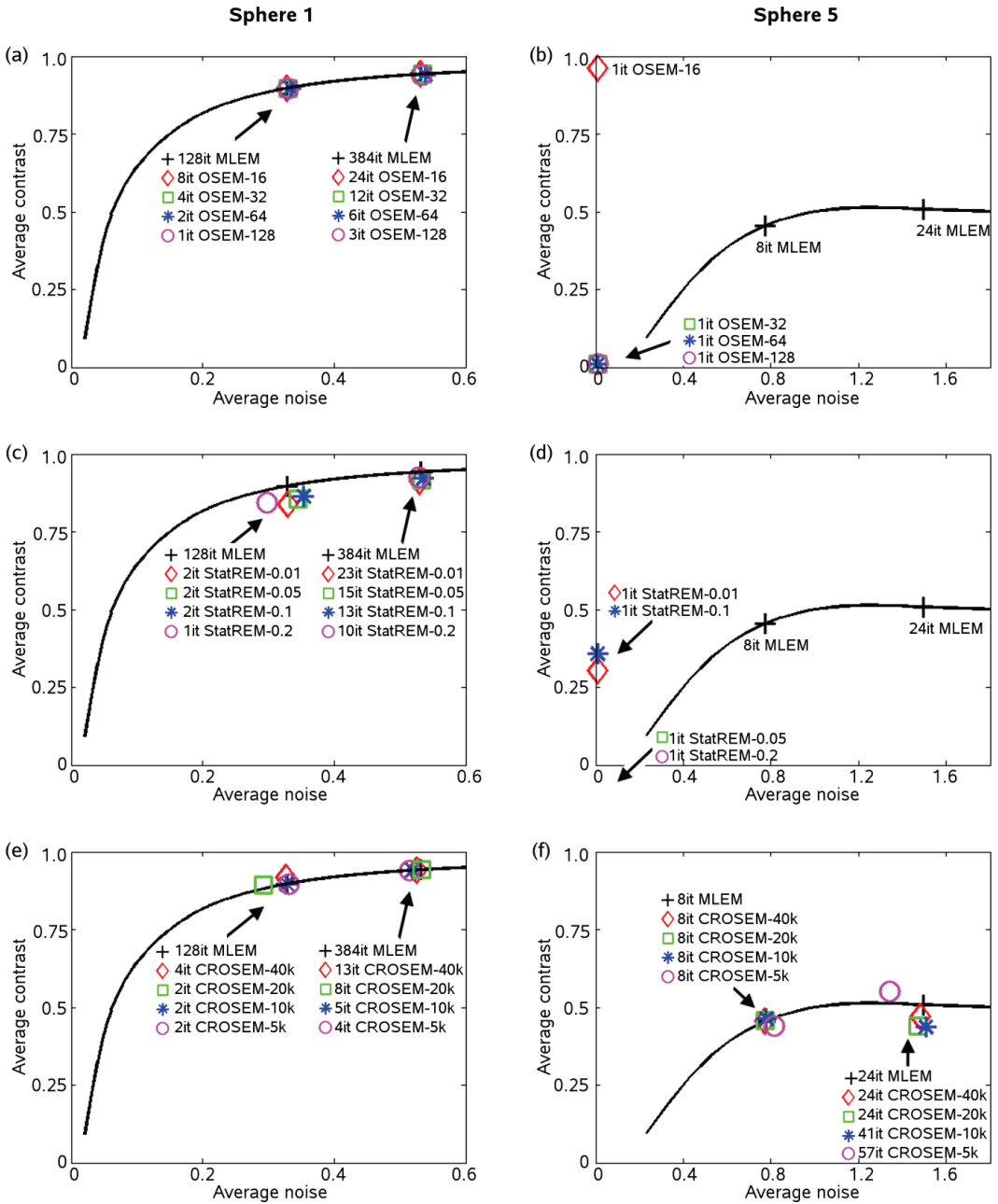
**Figure 4**. *Graphs of average contrast vs. average noise (average over 10 noise realizations) in sphere 1 (left graphs) and sphere 5 (right graphs) for (a,b) OSEM, (c,d) StatREM and (e,f) CROSEM. The graphs also show corresponding MLEM curves (solid lines).*

## 6.3.2 In vivo SPECT

### 6.3.2.1 Scan of a tumor-bearing mouse

Fig. 5 shows the reconstructed SPECT images of a tumor-bearing mouse for (a) MLEM, (b) OSEM, (c) StatREM and (d) CROSEM. Similar to the phantom studies discussed above, activity in more and more voxels was being erased in OSEM reconstructions as the NS increased: for OSEM-128 activity inside the kidneys and tumor even completely disappeared. The image profiles (thickness and width: 1.875 mm) clearly show deviations between MLEM (dashed black line) and OSEM (solid magenta lines), which became larger for an increase in the NS. The StatREM-0.05 image and profile are much closer to the MLEM image and profile, although the MIP looks noisier and the profile deviates in some places. The MIP of the CROSEM-20k reconstruction appears to be less noisy than the one of StatREM-0.05 and the profile of CROSEM-20k almost perfectly matches the one of MLEM.

Table 2 shows the percentages of reconstructed activity in the kidneys and the tumor (VOIs indicated in Fig. 5a) obtained with OSEM, StatREM-0.05 and CROSEM-20k relative to the activities obtained with MLEM. StatREM-0.05 and CROSEM-20k show the smallest deviations from MLEM, while for OSEM the deviations from MLEM increased for an increase in the NS.

**TABLE II**. Reconstructed activities (% of 128it MLEM-reconstructed activities)

| Algorithm | Kidneys | Tumor |
|---|---|---|
| 8it OSEM-16 | 102.4 | 97.4 |
| 4it OSEM-32 | 102.8 | 86.5 |
| 2it OSEM-64 | 92.3 | 0.0 |
| 1it OSEM-128 | 0.0 | 0.0 |
| 8it StatREM-0.05 | 98.3 | 102.0 |
| 8it CROSEM-20k | 98.8 | 98.4 |
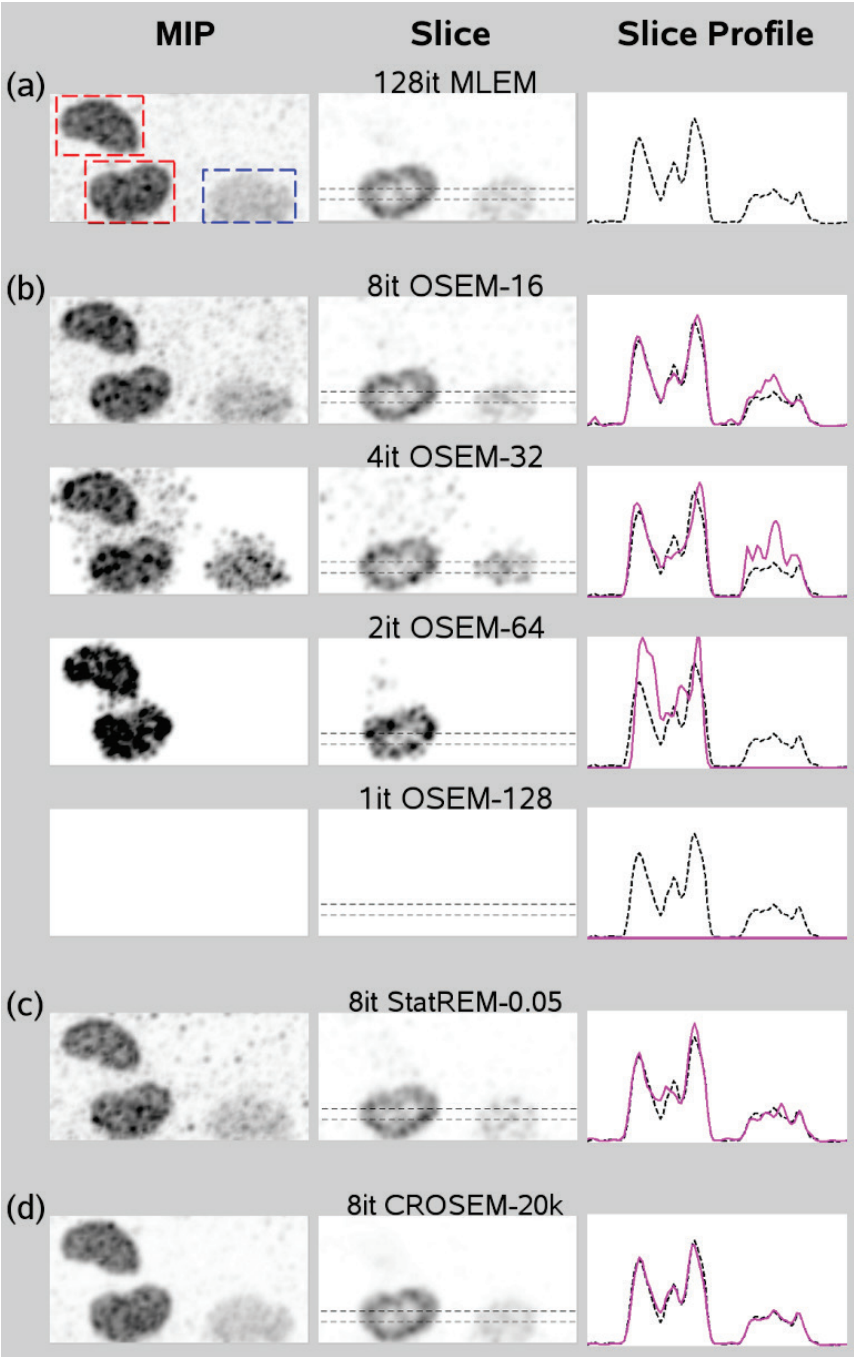
**Figure 5**. *MIPs, slices and profiles of same SPECT scan as shown in Fig 1. Image profiles of (a) MLEM (dashed black line) are compared to (b) OSEM, (c) StatREM-0.05 and (d) CROSEM-20k (solid magenta lines): CROSEM-20k deviates very little from MLEM. MIP in (a) indicates VOIs for kidneys (red) and tumor (blue).*

### 6.3.2.2 Bone-scan of a Mouse

Figure 6 shows the results for 1-min and 50-min mouse bone-scan reconstructions with (a) MLEM, (b) OSEM, (c) StatREM and (d) CROSEM. For the OSEM reconstructions of the 1-min scan (Fig. 6b, left) large parts of the image were erased as the NS increased: in the image that was reconstructed with OSEM-128 only high-activity regions of the liver and bladder had nonzero activity. StatREM-0.05 resulted in a very noisy reconstruction and bony structures are only vaguely visible (Fig. 6c, left). In contrast, CROSEM-20k clearly shows all structures that are visible in the MLEM image (Fig. 6d, left).

The OSEM reconstructions of the 50-min scan (Fig. 6b, right) also show artifacts as the NS increased; the MIPs look increasingly noisy and again activity in parts of the OSEM-128 image was erased (e.g. parts of the jaw and tail), although these artifacts were not as severe as in the OSEM reconstructions of the 1-min scan. The StatREM-0.05 reconstruction (Fig. 6c, right) looks very similar to the one of MLEM. The CROSEM-20k reconstruction (Fig. 6d, right) shows a high level of detail in high-activity regions and less noisy low-activity regions compared to MLEM.

Table 3 shows the percentages of reconstructed activities in the bladder and a part of the spine (VOIs are indicated in Fig. 6a) relative to the activities obtained with 128it MLEM for the 1-min and 50-min acquisitions. For the 1-min scan reconstructions OSEM increasingly underestimated the activity in the spinal region as the NS increased, while for the 50-min scan all tested OSEM performed similar to MLEM. For the 1-min scan reconstruction, StatREM-0.05 resulted in underestimation of the activity in the spine by about 10%, while for the 50-min scan StatREM-0.05 deviated little from MLEM. For the 1-min scan, CROSEM-20k underestimated the activities maximally about 5%, while for the 50-min scan CROSEM-20k recovered about the same activity as MLEM.

**TABLE III**. Reconstructed activities (% of 128it MLEM-reconstructed activities)

| Algorithm | 1-min scan | | 50-min scan | |
|---|---|---|---|---|
| | Bladder | Spine | Bladder | Spine |
| 8it OSEM-16 | 99.5 | 88.3 | 100.0 | 101.0 |
| 4it OSEM-32 | 99.3 | 40.9 | 100.1 | 101.1 |
| 2it OSEM-64 | 99.9 | 11.3 | 100.6 | 101.4 |
| 1it OSEM-128 | 89.3 | 0.0 | 98.4 | 104.3 |
| 8it StatREM-0.05 | 98.8 | 89.6 | 99.1 | 98.0 |
| 8it CROSEM-20k | 96.3 | 94.7 | 98.5 | 100.4 |

**Figure 6**. *MIPs of mouse bone-scan reconstructions (189 MBq $^{99m}$Tc-HDP) of 1-min (left) and 50-min (right) scans for **(a)** MLEM, **(b)** OSEM, **(c)** StatREM-0.05 and **(d)** CROSEM-20k. Right MIP in (a) indicates VOIs for bladder (red) and spine (blue).*

## *6.4 Discussion*

In this study we have shown that CROSEM applied with a single setting of the reconstruction parameters ($NS^{max}$ and CTV) achieves high image resolution in highly active regions while still yielding quantitatively accurate images in regions with low activity uptake. In this study we have also shown that OSEM reconstruction could result in major reconstruction artifacts in regions with low activity and that these artifacts become more severe as the NS increases. Although StatREM generally outperformed OSEM in terms of quantifying activity in low-activity regions, we still found significant reconstruction artifacts in low-activity regions.

With CROSEM, the number of voxel updates is nonuniform over the image because it depends on the reconstructed activity distribution and, as a result, a spatially variant regularization is imposed: high-activity regions tend to recover more spatial resolution and contrast to better match the measured projections, whereas a high resolution cannot be achieved in low-activity regions and therefore less updates, resulting in more smoothness, can be preferable in these regions to avoid amplification of noise. However, users need to be aware of nonuniform spatial resolution since this could introduce errors into quantitative comparisons since partial volume effects will depend on local activity levels.

In this study we tested CROSEM for image reconstruction of SPECT data. In general, PET has higher sensitivity than SPECT and low-count induced OSEM artifacts may therefore be less important in PET. On the other hand, dose reduction in PET is still desirable and many new screening protocols or longitudinal studies would come into reach when very low-dose PET can be performed. We believe that for such low-dose PET (or dynamic PET studies with low counts per time frame) CROSEM may also improve contrast-noise characteristics over OSEM. Furthermore, as long as CROSEM is operated with balanced subsets, we see no reason why CROSEM could not be applied with (traditional) projection-based subsets that are mostly used in clinical SPECT and PET.

The extra reconstruction time that is needed for a full CROSEM iteration over an MLEM iteration is small; e.g., the reconstruction time of the mouse bone-scan acquired over 1 min (voxel size: 0.4 mm) was 1.5 min per iteration for MLEM (performed on 4 AMD processors using in total 16 cores; Opteron 6174, 2.19 GHz), while CROSEM required only < 15 s extra time per full iteration. Note that this is extra time per iteration and that CROSEM requires many fewer iterations than MLEM to achieve a high resolution in highly active image regions.

Besides CROSEM, other accelerated reconstruction algorithms may also prevent erasure of low-activity image regions. One way to accelerate reconstruction and prevent activity erasure is by applying a power factor in the MLEM update step to obtain an accelerated MLEM algorithm [29]. However, the speed-up of this algorithm over MLEM is still limited. There are also convergent OS methods which can be divided into relaxed- and incremental OS methods. A well-known relaxed OS algorithm is RAMLA [30]. RAMLA uses relaxation within a modified version of OSEM. Since there are no general rules for finding relaxation schedules that result in high reconstruction speed-up factors over MLEM, a

separate optimization study is required, and a comparison between the performance of optimized RAMLA and optimized CROSEM remains a topic for future research. A well-known incremental OS algorithm is COSEM [31]. COSEM does not require a user-specified and object-dependent relaxation schedule; however, the speed-up of COSEM lies between MLEM and optimized RAMLA. Faster convergence may be achieved by starting with OSEM and switching to a convergent OS algorithm at later iterations. However, for low-count (multi-pinhole) SPECT, a relatively low number of subsets can already result in activity erasure in a large fraction of the voxels.

## *6.5 Conclusions*

CROSEM is a fast and stable alternative to OSEM that prevents excessive image noise and quantitative errors in low-activity regions while achieving high resolution recovery in structures with high activity uptake. A single setting of the reconstruction parameters ($NS^{max}$ and CTV) leads to images with high resolution where possible and good quantitative accuracy for all imaging studies presented here in which we covered a wide range of doses and activity distributions. In addition our results clearly indicate that CROSEM can help prevent users having to compromise between resolution and quantitative accuracy.

## *Bibliography*

[1]    F. J. Beekman, H. W. A. M. De Jong, and S. Van Geloven, "Efficient fully 3-D iterative SPECT reconstruction with Monte Carlo-based scatter compensation," *IEEE Trans. Med. Imag.,* vol. 21, no. 8, pp. 867-877, 2002.

[2]    B. F. Hutton, H. M. Hudson, and F. J. Beekman, "A clinical perspective of accelerated statistical reconstruction," *Eur. J. Nucl. Med.,* vol. 24, no. 7, pp. 797-808, 1997.

[3]    R. Leahy, and C. Byrne, "Recent developments in iterative image reconstruction for PET and SPECT," *IEEE Trans. Med. Imag.,* vol. 19, no. 4, pp. 257-260, 2000.

[4]    R. M. Leahy, and J. Y. Qi, "Statistical approaches in quantitative positron emission tomography," *Stat. Comput.,* vol. 10, no. 2, pp. 147-165, 2000.

[5]    J. Qi, and R. M. Leahy, "Iterative reconstruction techniques in emission computed tomography," *Phys. Med. Biol.,* vol. 51, no. 15, pp. R541-78, 2006.

[6]    F. J. Beekman, and C. Kamphuis, "Ordered subset reconstruction for x-ray CT," *Phys. Med. Biol.,* vol. 46, no. 7, pp. 1835-1844, 2001.

[7]    B. De Man, J. Nuyts, P. Dupont, G. Marchal, and P. Suetens, "An iterative maximum-likelihood polychromatic algorithm for CT," *IEEE Trans. Med. Imag.,* vol. 20, no. 10, pp. 999-1008, 2001.

[8]     H. Erdogan, and J. A. Fessler, "Ordered subsets algorithms for transmission tomography," *Phys. Med. Biol.,* vol. 44, no. 11, pp. 2835-51, 1999.

[9]     J. S. Kole, and F. J. Beekman, "Evaluation of the ordered subset convex algorithm for cone-beam CT," *Phys. Med. Biol.,* vol. 50, no. 4, pp. 613-23, 2005.

[10]    S. H. Manglos, G. M. Gagne, A. Krol, F. D. Thomas, and R. Narayanaswamy, "Transmission maximum-likelihood reconstruction with ordered subsets for cone-beam CT," *Phys. Med. Biol.,* vol. 40, no. 7, pp. 1225-1241, 1995.

[11]    J. Nuyts, B. De Man, P. Dupont, M. Defrise, P. Suetens, and L. Mortelmans, "Iterative reconstruction for helical CT: a simulation study," *Phys. Med. Biol.,* vol. 43, no. 4, pp. 729-737, 1998.

[12]    W. Zbijewski, and F. J. Beekman, "Efficient Monte Carlo based scatter artifact reduction in cone-beam micro-CT," *IEEE Trans. Med. Imag.,* vol. 25, no. 7, pp. 817-27, 2006.

[13]    W. Zbijewski, M. Defrise, M. A. Viergever, and F. J. Beekman, "Statistical reconstruction for x-ray CT systems with non-continuous detectors," *Phys. Med. Biol.,* vol. 52, no. 2, pp. 403-18, 2007.

[14]    K. Lange, and R. Carson, "EM reconstruction algorithms for emission and transmission tomography," *J. Comput. Assist. Tomogr.,* vol. 8, pp. 306-316, 1984.

[15]    L. A. Shepp, and Y. Vardi, "Maximum likelihood reconstruction for emission tomography," *IEEE Trans. Med. Imag.,* vol. 1, no. 2, pp. 113-22, 1982.

[16]    B. F. Hutton, I. Buvat, and F. J. Beekman, "Review and current status of SPECT scatter correction," *Phys. Med. Biol.,* vol. 56, no. 14, pp. R85-112, 2011.

[17]    F. Van der Have, B. Vastenhouw, R. M. Ramakers, W. Branderhorst, J. O. Krah, C. Ji, S. G. Staelens, and F. J. Beekman, "U-SPECT-II: An Ultra-High-Resolution Device for Molecular Small-Animal Imaging," *J. Nucl. Med.,* vol. 50, no. 4, pp. 599-605, 2009.

[18]    H. M. Hudson, and R. S. Larkin, "Accelerated image-reconstruction using ordered subsets of projection data," *IEEE Trans. Med. Imag.,* vol. 13, no. 4, pp. 601-609, 1994.

[19]    C. Kamphuis, F. J. Beekman, and M. A. Viergever, "Evaluation of OS-EM vs ML-EM for 1D, 2D and fully 3D SPECT reconstruction," *IEEE Trans. Nucl. Sci.,* vol. 43, no. 3, pp. 2018-2024, 1996.

[20]    D. S. Lalush, and B. M. Tsui, "Performance of ordered-subset reconstruction algorithms under conditions of extreme attenuation and truncation in myocardial SPECT," *J. Nucl. Med.,* vol. 41, no. 4, pp. 737-44, 2000.

[21]    W. Branderhorst, B. Vastenhouw, and F. J. Beekman, "Pixel-based subsets for rapid multi-pinhole SPECT reconstruction," *Phys. Med. Biol.,* vol. 55, no. 7, pp. 2023-34, 2010.

[22]    S. A. Kularatne, Z. Zhou, J. Yang, C. B. Post, and P. S. Low, "Design, synthesis, and preclinical evaluation of prostate-specific membrane antigen targeted (99m)Tc-radioimaging agents," *Mol. Pharm.,* vol. 6, no. 3, pp. 790-800, 2009.

[23]    D. J. Kadrmas, "Statistically regulated and adaptive EM reconstruction for emission computed tomography," *IEEE Trans. Nucl. Sci.,* vol. 48, no. 3, pp. 790-798, 2001.

[24]    P. E. B. Vaissier, M. C. Goorden, B. Vastenhouw, F. van der Have, R. M. Ramakers, and F. J. Beekman, "Fast spiral SPECT with stationary gamma-cameras and focusing pinholes," *J. Nucl. Med.,* vol. 53, no. 8, pp. 1292-9, 2012.

[25]    F. Van der Have, B. Vastenhouw, M. Rentmeester, and F. J. Beekman, "System calibration and statistical image reconstruction for ultra-high resolution stationary pinhole SPECT," *IEEE Trans. Med. Imag.,* vol. 27, no. 7, pp. 960-71, 2008.

[26]    B. Vastenhouw, and F. Beekman, "Submillimeter total-body murine imaging with U-SPECT-I," *J. Nucl. Med.,* vol. 48, no. 3, pp. 487-93, 2007.

[27]    M. Gieles, H. W. de Jong, and F. J. Beekman, "Monte Carlo simulations of pinhole imaging accelerated by kernel-based forced detection," *Phys. Med. Biol.,* vol. 47, no. 11, pp. 1853-67, 2002.

[28]    M. C. Goorden, F. Van der Have, R. Kreuger, and F. J. Beekman, "An efficient simulator for pinhole imaging of PET isotopes," *Phys. Med. Biol.,* vol. 56, no. 6, pp. 1617-34, 2011.

[29]    D. Hwang, and G. L. Zeng, "Convergence study of an accelerated ML-EM algorithm using bigger step size," *Phys. Med. Biol.,* vol. 51, no. 2, pp. 237-252, 2006.

[30]    J. Browne, and A. R. De Pierro, "A row-action alternative to the EM algorithm for maximizing likelihoods in emission tomography," *IEEE Trans. Med. Imag.,* vol. 15, no. 5, pp. 687-699, 1996.

[31]    I. T. Hsiao, A. Rangarajan, P. Khurd, and G. Gindi, "An accelerated convergent ordered subsets algorithm for emission tomography," *Phys. Med. Biol.,* vol. 49, no. 11, pp. 2145-56, 2004.

# 7. Regulated OSEM reconstruction and its application to pinhole emission tomography

P. E. B. Vaissier, M. C. Goorden, and F.J. Beekman. "Regulated OSEM reconstruction and its application to pinhole emission tomography," in preparation.

## *Abstract*

Ordered Subsets Expectation Maximization (OSEM) is widely used to accelerate tomographic reconstruction. Speed-up of OSEM over Maximum Likelihood Expectation Maximization (MLEM) is close to the number of subsets in which the projection data is divided. Although a high number of subsets is desired to prevent prohibitively long reconstructions, a high number of subsets can cause severe quantitative inaccuracies or even disappearance of tissue with low activity from images. To overcome such problems, we recently introduced Count-Regulated OSEM (CR-OSEM). It was shown that for pinhole SPECT, CR-OSEM prevents erasure of activity in regions with low-activity, displays fast contrast recovery in high-activity regions, while contrast and noise in low-activity regions remain relatively low. In this work we extend the validation of CR-OSEM to the reconstruction of pinhole-collimated imaging of both SPECT and PET tracers. We show that reconstruction speed of CR-OSEM in image regions with low-activity can sometimes still be rather slow. Moreover, at higher iterations contrast does not always reach the same level as is reached with MLEM after many iterations. To overcome these problems we introduce Similarity-Regulated OSEM (SR-OSEM). Like CR-OSEM, SR-OSEM also shows high reconstruction speed-up over MLEM in high-activity regions. However, in regions with lower activity SR-OSEM generally displays significantly higher reconstruction speeds than CR-OSEM, in some cases an order of magnitude higher. Cases of compromised performance with respect to contrast recovery with CR-OSEM were not observed with SR-OSEM. We conclude that SR-OSEM is fast and can be used with a single setting of reconstruction parameters for image reconstruction in pinhole emission tomography.

## 7.1 Introduction

Statistical iterative image reconstruction methods gain increasing interest for the reconstruction of Single Photon Emission Computed Tomography (SPECT) and Positron Emission Tomography (PET) images [1-5]. In contrast to analytic reconstruction methods, like filtered back-projection, iterative methods allow for accurate modeling of the physical detection process and for application to complex scanner geometries like those found in multi-pinhole SPECT. An important standard for statistical iterative reconstruction in emission tomography is the Maximum Likelihood Expectation Maximization algorithm (MLEM, [6, 7]), mostly due to its consistent and predictable convergence behavior, non-negativity constraint and ease of implementation.

Despite these desirable properties, the widespread application of MLEM in medical image reconstruction is hampered by its computational cost. MLEM has a slow convergence speed, which means that many iterations are required to obtain an acceptable image. Moreover, with increasingly refined models of photon transport and scanners that can achieve higher spatial resolutions, the size of system matrices that describe photon transport also increases over time, which lengthens the reconstruction time per iteration. Therefore, additional computational power may be largely used to compensate for the increased demands of photon transport modeling. In order to shorten reconstruction times block-iterative methods were introduced. With these methods, an iteration of the algorithm is subdivided into a number of subsequent sub-iterations. Each sub-iteration uses a different subset of the projection data to find a new estimate of the activity distribution. A widely used block-iterative version of MLEM is the Ordered Subsets Expectation Maximization algorithm (OSEM, [8]). Despite the absence of convergence, OSEM has shown to very often yield almost the same reconstructed images as MLEM if the number of subsets is not too high [9, 10]. In such cases, the acceleration factor of OSEM over MLEM in terms of resolved image resolution is roughly proportional to the number of subsets [8, 9].

Traditionally, subsets are selected in such a way that each subset contains a number of complete SPECT projections. However, it can be more advantageous to use subset schemes in which each subset contains detector pixels from all projections (Pixel-based OSEM; POSEM, [11]). This way, the requirement that OSEM is operated with balanced subsets (i.e. each subset is equally sensitive to a particular voxel) can still be met for higher numbers of subsets compared to traditional OSEM. As a result, for a sufficiently high number of detected photons, POSEM can reach acceleration factors that are an order of magnitude higher than those of traditional OSEM without significant image degradation [11].

In the case of high-count projection data and strong subset balance, the number of counts in each subset is approximately equal. However, the variance in the number of counts that are contained in different subsets grows if the number of counts in the projections is lower. In projections with fewer counts, the likelihood that all detector pixels in a subset that are associated with a certain voxel have not received any counts increases, even if this voxel contains some activity. As a consequence, the activity in this voxel can be set to zero in the corresponding sub-iteration. Due to the multiplicative nature of the OSEM update, the activity

in this voxel will remain zero, even if other subsets do contain detector pixels with counts that are associated with this particular voxel. As shown in the mouse bone-scan of Fig. 1, this can lead to the permanent erasure of activity. Generally, the chance of generating such an artifact becomes higher if the number of subsets is larger and/or the number of counts in the projections is lower. Apparently obvious solutions, such as only allowing nonzero activity updates or to simply exclude detector pixels that have no counts do not solve the problem but can even lead to more severe reconstruction artifacts as we have demonstrated for pinhole SPECT in [12].
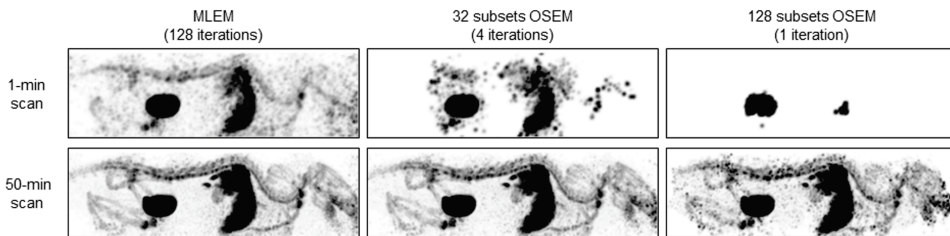


**Figure 1**. *Maximum-intensity-projections (MIPs) of MLEM and OSEM (32 and 128 subsets) reconstructions of mouse bone-scan (189 MBq $^{99m}$Tc-HDP) of 1 min (top row) and 50 min (bottom row). OSEM reconstruction can result in quantitative inaccuracies and even in erasure of activity. The severity of these artifacts strongly depends on the number of counts in the projections and on the number of subsets.*

Erasure of activity from the image can be prevented by using fewer subsets. However, no guideline exists to establish the highest number of subsets that can still be safely used. To minimize the risk of inducing such artifacts one can always select a low number of subsets, but this can lead to too time consuming noisy reconstructions if many iterations are required to reconstruct a high-resolution image. Alternatively, a low number of subsets can lead to a low-resolution image if only a few iterations are performed to save reconstruction time.

In order to prevent erasure of activity by OSEM in case of low count statistics and still enable accelerated image reconstruction in case of higher count statistics, we recently developed a Count-Regulated OSEM algorithm (CR-OSEM; [12]). CR-OSEM uses the concepts of adaptive subset formation and spatially adaptive voxel updates [13]. CR-OSEM applies these concepts by grouping together subsets of subsequent sub-iterations before an update is performed. The number of subsets that are grouped together is voxel-specific and depends on the estimated activity in that voxel. To decide when a specific voxel is updated, CR-OSEM uses a Count Threshold Value (CTV): a voxel is only updated if the estimated number of counts that it has contributed to the subset with which it is updated is larger than the selected CTV. This way, low-activity voxels will not be updated every sub-iteration, rather they are updated fewer times, each time using a larger subset of the projection data. In [12], we validated CR-OSEM for pinhole SPECT of mice in which we covered a large range of activity distributions and numbers of counts. It was found that CR-OSEM could safely be operated with a single setting of the reconstruction parameters (i.e. high number of subsets

and CTV): CR-OSEM prevented erasure of activity in regions with low-activity, while at the same time CR-OSEM could reach speed-up factors over MLEM close to the maximum number of subsets in high-activity regions. In this work we extend our validation of CR-OSEM to the reconstruction of pinhole-collimated imaging of both SPECT and PET tracers (including scatter correction). However, we will show that reconstruction speed of CR-OSEM in image regions with low activity can sometimes still be rather slow. Moreover, after many iterations contrast does not always reach the same level as is reached with MLEM after many iterations.

To overcome drawbacks of CR-OSEM, we here propose Similarity-Regulated OSEM (SR-OSEM). SR-OSEM regulates the amount of individual voxel updates with a different criterion than CR-OSEM. In SR-OSEM, the decision whether or not to update a certain voxel is based on the level of similarity between the update factors for that voxel that are acquired in different subsets. This way, SR-OSEM groups together subsets until a certain level of similarity between the update factors for a certain voxel is reached. The level of similarity is specified by a Similarity Threshold Value (STV). STV is a number between 0% and 100% indicating how much update factors from different subsets are allowed to vary from the corresponding MLEM update factor.

The aim of this work is to introduce and validate SR-OSEM as a fast and safe algorithm that can be used with a single setting of the reconstruction parameters (number of subsets and STV) for image reconstruction in pinhole-collimated emission tomography of SPECT and PET tracers.

## 7.2 Materials and methods

### 7.2.1 Image reconstruction algorithms

Note that in this work OSEM, CR-OSEM and SR-OSEM are all applied with 128 pixel-based subsets.

#### 7.2.1.1 MLEM

An MLEM update of the activity estimate $\widetilde{a}_i^{(k-1)}$ in voxel $i$ at the $k^{\text{th}}$ iteration can be expressed as a multiplication of $\widetilde{a}_i^{(k-1)}$ with an update factor. The update factor consists of a correction factor $C_i^{(k)}$ that is divided by a normalization factor $N_i$ which are defined as:

$$C_i^{(k)} = \sum_j M_{ij} \frac{p_j}{\widetilde{p}_j^{(k)} + s_j}$$

$$\widetilde{p}_j^{(k)} = \sum_i M_{ij} \widetilde{a}_i^{(k-1)} \qquad (1)$$

$$N_i = \sum_j M_{ij}$$

The update equation of MLEM then reads:

$$\widetilde{a}_i^{(k)} = \widetilde{a}_i^{(k-1)} \frac{C_i^{(k)}}{N_i} \qquad (2)$$

In (1), $M_{ij}$ is the system matrix element representing the probability that a non-scattered photon emitted from voxel $i$ is detected in detector pixel $j$. Furthermore, $p_j$ and $\widetilde{p}_j^{(k)}$ are the measured and expected (simulated) number of gamma photon counts in detector pixel $j$ with an energy that lies within the selected photopeak window. The parameter $s_j$ denotes the estimated number of scattered photons within the photopeak window that is detected in detector pixel $j$. For all experiments in this work $s_j$ is obtained by a triple-energy-window technique [14].

### 7.2.1.2 OSEM

OSEM uses the same equations as MLEM to update the image, but for each update only a subset $S_l$ of the detector pixels is used in each sub-iteration $l$ ($1 \leq l \leq L$) of iteration $k$. A single OSEM iteration $k$ is defined to be completed (i.e. full iteration) after all $L$ subsets have been traversed. Correction- and normalization factors for voxel $i$ in sub-iteration $(k,l)$ are defined as:

$$C_i^{(k,l)} = \sum_{j \in S_l} M_{ij} \frac{p_j}{\widetilde{p}_j^{(k,l)} + s_j}$$

$$N_i^{(l)} = \sum_{j \in S_l} M_{ij} \qquad (3)$$

The OSEM image update in sub-iteration $(k,l)$ then reads:

$$\widetilde{a}_i^{(k,l)} = \widetilde{a}_i^{(k,l-1)} \frac{C_i^{(k,l)}}{N_i^{(l)}} \qquad (4)$$

117

### 7.2.1.3 CR-OSEM

CR-OSEM, unlike OSEM, commences with a single MLEM iteration in order to obtain an initial estimate of the activity of individual voxels. Furthermore, while OSEM updates all voxels in each sub-iteration, CR-OSEM only updates a voxel $i$ if a user-specified Count Threshold Value (CTV) is exceeded for that voxel. To this end, CR-OSEM uses the activity estimate of voxel $i$ to estimate the number of counts $\widetilde{e}_i^{(k,l)}$ that voxel $i$ has contributed to the detector pixels of the current subset $S_l$:

$$\widetilde{e}_i^{(k,l)} = \sum_{j \in S_l} M_{ij} \widetilde{a}_i^{(k,l-1)} \tag{5}$$

If $\widetilde{e}_i^{(k,l)}$ exceeds the CTV, voxel $i$ is updated as in (4). However, if $\widetilde{e}_i^{(k,l)}$ does not exceed the CTV, voxel $i$ is not updated. Rather, $\widetilde{e}_i^{(k,l)}$ *and* the correction factor *and* the normalization factor accumulate during $x$ additional sub-iterations ($1 \leq x \leq L-1$):

$$
\left.
\begin{aligned}
\widetilde{E}_{sum,i}^{(k,l+x)} &= \widetilde{e}_i^{(k,l)} + ... + \widetilde{e}_i^{(k,l+x)} \\
C_{sum,i}^{(k,l+x)} &= C_i^{(k,l)} + ... + C_i^{(k,l+x)} \\
N_{sum,i}^{(k,l+x)} &= N_i^{(l)} + ... + N_i^{(l+x)}
\end{aligned}
\right\} \quad \text{if} \quad x \leq L-l
$$

$$
\left.
\begin{aligned}
\widetilde{E}_{sum,i}^{(k+1,l-L+x)} &= \widetilde{e}_i^{(k,l)} + ... + \widetilde{e}_i^{(k,L)} + \widetilde{e}_i^{(k+1,1)} + ... + \widetilde{e}_i^{(k+1,l-L+x)} \\
C_{sum,i}^{(k+1,l-L+x)} &= C_i^{(k,l)} + ... + C_i^{(k,L)} + C_i^{(k+1,1)} + ... + ... + C_i^{(k+1,l-L+x)} \\
N_{sum,i}^{(k+1,l-L+x)} &= N_i^{(l)} + ... + N_i^{(L)} + N_i^{(1)} + ... + N_i^{(l-L+x)}
\end{aligned}
\right\} \text{if} \quad x > L-l
\tag{6}
$$

Voxel $i$ is only updated once the estimated number of counts that voxel $i$ has contributed to the accumulated $x+1$ subsets exceeds the CTV:

$$
\begin{aligned}
\widetilde{a}_i^{(k,l+x)} &= \widetilde{a}_i^{(k,l-1)} \frac{C_{sum,i}^{(k,l+x)}}{N_{sum,i}^{(k,l+x)}} &\text{if} \quad x \leq L-l \\[2ex]
\widetilde{a}_i^{(k+1,l-L+x)} &= \widetilde{a}_i^{(k,l-1)} \frac{C_{sum,i}^{(k+1,l-L+x)}}{N_{sum,i}^{(k+1,l-L+x)}} &\text{if} \quad x > L-l
\end{aligned}
\tag{7}
$$

We implemented (7) with the additional requirement of a nonzero update factor to prevent that low-activity voxels can be updated to zero activity. With CR-OSEM, low-activity voxels will not be updated every sub-iteration, rather they are updated fewer times, each time using a larger subset (which consists of $x+1$ original subsets) of the projection data. If a voxel is not updated during $L$ subsequent sub-iterations, a forced update is performed for that voxel. This way, the number of individual voxel updates in every full iteration of CR-OSEM lies between 1 and $L$. To make the CTV independent of the reconstructed voxel size, it is in units of

counts/ml/subset. Before image reconstruction commences, the CTV is scaled to counts/voxel/subset.

### 7.2.1.4 SR-OSEM

In the case of pixel-based subset schemes, every subset contains detector pixels from all projection views and different subsets are rather equally spread out over the detectors. Projections of the activity distribution in different subsets will therefore be approximately equal in the noise-free case. As a consequence, it can be expected that for the same activity estimate, the update factors acquired in different subsets are very similar for a specific voxel. These update factors will also be similar to the corresponding MLEM update factor. However, differences between subset- and MLEM update factors will grow if the number of counts in the projections is lower due to increased variance in the number of counts. The level of similarity between the update factors of different subsets for a certain voxel may therefore be an indicator of how many updates can safely be performed on that voxel. SR-OSEM is based on this idea, namely of attaining a certain level of similarity between subset update factors for each voxel before it is updated. To this end, SR-OSEM groups together subsets to a level that the maximum deviations from the subset update factors with respect to the MLEM update factor are smaller than a user-specified Similarity Threshold Value (STV). STV is a number between 0% and 100% indicating how much update factors from different subsets are allowed to vary from the corresponding MLEM update factor.

Like CR-OSEM, SR-OSEM also commences with a single MLEM iteration. While calculating the MLEM update factor for each voxel, the correction- and normalization factors of the individual subsets are calculated as well (for the same uniform start image). These factors are used to determine the value of the deviation $D_i^{(1,l)}$ (%) of the update factor for each voxel $i$ and subset $l$ relative to the corresponding MLEM update factor for voxel $i$:

$$D_i^{(1,l)} = \left| \frac{C_i^{(1,l)}}{N_i^{(l)}} - \frac{C_{MLEM,i}^{(1)}}{N_{MLEM,i}} \right| / \frac{C_{MLEM,i}^{(1)}}{N_{MLEM,i}} \times 100\% \tag{8}$$

If deviations $D_i^{(1,l)}$ for all subsets are smaller than the STV, similarity between subset update factors is deemed sufficiently high to justify updates in every sub-iteration for all subsequent full iterations of SR-OSEM. However, if the deviation for one or more subsets is larger than the STV, subsets are paired to form $L/2$ new larger subsets and the corresponding correction- and normalization factors are calculated. The update factors corresponding to these newly formed subsets are then again compared to the MLEM update factor and percentage deviations are determined as in (8). This process continues until update factors of all individual subsets deviate less than the STV. This way, a voxel will be updated either $L$, $L/2$, $L/4,..,4$, 2 or 1 times per full iteration of SR-OSEM in all subsequent iterations. Note that if subsets are paired to form new subsets, $L$ has to be a power of 2. One may also choose to group larger numbers of subsets together to form new subsets (e.g. grouping together 4

subsets at a time). However, this may hamper reconstruction speed in cases where grouping fewer subsets together (and therefore more voxel updates per full iteration of SR-OSEM) would already yield high enough similarity between update factors of different subsets.

Note that with SR-OSEM the update scheme of voxels is only determined once in the first MLEM iteration. As a result, correction- and normalization factors for a voxel will never accumulate in a subsequent full iteration, which can be the case for CR-OSEM (i.e. formula (6)) which has a dynamic update scheme that may change depending on new activity estimates.

## 7.2.2 U-SPECT-II and VECTor

Two scanners, namely U-SPECT-II and VECTor (MILabs B.V., The Netherlands), have been used to acquire the data presented in this paper.

U-SPECT-II is a dedicated small-animal SPECT system comprising three stationary detectors with multi-pinhole collimators optimized for differently sized rodents. In this work, the general-purpose mouse collimator was used for the *in vivo* scan of a mouse. The collimator used in this work has 75 focused pinholes (ø 0.6 mm) and U-SPECT-II can achieve resolutions of <0.4 mm when equipped with this collimator [15]. The corresponding system matrix was obtained using the method described in [16]. Digital phantom simulations in this paper were based on the same collimator and detector geometry. Details of the SPECT simulator are provided in the next section.

The recently introduced VECTor system, which is based on the U-SPECT-II platform, uses a high-energy collimator with clustered multi-pinholes to enable (simultaneous) imaging of SPECT and PET radiotracers [17]. The VECTor collimator that is optimized for imaging rats was used to acquire the resolution phantom scans in this paper. The collimator has 156 pinholes (ø 1.8 mm). When equipped with this collimator, VECTor can achieve resolutions of approximately 1.1 mm for $^{99m}$Tc (140 keV photons) and approximately 1.3 mm for $^{18}$F (511 keV photons). The system matrices for SPECT and PET tracers for VECTor were calculated using a ray tracing code [18]. Inputs to this code were energy-specific photon attenuation coefficients of the collimator and detector materials and the positions and orientations of the pinholes and detectors. The positions and orientations of the pinholes and detectors were obtained from point-source measurements.

All scans in this work were acquired using the scanning focus method [19] in combination with a spiral bed-positioning protocol [20].

## 7.2.3 Simulated SPECT scan of a digital image quality phantom

In order to evaluate the reconstruction speed of CR-OSEM and SR-OSEM, SPECT simulations of a digital image quality phantom that was filled with a $^{99m}$Tc solution were performed. The mouse-sized cylindrical phantom (Fig. 2a) contained 5 spheres filled with

different activity concentrations. Every consecutive sphere contained a factor 10 lower activity concentration than the previous one (highest for sphere #1, lowest for sphere #5). In the center of each sphere a small spherical cold-lesion was placed for contrast measurements (diameter 2 mm, no activity). The voxel size of the phantom (0.15 mm) was half the size of the voxels in the reconstructed images in order to mimic a continuous activity distribution. Ray tracing was used to simulate noiseless phantom projections and to pre-calculate the system matrix. The simulator accounted for resolution-degrading effects of pinhole diameter, pinhole edge penetration and the intrinsic resolution of the detectors [18, 21]. Poisson statistics were applied to generate 10 noise realizations from the noiseless projections taking into account the total administered activity (57.7 MBq), scan duration (60 min) and detection efficiency of the detectors (89%).

All noise realizations were reconstructed with MLEM, CR-OSEM (128 subsets) for different CTVs (40k and 20k counts/ml/subset) and with SR-OSEM (128 subsets) for different STVs (10% and 20%). We also performed reconstructions with OSEM with 128 subsets in order to illustrate the severity of OSEM reconstruction artifacts in low-activity regions. From the reconstructed images cold-lesion contrast and noise were calculated: Cold-lesion contrast inside a sphere was defined to be the contrast between the average reconstructed activity per voxel in a spherical annulus surrounding the cold-lesion (inner and outer diameter 4 mm and 8 mm respectively) and the average reconstructed activity per voxel inside a 1 mm diameter spherical VOI centered on the cold-lesion. The average contrast in each sphere at iteration $k$ was defined as the cold-lesion contrast averaged over all noise realizations. The normalized standard deviation over all voxels inside the cold-lesion VOI was averaged over all noise realizations to obtain a measure of the average noise in each sphere at iteration $k$.

## 7.2.4 Bone-scan of a mouse (SPECT)

A 30 g male mouse was anesthetized with isoflurane. An amount of 189 MBq $^{99m}$Tc-hydroxymethylene diphosphonate ($^{99m}$Tc-HDP) was injected in the tail vein. Scanning started right before injection. The mouse was scanned for 60 min in frames of 1 min. Low-count projection data was obtained from the last frame (1-min scan). Projection data with more counts was obtained by summing the projection data of the final 50 frames (50-min scan). For both sets of projection data the photopeak window was set to a width of 20%. A background window was set to each side of each photopeak window. Each background window had a width of 33% compared to the width of the photopeak window. This experiment was conducted following protocols approved by the Animal Research Committee of the University Medical Center Utrecht.

Both sets of projection data were reconstructed by MLEM (128 iterations), OSEM (128 subsets, 1 iteration), CR-OSEM (128 subsets, CTV=20k counts/ml/subset, 8 iterations) and SR-OSEM (128 subsets, STV=20%, 8 iterations). The reconstructed voxel size of the 1-min scan was 0.4 mm. The reconstructed voxel size of the 50-min scan was 0.2 mm. The

FWHM of the 3D Gaussian post-filter was 1 mm for the 1-min scan and 0.6 mm for the 50-min scan.

As a measure of the deviation of CR-OSEM and SR-OSEM reconstructions from the MLEM reconstruction, the normalized mean error (NME) and the normalized mean square error (NMSE) between the images were calculated:

$$NME = \sum_i \left| \frac{\tilde{a}_i^{(k)}}{\tilde{a}^{(k)}} - \frac{\tilde{a}_{MLEM,i}^{(128)}}{\tilde{a}_{MLEM}^{(128)}} \right|$$

$$NMSE = \sum_i \left( \frac{\tilde{a}_i^{(k)}}{\tilde{a}^{(k)}} - \frac{\tilde{a}_{MLEM,i}^{(128)}}{\tilde{a}_{MLEM}^{(128)}} \right)^2$$

(9)

In (9), $\tilde{a}_i^{(k)}$ is the reconstructed activity in voxel $i$ of the CR-OSEM or SR-OSEM image after $k$ iterations and $\tilde{a}^{(k)}$ is the total activity contained within the image. $\tilde{a}_{MLEM,i}^{(128)}$ and $\tilde{a}_{MLEM}^{(128)}$ are the corresponding activities in the MLEM image after 128 iterations.

## 7.2.5 Scans of a resolution phantom (SPECT and PET)

To evaluate the performance (i.e. contrast recovery speed and noise characteristics) of CR-OSEM and SR-OSEM for different gamma-photon energies and different numbers of counts, scans of a miniature resolution phantom ("Jaszczak" phantom) were reconstructed and analyzed.

Each sector of the phantom contained a set of equally sized capillaries with diameters of 1.7 mm (3 rods), 1.5 mm (3 rods), 1.3 mm (3 rods), 1.1 mm (3 rods), 0.95 mm (6 rods), and 0.85 mm (6 rods). The distance between the centers of neighboring capillaries within a sector equaled twice the diameter of the capillaries. Two 60-min scans were made, in one scan the phantom was filled with 59 MBq $^{99m}$Tc solution (140 keV photons), in the other scan the phantom was filled with 31 MBq $^{18}$F solution (511 keV annihilation photons). For each scan, two sets of projection data were obtained from the list mode data, one with 100M counts, the other with 1M counts. This corresponds for $^{99m}$Tc to 60-min scans with approximately 11 MBq and 0.11 MBq in the phantom. For $^{18}$F this corresponds to 60-min scans of phantoms filled with approximately 17 MBq and 0.17 MBq. For all scans a photopeak window with a width of 15% was selected and a background window was set to each side of the photopeak window. For $^{99m}$Tc, each background window had a width of 50% compared to the width of the photopeak window. For $^{18}$F, each background window had a width of 30% compared to the width of the photopeak window.

All four sets of projection data were reconstructed by MLEM, OSEM (128 subsets), CR-OSEM (128 subsets, CTV=20k counts/ml/subset) and SR-OSEM (128 subsets, STV=20%). The reconstructed voxel size of the $^{99m}$Tc-scan was 0.4 mm. The reconstructed voxel size of the $^{18}$F-scan was 0.6 mm. The FWHM of the 3D Gaussian post-filter was

0.8 mm for the $^{99m}$Tc-scan and 1.0 mm for the $^{18}$F-scan. Three of the six sectors of the phantom were separately considered for the contrast-noise analysis (1.7mm rods, 1.5mm rods and 1.3mm rods). In each sector hot and cold circular VOIs were selected in every axial image slice that was located within the central 3.6 mm along the axial direction of the rods. These VOIs had a radius equal to 90% of the radius of the rods. The hot VOIs were centered on the rods, the cold VOIs in between the rods (Fig. 2b). The average reconstructed activity per voxel in each VOI was calculated. From these numbers the average activity over all hot VOIs and the average activity over all cold VOIs were calculated to determine the contrast between the hot and the cold VOIs. As a measure of the noise in a sector, the normalized standard deviation over all voxels inside each of the cold VOIs was calculated. The noise was expressed as the average of these values.
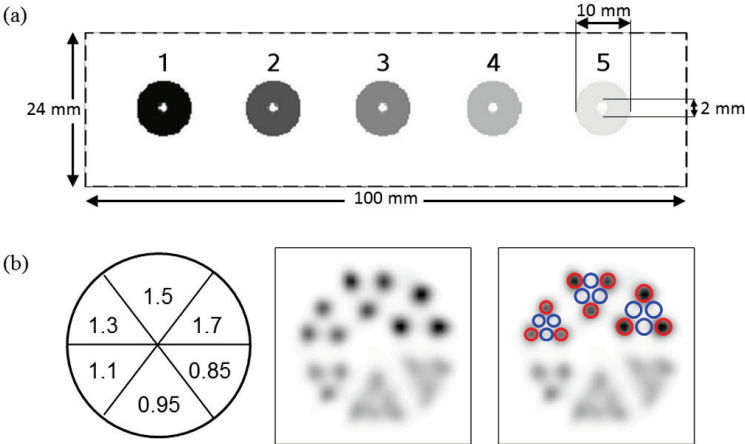


**Figure 2**. *(a) Image quality phantom containing 5 activity-filled spheres with spherical cold-lesions at their centers. Each consecutive sphere contained a factor 10 lower activity. (b) Left: 6 sectors of 'Jaszczak' resolution phantom. Rods in different sectors have different diameters (1,7, 1.5, 1.3, 1.1, 0.95 and 0.85 mm). Middle: Example reconstruction of resolution phantom SPECT scan ($^{99m}$Tc). Right: Hot (red) and cold (blue) regions in 3 of 6 sectors used for contrast-noise analysis.*

## 7.3 Results

### 7.3.1 Simulated SPECT scan of a digital image quality phantom

Figure 3b-f displays graphs of cold-lesion contrast vs. noise in spheres #1 to #5 of the image quality phantom (Fig. 3a) reconstructed with MLEM, OSEM-128, CR-OSEM (CTV=40k and 20k counts/ml/subset) and SR-OSEM (STV = 10% and 20%). The results are averages over 10 noise realizations. Acceleration factors of CR-OSEM and SR-OSEM over

MLEM discussed below do not consider the first (MLEM) iteration of CR-OSEM and SR-OSEM since there is no speed-up over MLEM in this iteration.

The speed-up of OSEM-128 over MLEM in spheres #1 and #2 was found to be approximately equal to the number of subsets, which can be deduced from the MLEM and OSEM-128 iteration numbers at approximately equal contrast and noise. The observed speed-up of OSEM-128 over MLEM in sphere #3 was even higher than the number of subsets. However, the observed additional speed increase is likely caused by erasure of activity just below the sphere surface in the reconstructions of the individual noise realizations (this is not visible in Fig. 3a; these images are averages over all noise realizations). For spheres #4 and #5, OSEM-128 led to even more severe artifacts since the activity in these spheres was completely erased and corresponding contrast and noise were defined zero. Results of the phantom scan for OSEM operated with less than 128 subsets (i.e. 16, 32 and 64 subsets) – which also led to severe reconstruction artifacts- can be found in chapter 6 (e.g. Fig. 3 and 4).

It is clear that CR-OSEM reconstruction resulted in accelerated contrast recovery over MLEM in high-activity spheres #1 and #2. It can also be seen that acceleration over MLEM decreased with increasing iterations: e.g. for sphere #2, 17 iterations CR-OSEM-40k resulted in equivalent contrast as 128 iterations MLEM while an additional 36 iterations of CR-OSEM-40k (i.e. 53 iterations CR-OSEM-40k) resulted in a contrast equivalent to only 128 additional MLEM iterations (i.e. 256 iterations MLEM). As would be logically expected, the acceleration of CR-OSEM over MLEM was higher for a lower CTV since a lower CTV allows for more updates and should therefore result in faster reconstruction speeds. However, while there is initial speed-up of CR-OSEM over MLEM in sphere #3, for higher iterations this is certainly not the case, rather CR-OSEM displays slower contrast recovery speed than MLEM: 69 iterations CR-OSEM-40k (i.e. from 33 to 102 iterations) and 105 iterations CR-OSEM-20k (i.e. from 22 to 127 iterations) were required to achieve approximately the same gain in contrast that is achieved by MLEM within 64 iterations (i.e. from 64 to 128 iterations). Similar observations are made for sphere #4. Moreover, these numbers indicate that a higher CTV results in an increased speed, which is a counter-intuitive result since a lower CTV allows for more updates and should therefore result in faster reconstruction speeds. These findings indicate that although CR-OSEM demonstrated speed-up over MLEM in early iterations, CR-OSEM reconstruction can result in compromised performance at higher iterations.

SR-OSEM generally achieved considerably higher acceleration factors over MLEM than CR-OSEM. For SR-OSEM, a higher STV resulted in higher reconstruction speeds: In sphere #1 acceleration factors of 128 are attained by SR-OSEM for both STVs, in sphere #2 acceleration factors of about 64 and 20 are attained by respectively SR-OSEM-20 and SR-OSEM-10, in sphere #3 acceleration factors of about 13 and 5 are attained for respectively SR-OSEM-20 and SR-OSEM-10, in sphere #4 SR-OSEM acceleration is still more than twice as fast as MLEM for both STVs. The acceleration factor over MLEM in sphere #5 lies between 1 and 2 for both STVs.
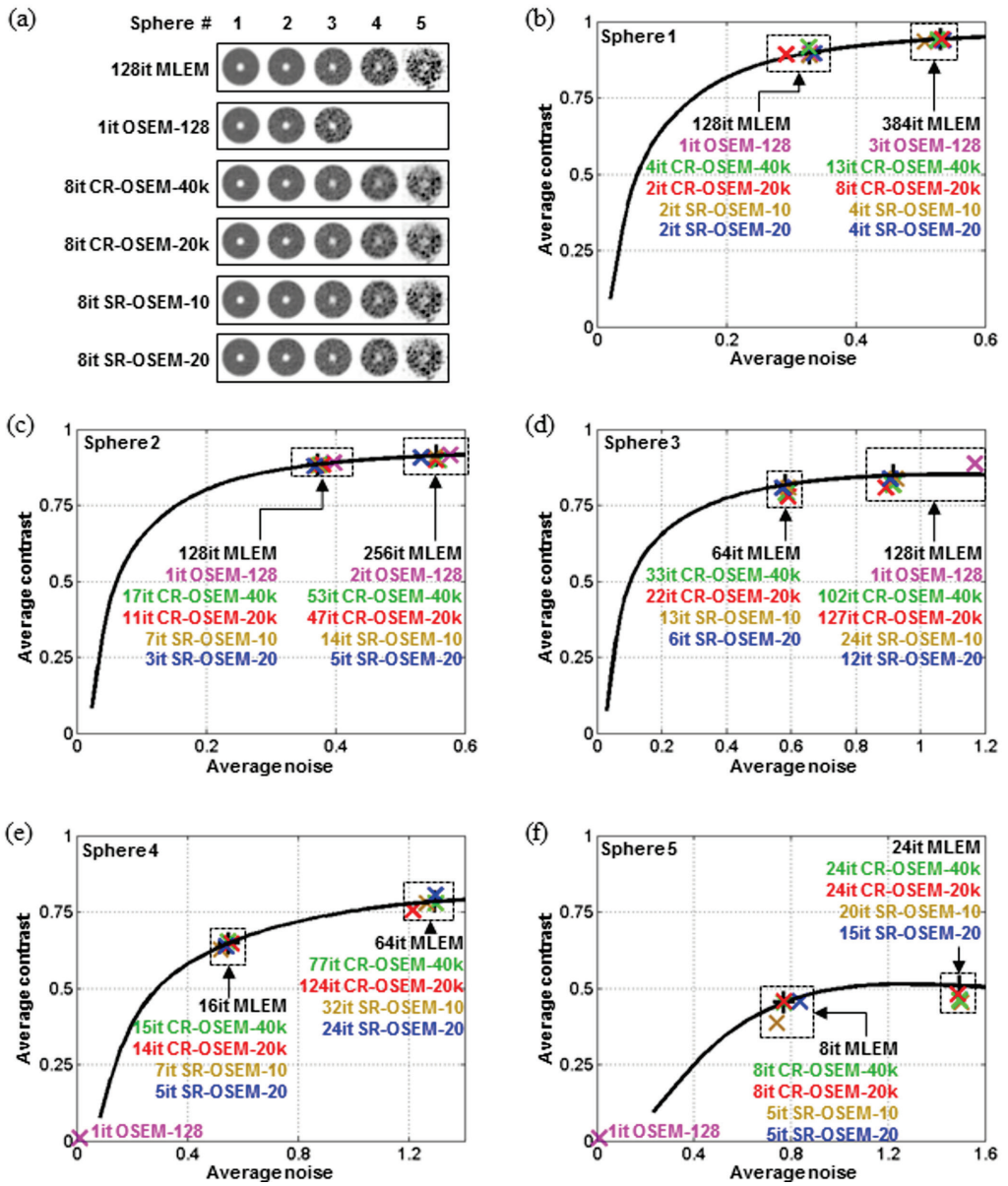
**Figure 3**. *Results for reconstructions of MLEM, OSEM, CR-OSEM and SR-OSEM (results are averages over 10 noise realizations) of simulated image quality phantom scan (57.7 MBq $^{99m}Tc$, 60 min scan time). (a) Longitudinal image slices through centers of each sphere (different grayscale per sphere). (b-f) Graphs of average contrast vs. average noise in spheres #1 to #5.*

## 7.3.2 Bone-scan of a mouse (SPECT)

Figures 4 and 5 show results for CR-OSEM-20k and SR-OSEM-20 reconstructions of the same mouse bone-scan as Fig. 1, which led to severe reconstruction artifacts for OSEM.

Fig. 4a displays maximum-intensity-projections (MIPs), image slices and image profiles for the reconstructions of the 1-min scan. Results for MLEM and OSEM-128 are shown for respectively 128 and 1 iterations. Results for CR-OSEM-20k and SR-OSEM-20 are shown for 8 iterations, as this allows to study differences in reconstruction speed and accuracy between these algorithms.

OSEM-128 led to serious artifacts since activity in most voxels was erased. From the image profiles it can be seen that the SR-OSEM-20 profile is closer to the MLEM profile than the CR-OSEM-20k profile. Fig. 4b shows the NME (log10 scale) and NMSE (log10 scale) of the images reconstructed with CR-OSEM-20k and SR-OSEM-20 with respect to the MLEM image (128 iterations) as a function of the number of iterations of CR-OSEM and SR-OSEM. It can be seen that SR-OSEM-20 results in considerably faster reconstruction than CR-OSEM-20k since the difference with the MLEM image diminishes much more quickly with SR-OSEM-20.

Figure 5 displays similar results for the 50-min scan: in the reconstruction by OSEM-128 there were still visible artifacts; e.g. part of the activity in the jawbone was erased. Furthermore, the image profile through the OSEM-128 image visibly deviated from the MLEM profile in some places. The image profiles of the CR-OSEM-20k and SR-OSEM-20 images are both close to the MLEM-profile although the CR-OSEM-20k-profile deviates a little more. Figure 5b conveys the same message as Fig. 4b: the difference with the MLEM image (128 iterations) diminishes significantly more quickly with SR-OSEM-20 than with CR-OSEM-20k.
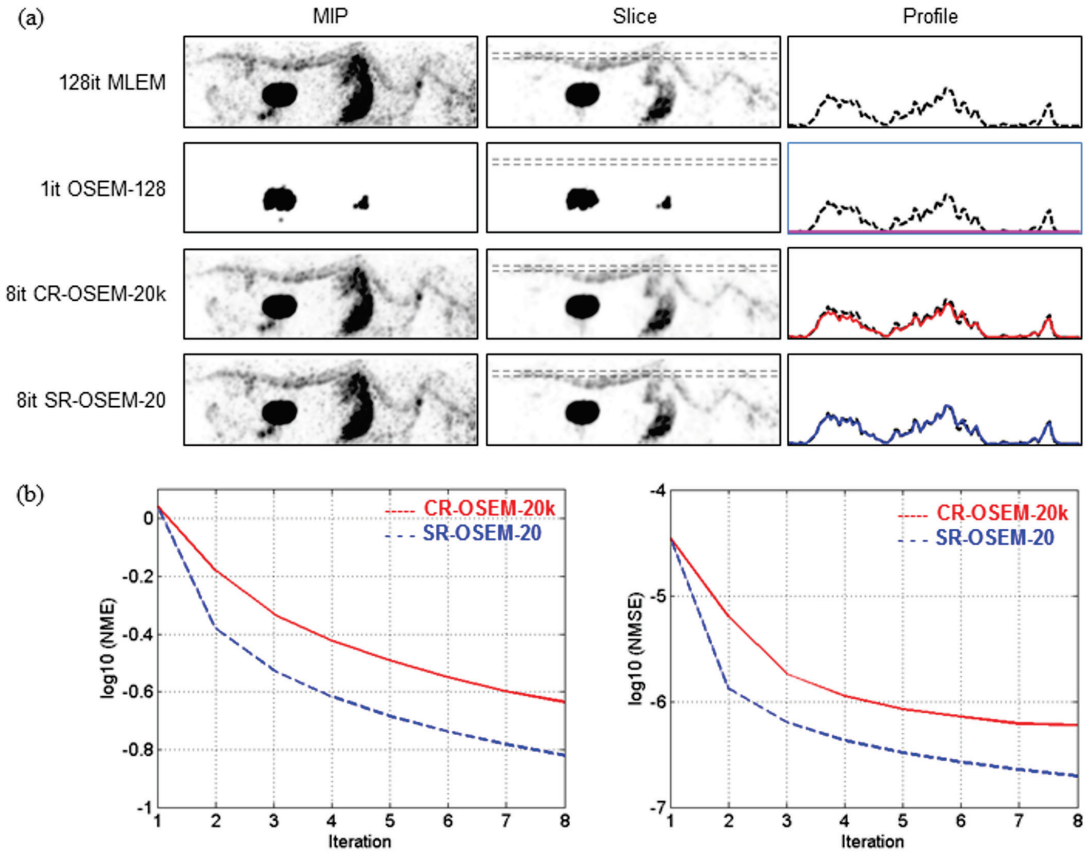
**Figure 4**. *(a) MIPs, image slices and image profiles of 1-min mouse bone-scan reconstructions of the same scan as in Fig. 1 (189 MBq $^{99m}Tc$-HDP) with MLEM, OSEM-128, CR-OSEM-20k and SR-OSEM-20. (b) NME and NMSE of reconstructions of CR-OSEM-20k (solid red) and SR-OSEM-20 (dashed blue) with respect to MLEM image (128 iterations) as function of number of iterations of CR-OSEM-20k and SR-OSEM-20.*
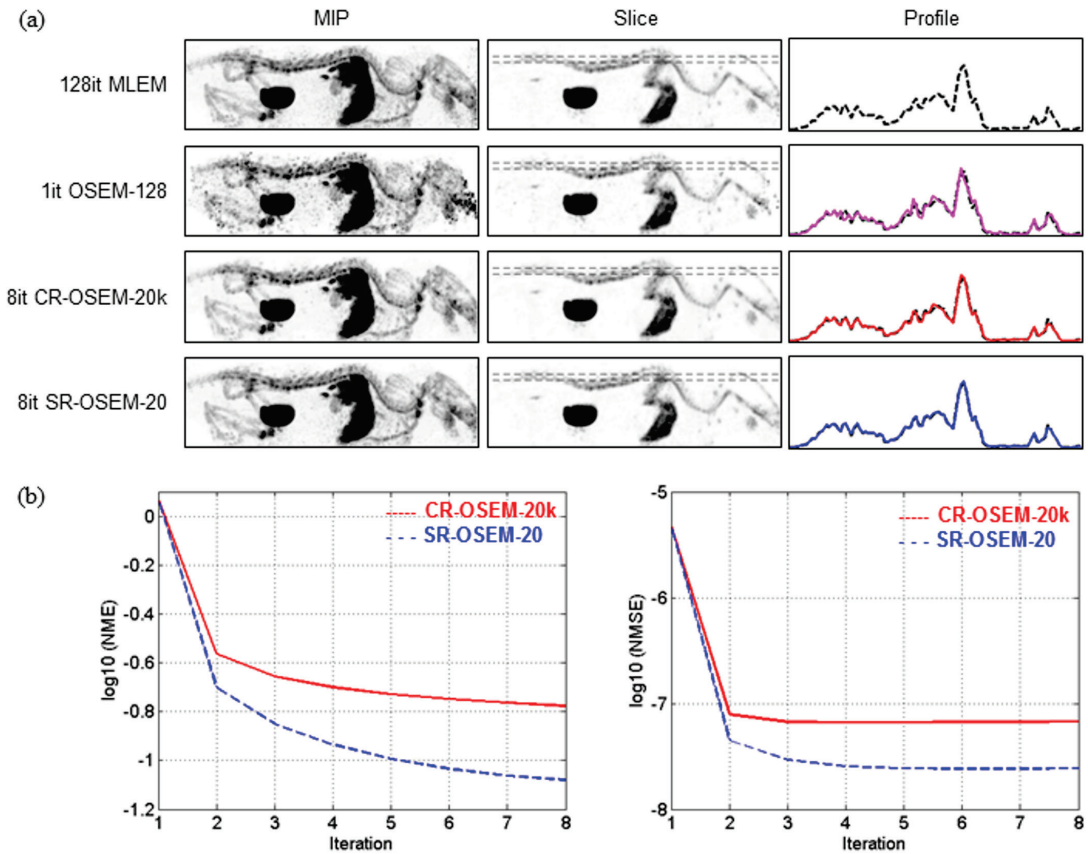
**Figure 5**. *Like Fig. 4, but now for a 50-min mouse bone-scan.*

## 7.3.3 Scans of a resolution phantom (SPECT and PET)

Figure 6a displays graphs of contrast vs. noise in different sectors of the resolution phantom that was filled with $^{99m}$Tc and that was reconstructed with MLEM, OSEM-128, CR-OSEM-20k and SR-OSEM-20.

For the reconstruction with 100M counts, CR-OSEM-20k and SR-OSEM-20 displayed similar reconstruction speeds after their first (MLEM) iteration, namely approximately equal to OSEM-128 and about 128 times faster than MLEM. For the reconstruction of the projection data with 1M counts, SR-OSEM-20 attained reconstruction speeds that were about 100 times faster than MLEM for the sectors with 1.7mm and 1.5mm rods and a speed of about 80 times faster than MLEM in the sector with 1.3mm rods. The initial reconstruction speed of CR-OSEM-20k was much lower. Moreover, the observed reconstruction speed at higher iterations was even lower than MLEM: CR-OSEM-20k did not attain the same contrast as MLEM for the same number of iterations (i.e. 896 iterations) in the sector with 1.3 mm rods.

Figure 6b shows image slices (thickness 3.6 mm) through the reconstructed images. For each algorithm, the reconstructions of the projections with 100M and 1M counts are shown at the same iteration number. At these numbers all tested algorithms had approximately equal contrast in the sector with 1.7 mm rods in the reconstructions of the projections with 100M counts. It can be readily seen that the 1.1 mm rods can be visually distinguished in all reconstructions of the projections with 100M counts. However, for the reconstruction of the projections with 1M counts this is not the case for CR-OSEM-20k. Moreover, the CR-OSEM-20k image shows a higher background activity.

Figure 7a shows the results of the scan of the phantom that was filled with $^{18}$F. Similar observations are made as for the reconstructions of the scan of the phantom that was filled with $^{99m}$Tc: The reconstruction speed-up of SR-OSEM-20 and CR-OSEM-20k over MLEM after their first (MLEM) iteration were approximately equal to OSEM-128, namely about 128 times faster than MLEM. For the reconstruction of the projection data with 1M counts, SR-OSEM-20 still attained a similar speed-up over MLEM as OSEM-128. However, the initial reconstruction speed of CR-OSEM-20k was much lower and CR-OSEM-20k did not attain the same contrast as MLEM at higher iterations. Moreover, in the sector with 1.3 mm rods, noise is higher at the same contrast compared to MLEM.

Figure 7b shows image slices through the reconstructed images. The 1.3 mm rods can be visually distinguished in all images that were reconstructed from the projections with 100M counts. This is also the case for the images that were reconstructed from the projections with 1M counts, except for the image reconstructed by CR-OSEM-20k in which the 1.3 mm rods have not been resolved.
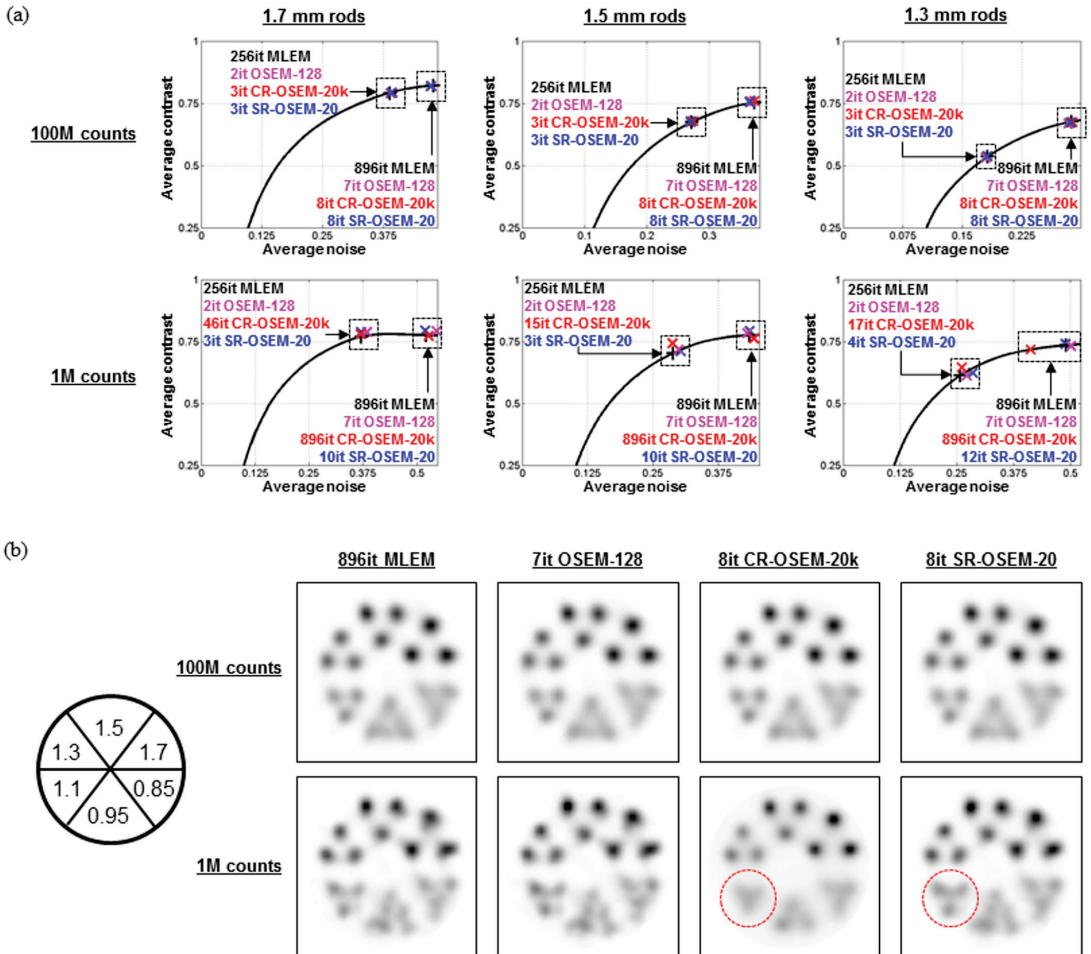
**Figure 6**. *Results of reconstruction by MLEM, OSEM-128, CR-OSEM-20k and SR-OSEM-20 of resolution phantom scan filled with $^{99m}$Tc. (a) Graphs of average contrast vs. average noise in different sectors of phantom. Graphs correspond to reconstructions of projection data containing 100M counts (top row) and 1M counts (bottom row). CR-OSEM-20k displays compromised contrast recovery for the reconstruction of the projections with 1M counts. (b) Image slices through reconstructions of projections with 100M counts (top row) and with 1M counts (bottom row) shown at the same iteration number for each algorithm. For these iteration numbers all tested algorithms had approximately equal contrast in the sector with 1.7 mm rods in reconstructions of projections with 100M counts. CR-OSEM-20k does not recover 1.1 mm rods in reconstruction of 1M counts, SR-OSEM-20 does (dashed red circles).*
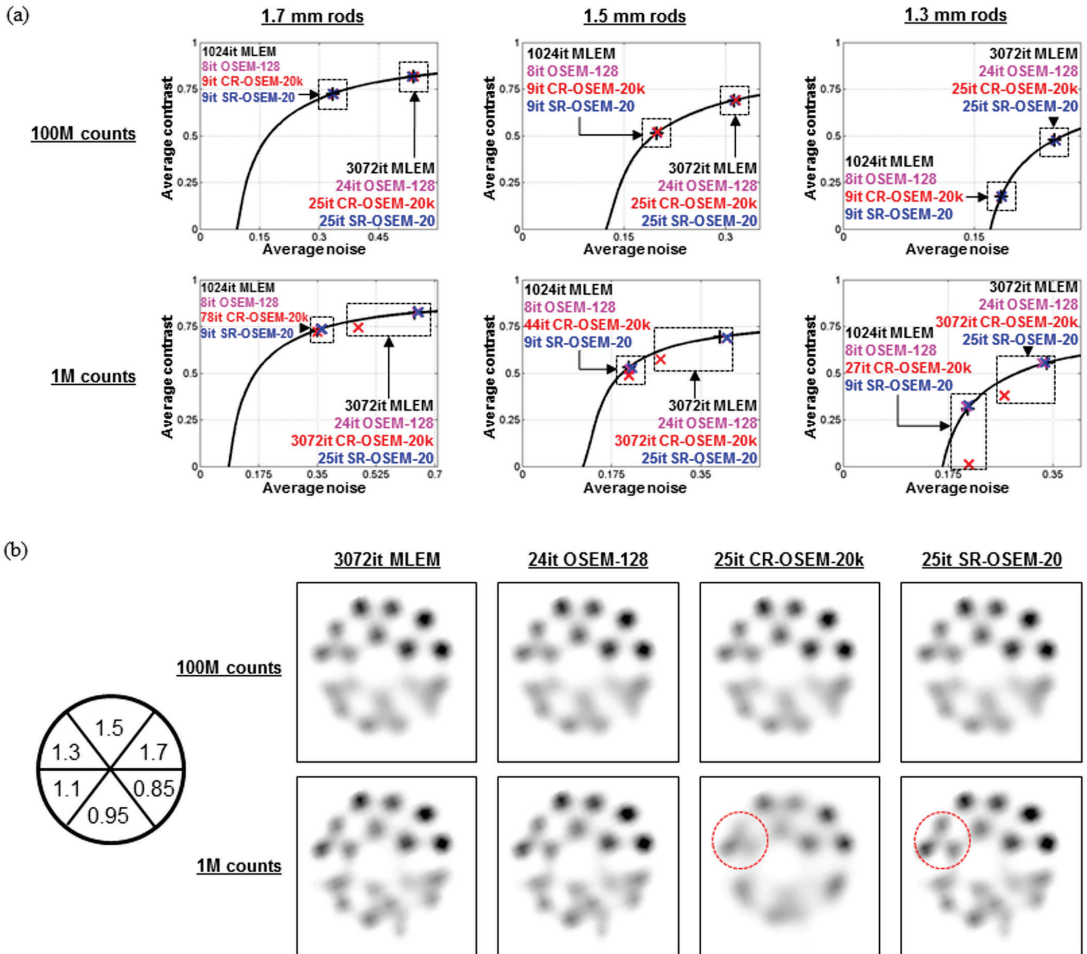
**Figure 7**. *Like Fig. 6, but now for a scan of resolution phantom filled with $^{18}F$. **(a)** CR-OSEM-20k displays compromised contrast recovery for the reconstruction of the projections with 1M counts. **(b)** CR-OSEM-20k does not recover 1.3 mm rods in reconstruction of 1M counts, SR-OSEM-20 does (dashed red circles).*

## 7.4 Discussion

In [12] we introduced CR-OSEM and found that it could achieve fast reconstruction - and therefore high resolution recovery- in highly active regions while preventing erasure of activity in regions with low activity. In this work we extended the validation of CR-OSEM to the reconstruction of pinhole-collimated imaging of both SPECT and PET tracers. We showed that reconstruction speed of CR-OSEM in image regions with low-activity can sometimes still be rather slow. Moreover, at higher iterations contrast did not always reach the same level as is reached with MLEM after many iterations. As a faster alternative to CR-OSEM we

introduced SR-OSEM in this work. In regions with lower activities SR-OSEM generally displayed significantly faster reconstruction speeds than CR-OSEM. The compromised performance with respect to contrast recovery that was observed with CR-OSEM was not observed with SR-OSEM.

The compromised performance of CR-OSEM with respect to cold-lesion contrast recovery at later iterations is likely due to the fact that in these iterations the estimated activity in the cold-lesion is reduced to a level that the cold voxels are only updated a few/one time(s) per full iteration, while neighboring hot voxels are still updated many times per full iteration. Therefore, image noise in hot voxels increases fast, which may have a negative effect on new activity estimates of the cold voxels since their update factors are (partly) based on detector pixels onto which noisy hot voxels also project. In contrast, with SR-OSEM the number of updates of a voxel does not directly depend on its activity estimate, rather it is directly related to the quality of the projection data which is comparable for neighboring cold and hot voxels. As a result, cold and hot voxels that lie in the same neighborhood are updated at a similar rate.

CR-OSEM and SR-OSEM use the concepts of adaptive subset formation and spatially adaptive voxel updates: The number of voxel updates can be non-uniform over the image and, as a consequence, resolution and noise can also vary over the image. Non-uniform image resolution can introduce errors in quantitative comparisons since the extend of partial-volume effects may vary over the image. As we showed in this work, in regions with low activity SR-OSEM generally resulted in considerable higher reconstruction speeds than CR-OSEM. As a result, for the same number of iterations, partial-volume-effects can be strongly reduced with SR-OSEM compared to CR-OSEM.

## 7.5 Conclusions

CR-OSEM and SR-OSEM both display high speed-up over MLEM in highly active image regions. However, in regions with lower activity SR-OSEM generally displayed significantly faster reconstruction speeds than CR-OSEM. The compromised performance in contrast recovery that was observed with CR-OSEM in later iterations was not observed with SR-OSEM. We conclude that SR-OSEM is fast, safe and can be used with a single setting of reconstruction parameters for the reconstruction of pinhole-collimated emission tomography of SPECT and PET tracers.

# *Bibliography*

[1]     F. J. Beekman, H. W. A. M. De Jong, and S. Van Geloven, "Efficient fully 3-D iterative SPECT reconstruction with Monte Carlo-based scatter compensation," *IEEE Trans. Med. Imag.,* vol. 21, no. 8, pp. 867-877, 2002.

[2]     B. F. Hutton, H. M. Hudson, and F. J. Beekman, "A clinical perspective of accelerated statistical reconstruction," *Eur. J. Nucl. Med.,* vol. 24, no. 7, pp. 797-808, 1997.

[3]     R. Leahy, and C. Byrne, "Recent developments in iterative image reconstruction for PET and SPECT," *IEEE Trans. Med. Imag.,* vol. 19, no. 4, pp. 257-260, 2000.

[4]     R. M. Leahy, and J. Y. Qi, "Statistical approaches in quantitative positron emission tomography," *Stat. Comput.,* vol. 10, no. 2, pp. 147-165, 2000.

[5]     J. Qi, and R. M. Leahy, "Iterative reconstruction techniques in emission computed tomography," *Phys. Med. Biol.,* vol. 51, no. 15, pp. R541-78, 2006.

[6]     K. Lange, and R. Carson, "EM reconstruction algorithms for emission and transmission tomography," *J. Comput. Assist. Tomogr.,* vol. 8, pp. 306-316, 1984.

[7]     L. A. Shepp, and Y. Vardi, "Maximum likelihood reconstruction for emission tomography," *IEEE Trans. Med. Imag.,* vol. 1, no. 2, pp. 113-22, 1982.

[8]     H. M. Hudson, and R. S. Larkin, "Accelerated image-reconstruction using ordered subsets of projection data," *IEEE Trans. Med. Imag.,* vol. 13, no. 4, pp. 601-609, 1994.

[9]     C. Kamphuis, F. J. Beekman, and M. A. Viergever, "Evaluation of OS-EM vs ML-EM for 1D, 2D and fully 3D SPECT reconstruction," *IEEE Trans. Nucl. Sci.,* vol. 43, no. 3, pp. 2018-2024, 1996.

[10]    D. S. Lalush, and B. M. Tsui, "Performance of ordered-subset reconstruction algorithms under conditions of extreme attenuation and truncation in myocardial SPECT," *J. Nucl. Med.,* vol. 41, no. 4, pp. 737-44, 2000.

[11]    W. Branderhorst, B. Vastenhouw, and F. J. Beekman, "Pixel-based subsets for rapid multi-pinhole SPECT reconstruction," *Phys. Med. Biol.,* vol. 55, no. 7, pp. 2023-34, 2010.

[12]    P. E. B. Vaissier, M. C. Goorden, A. B. Taylor, and F. J. Beekman, "Fast count-regulated OSEM reconstruction with adaptive resolution recovery," *IEEE Trans. Med. Imag.,* vol. 32, no. 12, pp. 2250-2261, 2013.

[13]    D. J. Kadrmas, "Statistically regulated and adaptive EM reconstruction for emission computed tomography," *IEEE Trans. Nucl. Sci.,* vol. 48, no. 3, pp. 790-798, 2001.

[14]    K. Ogawa, Y. Harata, T. Ichihara, A. Kubo, and S. Hashimoto, "A practical method for position-dependent Compton-scatter correction in single photon emission CT," *IEEE Trans. Med. Imag.,* vol. 10, no. 3, pp. 408-12, 1991.

[15]    F. Van der Have, B. Vastenhouw, R. M. Ramakers, W. Branderhorst, J. O. Krah, C. Ji, S. G. Staelens, and F. J. Beekman, "U-SPECT-II: An Ultra-High-Resolution Device for Molecular Small-Animal Imaging," *J. Nucl. Med.,* vol. 50, no. 4, pp. 599-605, 2009.

[16]    F. Van der Have, B. Vastenhouw, M. Rentmeester, and F. J. Beekman, "System calibration and statistical image reconstruction for ultra-high resolution stationary pinhole SPECT," *IEEE Trans. Med. Imag.,* vol. 27, no. 7, pp. 960-71, 2008.

[17]    M. C. Goorden, F. van der Have, R. Kreuger, R. M. Ramakers, B. Vastenhouw, J. P. Burbach, J. Booij, C. F. Molthoff, and F. J. Beekman, "VECTor: a preclinical imaging system for simultaneous submillimeter SPECT and PET," *J. Nucl. Med.,* vol. 54, no. 2, pp. 306-12, 2013.

[18]    M. C. Goorden, F. Van der Have, R. Kreuger, and F. J. Beekman, "An efficient simulator for pinhole imaging of PET isotopes," *Phys. Med. Biol.,* vol. 56, no. 6, pp. 1617-34, 2011.

[19]    B. Vastenhouw, and F. Beekman, "Submillimeter total-body murine imaging with U-SPECT-I," *J. Nucl. Med.,* vol. 48, no. 3, pp. 487-93, 2007.

[20]    P. E. B. Vaissier, M. C. Goorden, B. Vastenhouw, F. van der Have, R. M. Ramakers, and F. J. Beekman, "Fast spiral SPECT with stationary gamma-cameras and focusing pinholes," *J. Nucl. Med.,* vol. 53, no. 8, pp. 1292-9, 2012.

[21]    M. Gieles, H. W. de Jong, and F. J. Beekman, "Monte Carlo simulations of pinhole imaging accelerated by kernel-based forced detection," *Phys. Med. Biol.,* vol. 47, no. 11, pp. 1853-67, 2002.

# 8. Summary

Single photon emission computed tomography (SPECT) is a key modality in preclinical imaging of small animals. Dedicated high-resolution small-animal SPECT systems are used to quantitatively and visually assess the distribution of radioactive biological markers (tracers) *in vivo* in order to e.g. study disease and test new pharmaceuticals. These systems usually apply multi-pinhole collimators with high pinhole magnification factors to achieve high resolution and sensitivity to enable the visualization of small details within small animals. Recently, the application of high-energy collimators has opened up the possibility of imaging positron emitting tracers (511 keV annihilation photons) with sub-mm resolutions, even simultaneously with single photon emitting tracers. This thesis described the development and validation of novel image acquisition and reconstruction techniques for multi-pinhole emission tomography of single-photon and positron emitting tracers.

Preclinical imaging with SPECT combined with either X-ray computed tomography (CT) or magnetic resonance imaging (MRI) has proven to be very useful in translational research. Today, CT and MRI are still mainly applied to anatomically localize tracer binding and to improve SPECT quantification, although both CT and MRI have additional potential. While preclinical SPECT/CT is most widely applied in oncology research, SPECT-MRI offers special potential for both neuroscience applications and oncological applications. Until now, SPECT and CT systems are often integrated into a single device, whereas at present combined SPECT and MRI is almost always carried out with separate systems. **Chapter 2** provided an overview of current preclinical research applications and trends of SPECT/CT and SPECT-MRI, which are mainly in tumor imaging and neuroscience imaging and discusses advantages and disadvantages of different hybrid imaging approaches.

Multi-pinhole SPECT systems with stationary detectors are able to perform fast total-body scans by shifting the animal bed through the collimator. However, a large number of highly overlapping scan positions results in long overhead times due to animal repositioning which hampers temporal resolutions that can be achieved with these systems. In **chapter 3** we developed and tested spiral trajectories (ST) of the animal bed with fewer bed positions in order to improve temporal resolutions of SPECT scans. In addition, we tested 'traditional' multiplane trajectories of the animal bed (MPT). We found that ST required less than half the number of bed positions compared to MPT in order to still achieve sufficient sampling. The reduced number of bed positions enabled by ST made it possible to perform a dynamic total-body bone scan and a dynamic hepatobiliary scan with time resolutions of 60 s and 15 s respectively. We conclude that ST open up new possibilities for high-throughput and fast dynamic radio-molecular imaging.

Recently, SPECT and PET imaging has been combined in a novel versatile emission computed tomography system (VECTor). VECTor enables simultaneous sub-mm imaging of

single-photon and positron emitting tracers in mice. VECTor enables scientists to select the most suitable combinations of radiotracers from the entire complement of available SPECT and PET tracers to study the correlation between different biological functions in the same animal at the same time with a single dose of anesthesia. To this end VECTor applies a dedicated clustered multi-pinhole (CMP) collimator that can be mounted on existing SPECT platforms. Compared to pinholes used in conventional SPECT collimators, the pinholes in the CMP collimator have more narrow opening angles to reduce photon penetration through the pinhole edges by the high-energy annihilation photons. In **chapter 4** we presented and validated the extended capability of VECTor to also enable simultaneous SPECT-PET imaging in rat-sized small animals using a newly developed CMP collimator. The tomographic resolution achieved for SPECT and PET tracers was found to be competitive with those attained by dedicated multi-pinhole SPECT and coincidence PET systems. The capabilities of VECTor were further illustrated by simultaneously acquired (dynamic) SPECT-PET scans of rats.

Cardiac parameters obtained from cardiac SPECT images can be affected by respiratory motion, image filtering and animal positioning. In **chapter 5** we investigated the influence of these factors on high-resolution murine myocardial perfusion SPECT. The results indicated that there is no significant difference in the measured cardiac parameters when respiratory motion correction was applied, while significant differences in left ventricular volumes were found with regard to different positioning of animals. A linear relationship was found between left ventricular volumes and the kernel size of the Gaussian filter. These finding indicate that respiratory gating does not improve high-resolution cardiac SPECT images, while the position of the animals and the image filters should be the same in a comparative study with multiple scans to avoid systematic differences in measured cardiac parameters.

Ordered Subsets Expectation Maximization (OSEM) is widely used to accelerate tomographic image reconstruction. Significant additional speed-up is achievable if OSEM is applied with pixel-based subset schemes. However, a high number of subsets can cause quantitative inaccuracy or even disappearance of lesions in low-activity image regions, while a low number of subsets leads to prohibitively long reconstructions or unrecovered details in highly active regions. In **chapter 6** we proposed Count-Regulated OSEM (CR-OSEM) to overcome these problems. CR-OSEM regulates the number of individual voxel updates –and therefore the size of voxel-wise subsets– based on local activity estimates, which depend on the number of counts in the projection data. It was shown for pinhole SPECT that CR-OSEM prevented erasure of activity in regions with low-activity, it displayed fast contrast recovery in high-activity regions, while contrast and noise in low-activity regions remained relatively low.

In **chapter 7** we extended the validation of CR-OSEM to the reconstruction of pinhole-collimated imaging of both SPECT and PET tracers. We showed that reconstruction speed of CR-OSEM in image regions with low-activity can sometimes still be rather slow.

Moreover, after a many iterations of CR-OSEM, contrast does not always reach the same level as is reached with MLEM after many iterations. To overcome these problems, we proposed and validated a novel algorithm, dubbed Similarity-Regulated OSEM (SR-OSEM). Like CR-OSEM, SR-OSEM also automatically and locally adapts the number of voxel updates. SR-OSEM does this based on a similarity criterion regarding the update factors for a voxel that are acquired in different subsets. SR-OSEM was compared to MLEM and CR-OSEM by reconstructions of simulated and experimental pinhole-collimated SPECT and PET data. Whereas both algorithms displayed high reconstruction speed-up over MLEM in highly active image regions, in low-activity regions SR-OSEM generally resulted in significantly faster reconstruction speeds than CR-OSEM. The compromised performance in contrast recovery that was observed with CR-OSEM was not observed with SR-OSEM. We conclude that SR-OSEM is fast, safe and can be used with a single setting of reconstruction parameters for image reconstruction in pinhole-collimated emission tomography of SPECT and PET tracers.

*Samenvatting*

# 9. Samenvatting

Single photon emission computed tomography (SPECT) is een belangrijke beeldvormende techniek die onder meer gebruikt wordt in proefdieronderzoek naar ziekten en voor het testen van farmaceutica. Hoge-resolutie SPECT systemen die speciaal zijn ontwikkeld voor kleine proefdieren zoals muizen en ratten worden gebruikt om *in vivo* de driedimensionale verdeling van radioactieve biologische zoekstoffen ('tracers') te visualiseren en te kwantificeren. Meestal maken deze systemen gebruik van multi-pinhole collimatoren met grote vergrotingsfactoren om een hoge resolutie en gevoeligheid te bereiken. Op deze manier kunnen details in kleine proefdieren worden gevisualiseerd. De toepassing van speciale hoge-energie collimatoren maakt het mogelijk om ook tracers die met positron emission tomography (PET) gebruikt worden met sub-millimeter resolutie te visualiseren. Zulke PET scans kunnen zelfs gelijktijdig met 'traditionele' SPECT scans gedaan worden. Deze thesis beschrijft de ontwikkeling en validatie van nieuwe beeldacquisitiemethoden en beeldreconstructietechnieken voor multi-pinhole emission tomography van SPECT and PET tracers.

Preklinische beeldvorming met SPECT in combinatie met X-ray computed tomography (CT) of magnetic resonance imaging (MRI) kent veel nuttige toepassingen in translationeel onderzoek. CT en MRI worden vandaag de dag vooral gebruikt voor anatomische lokalisering van tracers en voor de verbetering van SPECT kwantificatie. CT en MRI hebben echter meer potentie. Terwijl SPECT/CT vooral toepassingen kent in oncologisch onderzoek, biedt SPECT-MRI speciale mogelijkheden in neurologisch en oncologisch onderzoek. Tot dusver worden SPECT en CT vaak geïntegreerd in één apparaat, terwijl gecombineerde beeldvorming met SPECT en MRI meestal wordt uitgevoerd met losstaande scanners. **Hoofdstuk 2** gaf een overzicht van de preklinische onderzoektoepassingen en trends met betrekking tot SPECT/CT en SPECT-MRI in oncologie en neurologie. De voor- en nadelen van verschillende benaderingen van hybride beeldvorming werden ook besproken.

Multi-pinhole SPECT systemen met stationaire detectoren maken het mogelijk snelle scans van het gehele proefdierlichaam uit te voeren door het bed waarop het proefdier ligt in een aantal stappen door de collimator te verplaatsen. Echter, een groot aantal sterk overlappende scan posities resulteert in relatief veel verloren scan tijd als gevolg van de vele herpositioneringen van het dierbed. Dit is een belangrijke beperkende factor voor de temporele resoluties die met dit soort systemen gehaald kunnen worden. Om de temporele resoluties van SPECT scans te verbeteren werden in **hoofdstuk 3** scans met spiraalvormige banen van het dierbed (spiral trajectories; ST) met veel minder scan posities getest en gevalideerd. Daarnaast werd 'traditionele' multi-planaire positionering van het dierbed getest (multi-plane trajectories; MPT). We vonden dat ST minder dan de helft van het aantal bedposities vergde vergeleken met MPT om voldoende sampling te bereiken. Het relatief lage aantal bedposities met ST maakte een dynamische total-body botscan en een dynamische hepatobiliaire scan met tijdsresoluties van respectievelijk 60 s en 15 s mogelijk. We concluderen dat het gebruik van ST nieuwe mogelijkheden creëert voor high-throughput SPECT en snelle dynamische SPECT scans.

Onlangs zijn de mogelijkheden van SPECT en PET gecombineerd in een nieuw versatile emission computed tomography systeem (VECTor). VECTor maakt simultane beeldvorming van SPECT en PET tracers in muizen mogelijk met sub-millimeter resolutie. Hierdoor kunnen onderzoekers de meest geschikte tracercombinaties kiezen uit het totale complement van

beschikbare SPECT en PET tracers, waardoor de correlatie tussen verschillende biologische functies gelijktijdig in hetzelfde dier bestudeerd kan worden en er slechts een enkele dosis anesthetica nodig is. VECTor maakt gebruik van een speciale geclusterde multi-pinhole collimator (clustered multi-pinhole; CMP) die in bestaande SPECT systemen gemonteerd kan worden. Vergeleken met de pinholes in conventionele SPECT collimatoren hebben de pinholes in de CMP collimator kleinere openingshoeken om penetratie van de hoge-energie annihilatiefotonen door de pinholeranden te reduceren. In **hoofdstuk 4** presenteerden en valideerden we de mogelijkheid om met VECTor ook gelijktijdige SPECT-PET beeldvorming in proefdieren ter grootte van een rat te kunnen doen met behulp van een nieuw ontwikkelde CMP collimator. De tomografische resolutie met de nieuwe CMP ratcollimator voor SPECT en PET tracers is concurrerend met die van multi-pinhole SPECT en coincidence PET systemen die speciaal voor proefdieren zijn ontwikkeld. De mogelijkheden van VECTor werden verder geïllustreerd door simultaan verworven (dynamische) SPECT-PET-scans van ratten.

Cardiale parameters van proefdieren die verkregen zijn met SPECT kunnen worden beïnvloed door ademhalingsbeweging, beeldfiltering en positionering van de dieren in de scanner. In **hoofdstuk 5** onderzochten we de invloed van deze factoren op hoge-resolutie myocard perfusie SPECT van muizen. De resultaten gaven aan dat het toepassen van ademhalingscorrectie geen significant verschil in de gemeten cardiale parameters opleverde ten opzichte van het niet toepassen van ademhalingscorrectie. Echter, grote verschillen in linker ventriculaire volumes werden geobserveerd als de dieren anders gepositioneerd werden. Er werd een lineair verband geobserveerd tussen gemeten linker ventriculaire volumes en de grootte van het Gaussiaanse beeldfilter. Deze bevindingen geven aan dat het toepassen van ademhalingscorrectie geen verbetering oplevert voor hoge-resolutie cardiale SPECT, terwijl positionering van dieren en het gebruikte beeldfilter in een vergelijkende studie met meerdere scans gelijk gehouden moeten worden om systematische verschillen in cardiale parameters te voorkomen.

Ordered Subsets Expectation Maximization (OSEM) wordt veel gebruikt om tomografische reconstructie te versnellen. Aanzienlijke extra versnelling is haalbaar als OSEM wordt toegepast met pixel-based subsets. Echter, een groot aantal subsets kan resulteren in kwantitatieve beeldfouten of zelfs verdwijning van de laesies in gebieden met een lage activiteit. Aan de andere kant kan een (veilig) laag aantal subsets leiden tot buitensporig lange reconstructies of tot een suboptimale resolutie in gebieden met een hoge activiteit. Om deze problemen te overwinnen werd in **hoofdstuk 6** Count-Regulated OSEM (CR-OSEM) geïntroduceerd. CR-OSEM reguleert het aantal individuele voxel-updates –en daarmee de grootte van de corresponderende subsets– op basis van de schatting van de lokale activiteit, hetgeen afhangt van het aantal detecties in de projectiedata. Voor pinhole SPECT lieten we zien dat CR-OSEM voorkomt dat activiteit in gebieden met een lage activiteit verdwijnt en dat CR-OSEM resulteert in snelle contrast-recovery in gebieden met een hoge activiteit, terwijl contrast en ruis in gebieden met weinig activiteit relatief laag gehouden worden.

In **hoofdstuk 7** breidden we de validatie van CR-OSEM uit naar beeldreconstructie van pinhole SPECT data en pinhole PET data. We lieten zien dat de reconstructiesnelheid van de CR-OSEM in gebieden met een lage activiteit soms nogal traag kan zijn. Bovendien werd door CR-OSEM na een groot aantal iteraties niet altijd hetzelfde contrast bereikt als met MLEM na vele iteraties. Om deze problemen te verhelpen introduceerden en valideerden we een nieuw algoritme, genaamd Similarity-Regulated OSEM (SR-OSEM). Net als CR-OSEM

past ook SR-OSEM automatisch en lokaal het aantal voxel-updates aan. SR-OSEM doet dit op basis van de overeenkomst tussen de updatefactoren voor een voxel die verkregen zijn in verschillende subsets. SR-OSEM werd vergeleken met MLEM en CR-OSEM door middel van reconstructies van gesimuleerde en experimentele pinhole SPECT data en pinhole PET data. Beide algoritmen lieten grote reconstructieversnelling zien ten opzichte van MLEM in gebieden met hoge activiteit. In het algemeen was de reconstructiesnelheid van SR-OSEM in gebieden met een lage activiteit significant hoger dan die van CR-OSEM. De problemen met betrekking tot contrast-recovery die werden waargenomen voor CR-OSEM werden niet waargenomen met SR-OSEM. De conclusie is dat SR-OSEM snel en veilig is en kan worden gebruikt met een enkele instelling van de reconstructieparameters voor beeldreconstructie van pinhole SPECT data en pinhole PET data.

# Publications

## International journals

P. E. B. Vaissier, M. C. Goorden, B. Vastenhouw, F. van der Have, R. M. Ramakers, and F. J. Beekman, "Fast spiral SPECT with stationary gamma-cameras and focusing pinholes," *J. Nucl. Med.*, vol. 53, no. 8, pp. 1292-9, 2012.

P. E. B. Vaissier, M. C. Goorden, A. B. Taylor, and F. J. Beekman, "Fast count-regulated OSEM reconstruction with adaptive resolution recovery," *IEEE Trans. Med. Imag.*, vol. 32, no. 12, pp. 2250-2261, 2013.

M. R. Bernsen, P. E. B. Vaissier, R. Van Holen, J. Booij, F. J. Beekman, and M. de Jong, "The role of preclinical SPECT in oncological and neurological research in combination with either CT or MRI," *Eur. J. Nucl. Med. Mol. Imaging*, vol. 41 Suppl 1, pp. S36-49, 2014.

C. Wu, P. E. B. Vaissier, B. Vastenhouw, J. R. de Jong, R. H. J. A. Slart, and F. J. Beekman. "Influence of respiratory gating, image filtering and animal positioning on high-resolution ECG-gated murine cardiac SPECT," Submitted to *Mol. Imaging*, 2014.

P. E. B. Vaissier, F. van der Have, M. C. Goorden, O. Ivashchenko, B. Vastenhouw, R. M. Ramakers, and F. J. Beekman. "Simultaneous SPECT-PET imaging in rats," in preparation.

P. E. B. Vaissier, M. C. Goorden, and F. J. Beekman. "Regulated OSEM reconstruction and its application to pinhole emission tomography," in preparation.

## Conference proceedings

P. E. B. Vaissier, M. C. Goorden, A.B. Taylor, and F. J. Beekman. "Count-regulated OSEM reconstruction," *2012 IEEE Nuclear Science Symposium and Medical Imaging Conference Record*, pp. 3315-3320, 2012.

## Abstracts

P. E. B. Vaissier, M. C. Goorden, F. van der Have, B. Vastenhouw, and F. J. Beekman. **"**Fast whole-body mouse imaging with a stationary multi-pinhole SPECT system using spiral bed trajectories," *Small Animal Imaging Workshop, University of Arizona, 2010*.

P. E. B. Vaissier, M. C. Goorden, B. Vastenhouw, F. van der Have, and F. J. Beekman. "Ultra-fast total-body mouse imaging with U-SPECT-II," *2011 IEEE Nuclear Science Symposium and Medical Imaging Conference*, MIC21.S-189, 2011.

P. E. B. Vaissier, M. C. Goorden, and F. J. Beekman. "SR-POSEM: a new algorithm for improved accelerated image reconstruction of SPECT data," *2012 IEEE Nuclear Science Symposium and Medical Imaging Conference*, M17-10, 2012.

R. M. Ramakers, B. Vastenhouw, P. E. B. Vaissier, and F. J. Beekman, "Whole-body sub-half-minute 4D pharmacokinetic SPECT in mice," *J. Nucl. Med. meeting abstracts*, vol. 54, no. 2, pp. 264, 2013.

P. E. B. Vaissier, F. van der Have, M. C. Goorden, O. Ivashchenko, B. Vastenhouw, R.M. Ramakers, and F. J. Beekman. "High resolution simultaneous SPECT-PET imaging in rats," *SNMMI 2014 Annual Meeting*, publication number 2142, 2014.

P. E. B. Vaissier, M. C. Goorden, and F. J. Beekman. "Count-based update criteria for fast regulated OSEM reconstruction," *SNMMI 2014 Annual Meeting*, publication number 540, 2014.

P. E. B. Vaissier, M. C. Goorden, and F. J. Beekman. "Regulated OSEM Reconstruction for Pinhole Emission Tomography," *2014 IEEE Nuclear Science Symposium and Medical Imaging Conference*, M18-43, 2014.

# Curriculum Vitae

Pieter Eric Bart Vaissier was born on April 6 1985 in Nijmegen, The Netherlands. He grew up in Maastricht where he followed pre-university education  (Dutch: VWO) from 1997 to 2003.  In 2003 he started a study applied physics at the University of Groningen, The Netherlands, where he attained a Bachelor's degree in 2007. This was followed by a Master's degree in biomedical engineering in 2009 (specialization Medical Instrumentation & Imaging), which was acquired at the same university. The study for his Master thesis was performed at the department of radiation oncology at University Medical Center Groningen. At the end of 2009, he worked as an intern at Molecular Imaging Laboratories B.V. (MILabs B.V., Utrecht, The Netherlands) on an automated co-registration method for images obtained with small-animal SPECT and small-animal X-ray CT. In the beginning of 2010, he started as a PhD candidate at Delft University of Technology in the section Radiation, Detection and Medical Imaging led by professor Freek Beekman. The research focused on image acquisition methods and image reconstruction for multi-pinhole emission tomography, of which the results are described in this thesis.

# Dankwoord

Gedurende de laatste jaren van mijn studie in Groningen werd het voor mij steeds duidelijker dat ik absoluut niet wilde gaan promoveren. In mijn hoofd leed een promovendus een vierjarig kluizenaarsbestaan achter een pc in een kamer zonder ramen. De zoete beloning voor dit lijden? Een boek dat niemand leest. Deze beschrijving is misschien lichtelijk overdreven, maar desalniettemin werd mijn beeld ten positieve gecorrigeerd toen ik mijn studie afsloot met een stage bij MILabs, het bedrijf van professor Freek Beekman. De combinatie van wetenschap en industrie sprak mij direct heel erg aan. Freek gaf mij de mogelijkheid te promoveren in Delft. Niet alleen heb ik hierdoor heel veel kunnen leren op wetenschappelijk gebied, ook heb ik MILabs van de zijlijn mogen meemaken. Bovendien zijn Freek's tomeloze energie en drive een sterke motivator. Freek, voor dit alles wil ik je heel erg bedanken!

Verder wil ik mijn copromotor en 'supervisor' Marlies Goorden heel erg bedanken. Voor het delen van kennis. Voor de (werk-gerelateerde) discussies die we hadden. Voor de programmeerhulp. En voor het geduld dat je met mij had: Marlies, het moet soms zwaar geweest zijn voor je…en dat is het misschien nog...Nee toch???

Ook wil ik alle anderen uit de (voormalige) sectie RD&M bedanken, in het bijzonder Samuel (Salut!), Jarno en Oleksandra (Thanks for the design of the cover of this thesis!). En niet te vergeten: de overige collega's van het RID met wie ik vaker in 'het Koepeltje' heb rondgehangen!

Ik heb ook veel te danken aan de (voormalige) medewerkers van MILabs waarmee ik afgelopen jaren heb samengewerkt, met name Ruud, Frans, Brendan en Chao.

Ook niet te vergeten: "Unne groete merci" voor Pa & Ma, Juliette & Aernout & Isabelle & Thomas, Jacques en Noortje.

Verder bedank ik bij deze ieder ander die niet valt onder bovengenoemde mensen maar die –in welke vorm dan ook– heeft bijgedragen aan de totstandkoming van dit proefschrift!

'Last but not least' bedank ik de paranimfen Florian en Jaap die mij bijstaan op de dag van de verdediging van mijn proefschrift.